14

TRANSMITTERS

The concept of a laser was first published by A. L. Schawlow and C. H. Townes in 1958. Successful operation of the first laser (ruby laser) by T. H. Maiman amazed the scientific world in 1960. Since then, laser development has progressed at a fast pace, and numerous kinds of lasers have been invented.

The principle of operation of a laser will be presented as an extension of the light amplifier presented in the previous chapter. In a light amplifier, light passes through the gain medium once. In a laser, there are partially reflecting mirrors at each end of the gain medium, forming what is called the laser cavity. On average, light travels back and forth through the laser cavity many, many times before exiting. For lasing to occur, the amplitude must grow with each round trip, and the various round-trip components must interfere constructively.

14.1 TYPES OF LASERS

Our primary interest is semiconductor lasers, but before moving on to an in-depth treatment of semiconductor lasers, let us take a moment to look at some other popular kinds of lasers. These include gas lasers, excimer lasers, dye lasers, solid-state lasers, and chemical lasers.

14.1.1 Gas Lasers

An example of a gas laser [1] is the helium–neon (He–Ne) laser. The He–Ne laser emits red light at a wavelength of 0.6328 μm with a narrow spectrum of a few kilohertz. Figure 14.1 shows the structure of the He–Ne laser. The gas pressure is a few torr with a 5:1 gas pressure ratio of He and Ne. A few kilovolts is applied to start a discharge and then the potential is reduced by about half after the discharge starts. The He–Ne laser is pumped by the impact of electrons in the discharge. The laser cavity is made of two concave end mirrors with reflectivities higher than $R = 99.8\%$.
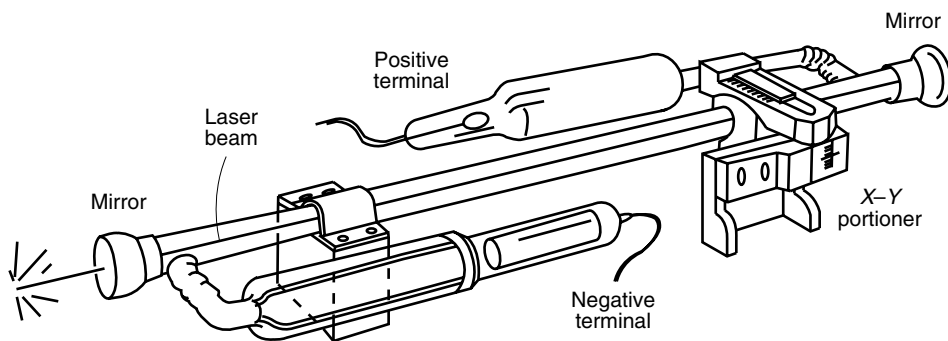
Figure 14.1 Geometry of the He−Ne gas laser.

The argon ion (Ar^+) laser is a gas laser that has several discrete spectra ranging from $\lambda = 0.488$ to 0.515 μm, of which the 0.515-μm line is the strongest.

The carbon dioxide (CO_2) laser emits high-intensity light at $\lambda = 10.6$ μm in the far-infrared region.

The excimer laser derives its name from an abbreviation for excited dimer. (A dimer is a molecule made of two identical atoms or molecules, whereas a polymer is made of many identical molecules.) Excimer lasers use such gases as Xe_2, Kr_2, or Ar_2. The output power is large and the wavelength lies in the vacuum ultraviolet (VUV) region, which is between 0.1 and 0.2 μm.

14.1.2 Solid-State Lasers

It was the solid-state laser [2] that T. H. Maiman first demonstrated at Hughes Aircraft Company. An artificial ruby (CrO_3 in Al_2O_3) was used. The wavelength of the ruby laser is 0.6934 μm.

Other popular solid-state lasers that the reader has some familiarity with from the previous chapter are the Er (erbium)-doped fiber laser, the Pr (praseodymium)-doped fiber laser, the neodymium YAG (yttrium−aluminum−garnet) laser, and the neodymium glass laser. The Er- and Pr-doped fiber lasers operate at 1.54 and 1.3 μm, respectively. The neodymium YAG and neodymium glass lasers operate at 1.064 and 1.3 μm.

The solid-state lasers are optically pumped by either a xenon or mercury flash lamp or even by a semiconductor laser array.

14.1.3 Dye Lasers

Organic dyes are used as laser media [1]. The gain curve of the rhodamine 6G dye extends from 0.57 to 0.66 μm and that of oxazine extends from 0.7 to 0.83 μm. The organic dyes are optically pumped by a laser with a wavelength shorter than the wavelength of their own emission. The wavelength of the dye laser can be scanned continuously by changing the resonance of the cavity containing the dye. If the laser media are exchanged, one after the other, the dye laser can cover a wide wavelength spectrum from 0.3 to 1.0 μm using the same physical arrangement.

14.1.4 Chemical Lasers

When hydrogen gas is injected into a high-temperature supersonic jet of SF_6, atomic fluorine (F) dissociated from SF_6 reacts with the hydrogen gas and chemical reactions take place, such as

$$H_2 + F \rightarrow HF + H \quad or \quad H_2 + 2F \rightarrow HF_2 + H \qquad (14.1)$$

This chemical reaction releases 31.7 kcal/mol of energy. This energy pumps HF or HF_2 into the excited state. The transition of HF or HF_2 emits radiation at wavelengths ranging from 2.7 to 2.9 µm. It is reported that the conversion efficiency of chemical to laser energy is 12%. A laser with 20-foot diameter mirrors placed 3 feet apart emits more than 400-W laser light [3]. A special feature of the chemical laser is the possibility of creating a laser that does not require an external energy source.

14.2 SEMICONDUCTOR LASERS

Of all the lasers mentioned so far, semiconductor [4,5] and solid-state lasers are the most commonly used sources for fiber-optic communication. This is because of such advantages as:

- Long life
- High reliability
- Ruggedness, compactness, and light weight
- High efficiency of electrooptic conversion
- Low applied voltage
- Spectral purity compared to non laser sources
- Direct modulation capability up to tens of gigahertz

It is the semiconductor lasers that are predominantly used for fiber-optic communication systems. Gallium arsenide lasers doped with aluminum ($Al_xGa_{1-x}As$) cover the wavelength range from 0.85 to 0.78 µm with increasing x. The laser doped with indium and phosphorus rather than aluminum ($In_{1-x}Ga_xAs_yP_{1-y}$) covers from 0.9 to 1.67 µm, depending on the values of x and y. With the proper combination of x and y, a laser can be designed to emit at 1.3 µm corresponding to the wavelength of the nondispersive range of the glass optical fiber, or it can be designed to emit at 1.55 µm corresponding to the lowest loss range of glass optical fibers. In communications, the semiconductor laser is also referred to as a laser diode or LD for short.

14.2.1 Gain of a Semiconductor Laser Amplifier

In Chapter 13 on the optical amplifier, it was mentioned that a semiconductor laser immediately becomes a semiconductor laser amplifier (SLA) simply by removing the end reflectors of the laser cavity. The treatment in this section complements that in Sections 13.4 and 13.5.

What's cooking in the laser kitchen? A couple of novelty lasers will be added here. An edible laser was cooked by mixing the nontoxic dye fluorescene with gelatin. Emission at $\lambda = 0.657$ μm was reported.

Although one is tempted to dismiss the edible laser as being flippant, gelatin is in fact a material with a number of interesting properties and has been studied quite seriously. Gelatin is used in emulsions for photography and holography and has played an important role in the development of the sophisticated DFB laser (see Section 14.9.3).

It is also reported that a kitchen utensil can be used as a mirror in the laser cavity. The laser cavity was made by combining a spatula with a conjugate mirror. The conjugate mirror (see Section 8.1) is made by four-wave mixing in a photorefractive medium and has the special property of reflecting back the incident light along the same path that the light had originally. In other words, the reflected light is on the same side of the normal to the surface of the mirror rather than following the law of reflection, which states that the light is reflected on the other side of the normal to the mirror surface at an angle equal to the incident angle, as shown in Fig. 14.2. No matter how crudely the laser cavity mirror is oriented with respect to the other conjugate mirror, the light goes back and forth taking the same path, and an efficient feedback of light is realized. If a conjugate mirror is used as one mirror of the laser cavity, a handheld spatula can be used as the other laser cavity mirror.
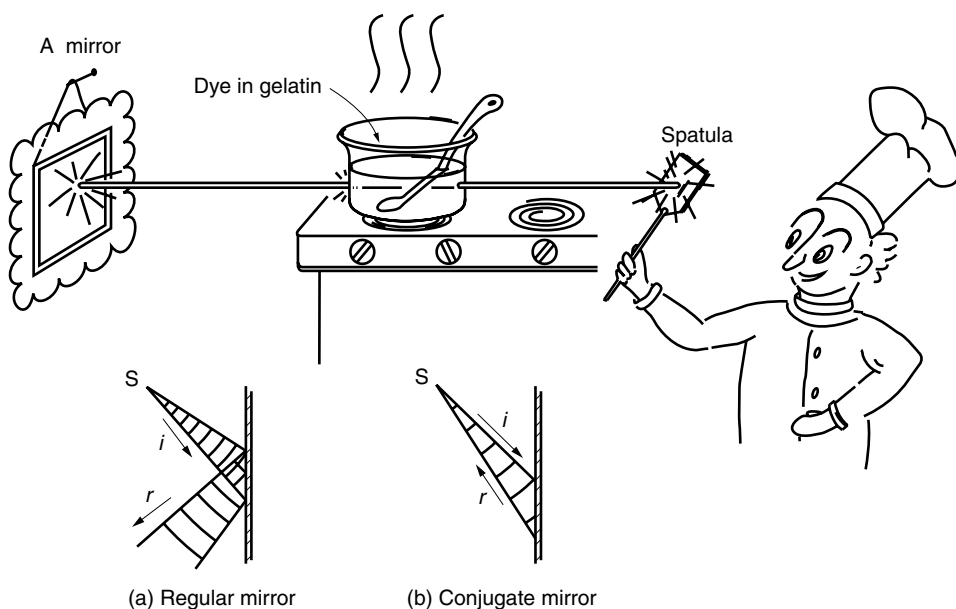

(a) Regular mirror   (b) Conjugate mirror

Figure 14.2   What's cooking in the kitchen? An edible laser!

One of the biggest factors that differentiates semiconductor laser materials from other materials is the existence of bands of energy levels rather than discrete energy levels, as in the case of gas or fiber amplifier materials mentioned in Chapter 13. A transition of an electron from any energy level within the conduction band into any level of the valence band emits light. Because of the spread of the energy band, the gain of the semiconductor material is spread over a wide range.

First, an explanation of the gain curve will be attempted using Fig. 14.3. Figure 14.3a shows how the electrons would populate the energy levels in a pure (intrinsic) semiconductor at a temperature of 0 K and with no current flowing through it ($T = 0$, $J = 0$). The energy level E_c is the bottom of the conduction band and E_v is the energy level of the top of the valence band and $g(E)$ represents the density of states. For Fig. 14.3a, all valence states are filled by electrons, as indicated by the hatched region, and the conduction states are empty. The Fermi level F, which defines the border between occupied electron states and unoccupied electron states at $T = 0$ K and $J = 0$, lies between E_c and E_v. Figure 14.3b illustrates what happens when an n-type impurity is introduced into the semiconductor, while keeping $T = 0$ and $J = 0$. An n-type impurity is one that has more valence electrons than the host material. In this case, all the valence band states are filled by electrons, and also the lower states of the conduction band are occupied up to the level F_c, which is the Fermi level of the n-doped semiconductor. Figure 14.3c is the same for a p-doped semiconductor. A p-type impurity is one that has less valence electrons than the host material. The Fermi level F_v of the p-doped semiconductor lies below E_v, indicating that there are unfilled states in the valence band.

If p-type and n-type semiconductors are joined, a nonequilibrium situation can be established, as shown in Fig. 14.3d, whereby the conduction band resembles that of the n-doped semiconductor and the valence band resembles that of the p-doped semiconductor. If one applies an optical pump to the junction area, or applies a bias
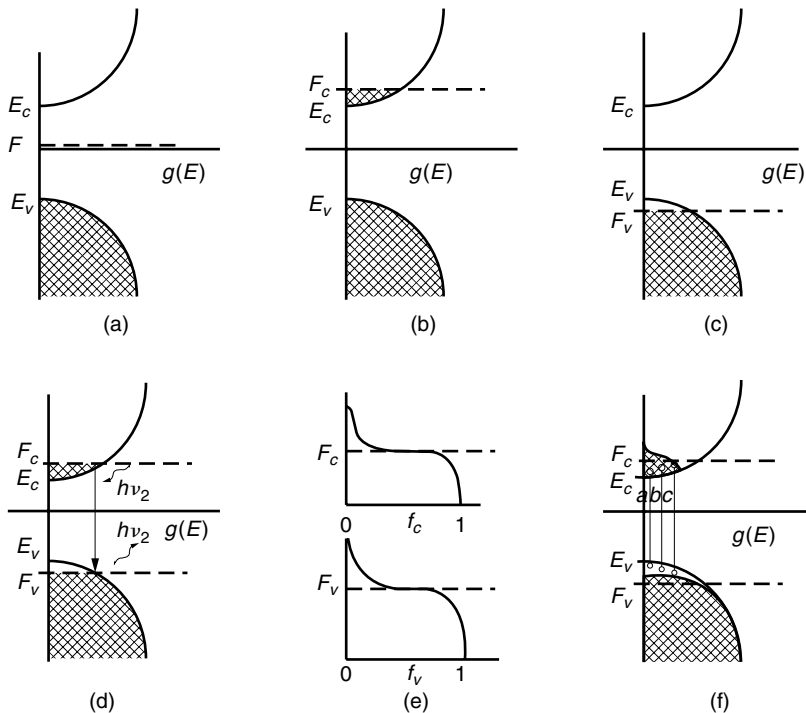

Figure 14.3   Density of state function $g(E)$ and the Fermi–Dirac distribution. (a) $T = 0$, $J = 0$, pure semiconductor. (b) $T = 0$, $J = 0$, n-doped semiconductor. (c) $T = 0$, $J = 0$, p-doped semiconductor. (d) $T = 0$, $J = 0$, p-n junction. (e) Fermi–Dirac distribution. (f) $T \neq 0$, $J = 0$, p-n junction.

voltage, electrons in the valence band absorb light and move to the conduction band, where they quickly settle into the lower states of the conduction band. Conversely, a photon of energy $h\nu_2$, as shown in Fig. 14.3d, can stimulate emission of another photon $h\nu_2$ by inducing an electron to make the transition from the conduction band to an empty state in the valence band.

Figure 14.3f depicts the situation where $T \neq 0$ and $J \neq 0$ at the p-n junction. The effect of a bias current is to create a nonequilibrium distribution similar to the impinging light in Fig. 14.3d. The effect of raising the temperature is to blur the distribution around F_c and F_v. The next step is to determine the criteria for amplification.

Before doing this, let us digress for a moment to explain semiconductor terminology. When an electron makes the transition from the valence band to the conduction band, it leaves behind a positively charged hole. The valence state vacated by the electron is said to be occupied by the positively charged hole. Furthermore, this hole is a positively charged carrier. The mobility of the hole arises from the fact that a nearby valence electron tends to fill the hole and, in doing so, leaves a hole behind in a different location, which in turn is filled by a nearby valence electron, and so forth. When an electron makes a transition from the conduction band to fill a hole in the valence band, this process is called recombination. Recombination can be viewed as the annihilation of a negative carrier (conduction electron) and a positive carrier (hole in the valence band), and energy is released. Energy is used either to radiate photons or heat the lattice of the crystal.

The electron density $n(E_2)$, which is the number of electrons per unit volume in energy levels between E_2 and $E_2 + dE_2$ in the conduction band, is given by

$$n(E_2)dE_2 = g_c(E_2)f_c(E_2)\,dE_2 \tag{14.2}$$

where

$$g_c(E_2) = \frac{\sqrt{2}m_e^{*3/2}}{\hbar^3\pi^2}(E_2 - E_c)^{1/2} \tag{14.3}$$

$$f_c(E_2) = \frac{1}{e^{(E_2 - F_c)/kT} + 1} \tag{14.4}$$

In Eq. (14.3), m_e^* is the effective mass of an electron, and $\hbar = h/2\pi$.

The function $g_c(E_2)$ represents the density of states per unit energy per unit volume in the conduction band at energy level E_2 and is proportional to $(E_2 - E_c)^{1/2}$. The proof of Eq. (14.3) is presented later when discussing the case of a quantum well and it is given by Eq. (14.203). The function $f_c(E_2)$ is the Fermi–Dirac distribution function that specifies the probability that the energy level E_2 in the conduction band will be occupied by an electron [6]. The Fermi–Dirac distribution is graphed in Fig. 14.3e. F_c is the qausi-Fermi level of electrons in the conduction band. E_c is the bottom edge of the conduction band.

Similarly, at the energy level E_1 in the valence band, the hole density $p(E_1)$, which is the number of holes per unit volume that are in the energy levels between E_1 and $E_1 + dE_1$, is expressed by

$$p(E_1)dE_1 = g_v(E_1)[1 - f_v(E_1)]\,dE_1 \tag{14.5}$$

where

$$g_v(E_1) = \frac{\sqrt{2}m_h^{*3/2}}{\hbar^3\pi^2}(E_v - E_1)^{1/2} \tag{14.6}$$

$$f_v(E_1) = \frac{1}{e^{(E_1-F_v)/kT} + 1} \tag{14.7}$$

$[1 - f_v(E_1)]$ is the probability of the absence of an electron or the presence of a hole at E_1. The quantities $g_v(E_1)$, $f_v(E_1)$, F_v, E_v, and m_h^* are similar to those defined for Eqs. (14.2), (14.3), and (14.4), but for holes in energy levels between E_1 and $E_1 + dE_1$ in the valence band.

The difference in the quasi-Fermi levels F_c and F_v is equal to the potential energy eV_b of the bias voltage V_b.

Recall that in the case of discrete energy levels, such as for an erbium-doped fiber amplifier, the emission equation, Eq. (13.20), consists of two terms. The first term is proportional to the input light whose coefficient can be considered as the gain of the amplifier. The second term is independent of the input light and can be considered as the noise of the amplifier. Let us first treat the amplifier term. Gain is the difference between stimulated emission and absorption. With a semiconductor, stimulated emission occurs when an incident photon induces an electron to make the transition from the conduction band to the valence band, and is proportional to the product $n(E_2)p(E_1)$ of the density of electrons in the conduction band and the density of holes in the valence band. Absorption is the transition in the reverse direction and is proportional to the product of the density of electrons in the valence band expressed by

$$n(E_1)dE_1 = g_v(E_1)f_v(E_1)dE_1 \tag{14.8}$$

and the density of vacant states in the conduction band expressed by

$$p(E_2)dE_2 = g_c(E_2)[1 - f_c(E_2)] \, dE_2 \tag{14.9}$$

Finally, the net increase in the photon density S (number of photons per unit volume) is thus

$$\frac{dS}{dt} = \iint W[n(E_2)p(E_1) - n(E_1)p(E_2)] \, dE_1 \, dE_2 \tag{14.10}$$

W is the stimulated transition probability and is expressed by

$$W = BE_d \tag{14.11}$$

where B is Einstein's B coefficient and E_d is the energy density of the light that is stimulating the transition. E_d is given by

$$E_d = h\nu S \tag{14.12}$$

From Eqs. (14.10), (14.11), and (14.12), the increase in the energy density of the light is

$$\frac{dE_d}{dt} = \iint Bh\nu E_d[n(E_2)p(E_1) - n(E_1)p(E_2)] \, dE_1 \, dE_2 \tag{14.13}$$

E_d is related to the light intensity I_s by means of Eq. (13.11) as

$$E_d = \frac{I_s}{v}$$

where v is the velocity of light.

$$\left(\frac{dI_s}{dz}\right)_{\text{stim}} = I_s \iint B\frac{hv}{v}[n(E_2)p(E_1) - n(E_1)p(E_2)]\, dE_1\, dE_2 \qquad (14.14)$$

where

$$\frac{d}{vdt} = \frac{d}{dz}$$

was used.

Next, the spontaneous emission will be calculated. The spontaneous emission is proportional to the product $n(E_2)p(E_1)$ of the density of electrons in the conduction band and the density of holes in the valence band. The increase in the photon density S by spontaneous emission is

$$\left(\frac{dS}{dt}\right)_{\text{spon}} = \iint An(E_2)p(E_1)\, dE_1\, dE_2 \qquad (14.15)$$

where A is Einstein's A coefficient. Equation (14.15) can be converted into the change in the light intensity variation due to spontaneous emission in a similar manner as Eq. (14.14) was obtained from Eq. (14.10).

$$\left(\frac{dI_s}{dz}\right)_{\text{spon}} = \iint A\frac{hv}{v}n(E_2)p(E_1)\, dE_1\, dE_2 \qquad (14.16)$$

The resultant light intensity variation is

$$\frac{dI_s}{dz} = \left(\frac{dI_s}{dz}\right)_{\text{stim}} + \left(\frac{dI_s}{dz}\right)_{\text{spon}} \qquad (14.17)$$

and combining Eqs. (14.14) and (14.15) and rewriting in a manner similar to Eq. (13.20), the final differential equation of the semiconductor laser amplifier is

$$\frac{dI_s}{dz} = g(hv)I_s + h(hv) \qquad (14.18)$$

where

$$g(hv) = B \iint \frac{hv}{v}[n(E_2)p(E_1) - n(E_1)p(E_2)]\, dE_1\, dE_2 \qquad (14.19)$$

$$h(hv) = A \iint \frac{hv}{v}n(E_2)p(E_1)\, dE_1\, dE_2 \qquad (14.20)$$

Let us examine Eq. (14.19). Insertion of Eqs. (14.2), (14.5), (14.8), and (14.9) into Eq. (14.19) leads to

$$g(h\nu) = B \iint \frac{h\nu}{v} g_c(E_2) g_v(E_1) [f_c(E_2) - f_v(E_1)] \, dE_1 \, dE_2 \tag{14.21}$$

The condition for positive gain is obtained by inserting Eqs. (14.4) and (14.7) into Eq. (14.21) as

$$E_2 - E_1 < F_c - F_v \tag{14.22}$$

This means the upper limit on the energy of $E_2 - E_1 = h\nu$ is $F_c - F_v$. When a forward bias current is applied, the difference $F_c - F_v$ is identical to the potential energy eV_b established by the external bias voltage V_b. The lower limit of the gain curve is determined approximately by the energy gap and, hence, the frequency range of the stimulated emission is

$$E_g < h\nu < eV_b \tag{14.23}$$

where

$$eV_b = F_c - F_v \tag{14.24}$$

Next, the gain curve will be obtained using a graphical method. E_1 in Eq. (14.21) is replaced by $E_1 = E_2 - h\nu$ to obtain

$$g(h\nu) = B \frac{h\nu}{v} \int g_c(E_2) g_v(E_2 - h\nu) [f_c(E_2) - f_v(E_2 - h\nu)] \, dE_2 \tag{14.25}$$

Figure 14.4 shows the distribution of the integrand with respect to energy E_2. $T = 0$ is assumed and the part of the integrand in the square brackets becomes either ± 1 or zero. Note that mathematically $g(h\nu)$ is the cross-correlation between $g_c(E_2)$ and $g_v(E_2 - h\nu)$, multiplied by the factor of $[f_c(E_2) - f_v(E_2 - h\nu)]$. This means $g(h\nu)$ is obtained by shifting one of the functions by $h\nu$ and integrating the product.

In order to calculate $g(h\nu)$, g_v and f_v are shifted toward the right. As soon as the amount $h\nu$ of shift exceeds $E_c - E_v$, the value of $g(h\nu)$ becomes nonzero because of the overlap of g_v and g_c. However, $g(h\nu)$ becomes zero and then negative as soon as the amount $h\nu$ of shift exceeds $F_c - F_v$. The value of $g(h\nu)$ becomes negative because of the change in the sign of $[f_c(E_2) - f_v(E_2 - h\nu)]$. The $g(h\nu)$ curve has a bell shape with the maximum near the center.

The calculated gain spectrum $g(h\nu)$ for $Ga_{0.47}In_{0.53}As$ [7] is shown in Fig. 14.5. The lower frequency cutoff does not match the bandgap, but slightly extends beyond it; this will be ignored for the time being.

Finally, an attempt will be made to recast the gain curve $g(h\nu)$. Such a recast makes the analysis of the semiconductor laser simpler. Figure 14.6 is a replot of the peak values of the gain curves in Fig. 14.5 as a function of the carrier density N. The replot is quite linear with $N - N_\alpha$, so that it is justifiable to write
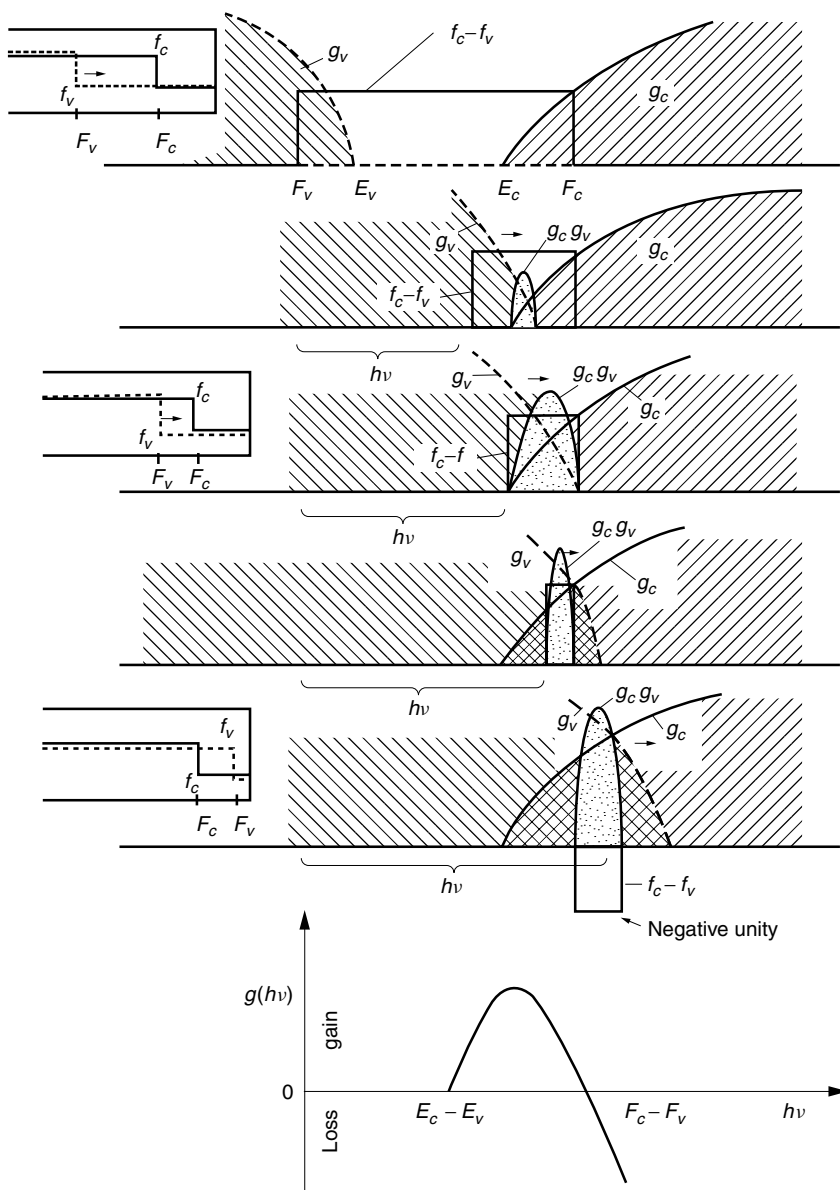
$$g = a(N - N_\alpha) \tag{14.26}$$

**Figure 14.4** Graphical explanation of the calculated gain spectrum.

where g without the argument $(h\nu)$ is used to designate the replot of the peaks of $g(h\nu)$. The quantity a is the newly defined gain constant. N_α is the electron density that intercepts the horizontal axis; it is called the zero gain electron density of the medium. For those applications where the frequency behavior is not a prime concern, Eq. (14.26) is a good approximation. The power equation of the semiconductor laser becomes

$$\frac{dI_s}{dz} = gI_s + h \tag{14.27}$$

The general shape of the gain curves in Fig. 14.5 will be appreciated using the model of a "photon punch press" shown here. This machine is made of a pair of punch-out dies. In order to generate a photon by the recombination of an electron and a hole, the machine has to punch out an electron and a hole at the same time. The spacing between the punch-out dies can be adjusted for photons of a specific frequency.

Such a machine may help us to better visualize the following behavior of the gain curves in Fig. 14.5:

1. The lower and upper limits of $h\nu$ are E_g and $F_c - F_v$.

2. The fan shape for the material to be punched means the gain curves have their maxima slightly above the center of the positive gain region.

3. When the bias current is increased, and F_c is raised and F_v is lowered, the gain shifts toward a larger value of $h\nu$, and as well, the value of the maximum is increased.

Photon punch press.
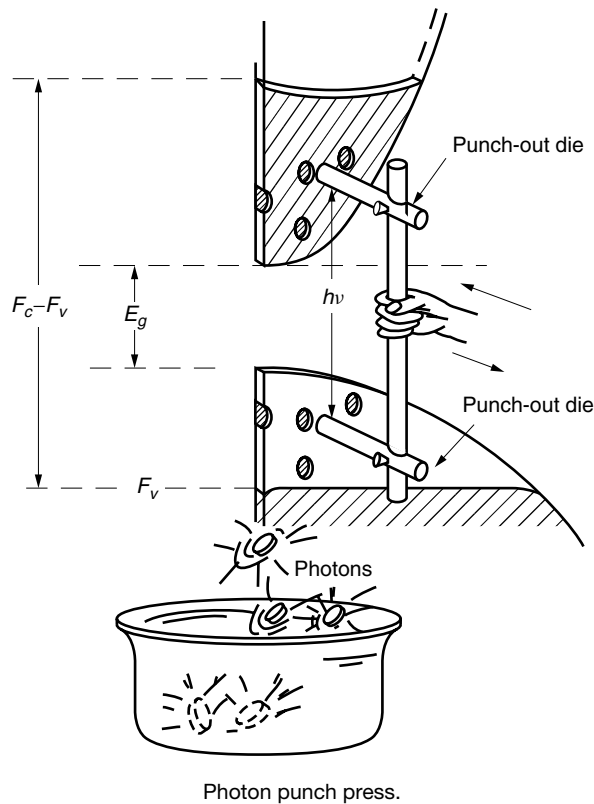
14.2.2 Laser Cavity

If mirrors are installed at the ends of the light amplifier and are oriented so that the output from the amplifier reenters the amplifier and follows the same path as the first pass, this is called *optical feedback*. A small amount of light, initially generated by spontaneous emission, is fed back to generate stimulated emission, which in turn is fed back to further generate stimulated emission and the oscillation starts. This is a laser.
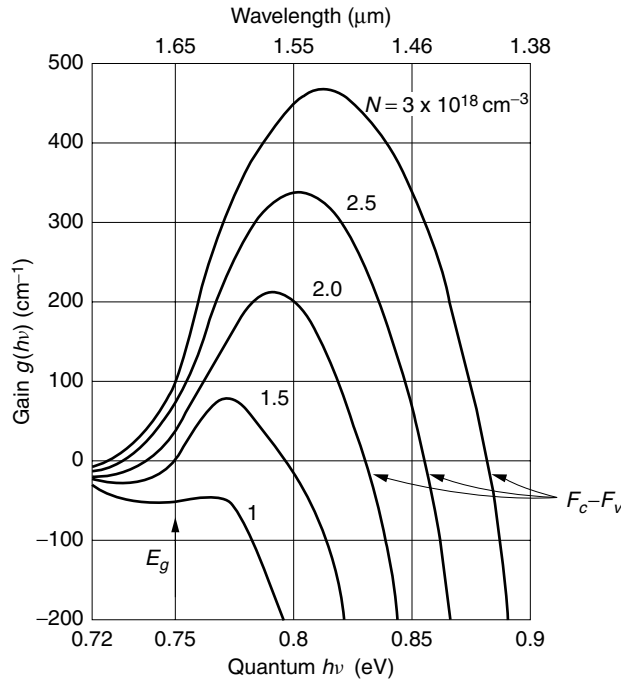
Figure 14.5   Gain spectrum of $Ga_{0.47}In_{0.53}As$. (After M. Asada and Y. Suematsu [7].)

The laser whose feedback light path is in a ring form is called a ring laser. The more common laser type uses end mirrors to reflect the light back and forth as a means of feedback. This laser can be very compact and is called a Fabry–Pérot (FP) type laser.

The amplifying medium of the laser is also referred to as the active medium. A structure that uses feedback to increase optical field intensities is known as an optical resonator. The laser is an optical resonator containing an active medium. Figure 14.7 shows the typical structure of a semiconductor laser. The active layer is the semiconductor p-n junction.

The forward bias current injects holes into the p-type layer on the top through a narrow metal stripe electrode, and electrons to the n-type layer through a metal electrode at the bottom. Recombination of the electrons and holes takes place in the narrow thin active layer. The generated light is confined inside the active layer because the index of refraction of the active layer is raised from that of the adjacent p- and n-type cladding layers.

Partially reflecting mirrors, which are simply cleaved surfaces or deposited mirrors, are placed on both ends of the active layer. The light that is reflected back and forth between these mirrors enhances the stimulated emission and becomes significantly larger than spontaneous emission. For each pass through the active layer, part of the light is reflected at the mirror, and the rest is transmitted through the mirror. The transmitted light is the laser output.

Artificial diamond whose heat conductivity is about three times as high as copper is often used as a heat sink.
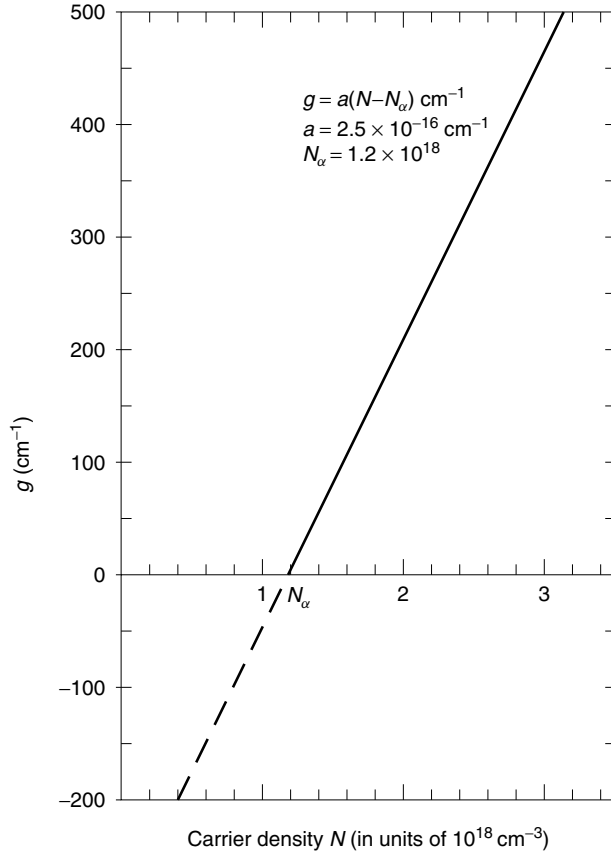
Figure 14.6   Linearized gain with respect to the carrier density N for $Ga_{0.47}In_{0.53}As$.

14.2.3   Conditions for Laser Oscillation

Figure 14.8 gives a heuristic illustration of a Fabry–Pérot type laser. As the light bounces back and forth in the active region, the light is amplified. From Fig. 14.8, the conditions for the wave to grow and finally oscillate are (1) the amplitude after each round trip has to be larger than before, and (2) the phase after each round trip has to be the same as the phase of the original trip.

14.2.3.1   *Amplitude Condition for Laser Oscillation*
The light travels back and forth in the active region between the end mirrors. The power of the amplification with distance will be obtained by solving Eq. (14.27) with $h \doteq 0$.

$$P = P_0 e^{gz}$$

In the real world, power is lost due to attenuation in the medium and escape at the cavity end mirrors. Taking these into account and writing in terms of amplitude rather than power, the amplification for one round trip is given by

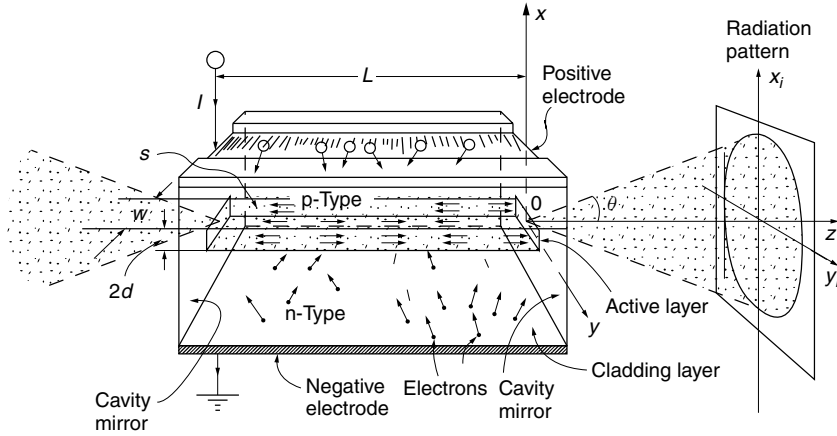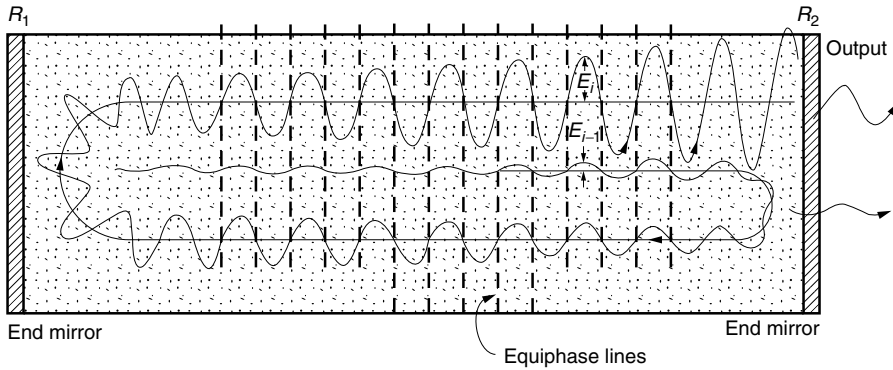$$E = E_0 R e^{(1/2)(g-\alpha)2L+j2\beta L} \tag{14.28}$$

Figure 14.7 Semiconductor laser.

Figure 14.8 Two conditions for lasing action: (1) gain $E_i > E_{i-1}$ and (2) phase match $\phi_i = \phi_{i-1} + 2\pi n$.

where E_0 is the amplitude of the light before the trip, L is the length of the active region, α is the power attenuation constant, and β is the propagation constant. If the amplitude reflection coefficients of the mirrors are r_1 and r_2, then $R = r_1 r_2$.

Equation (14.28) is the amplitude E of the light after each round trip. The reason for the expression in terms of amplitude is that both amplitude and phase are necessary when analyzing the conditions for lasing. Note that both g and α are defined in terms of power rather than amplitude, and they are halved for expressing the amplitude.

There are two important conditions for the field to grow after each round trip. The first condition is that the gain has to be larger than unity

$$Re^{(g-\alpha)L} \geq 1$$

and

$$g \geq \frac{1}{L} \ln \frac{1}{R} + \alpha \qquad (14.29)$$

In a medium with small gain, R has to be large. For instance, the He–Ne laser has a small gain $g = 10^{-4}$–10^{-3}cm^{-1}, so that the reflectivity R of the cavity mirrors has to be

$R = 0.998$. A GaAs semiconductor laser whose gain is as large as $g = 100-300$ cm^{-1} can afford a smaller reflectivity, and simple cleaved surfaces at the ends will suffice. The reflectance from a cleaved surface is

$$R = \left(\frac{n-1}{n+1}\right)^2 \tag{14.30}$$

where n is the index of refraction. For GaAs, $n = 3.5$ and $R = 0.31$.

The second condition for the field to grow concerns the phase.

14.2.3.2 *Phase Condition for Laser Oscillation*

So that the lightwave will constructively interfere, the phase after each round trip has to be an integral multiple of 2π, as shown in Fig. 14.8.

$$2\beta L = 2p\pi \tag{14.31}$$

where $p = 1, 2, 3, \ldots$, and β is the propagation constant in the active layer. Since the active layer is so thin that only the lowest order transverse mode is excited (see Section 9.4), the propagation constant β can be approximated as

$$\beta = \frac{2\pi}{\lambda_p} n \tag{14.32}$$

where n is the index of refraction of the active layer. Combining Eqs. (14.31) and (14.32) gives

$$\lambda_p = \frac{2nL}{p} \tag{14.33}$$

The wavelength λ_p is the wavelength of the pth cavity mode or pth longitudinal mode. The separation between adjacent longitudinal modes is

$$\Delta\lambda = -\frac{\lambda_p^2}{2nL} \tag{14.34}$$

where

$$\Delta\lambda = \lambda_p - \lambda_{p-1}$$

Equation (14.34) is an important quantity to be considered in fabricating a single longitudinal mode (SLM) laser.

Expressed in terms of frequency, Eq. (14.33) becomes

$$\nu_p = \frac{c}{2nL} p \tag{14.35}$$

and

$$\Delta\nu = \frac{c}{2nL} \tag{14.36}$$

where

$$\Delta\nu = \nu_p - \nu_{p-1}$$

The mode spacing decreases with an increase in cavity length.

14.2.4   Qualitative Explanation of Laser Oscillation

Figure 14.9 explains the same fact in a more qualitative manner. Figure 14.9a illustrates the frequencies that satisfy the condition for the round trips to be in phase. These frequencies are the resonant frequencies ν_p given by Eq. (14.35) of the cavity, as indicated by the notches along the horizontal axis in Fig. 14.9a. Figure 14.9b is a graph of the gain curves with respect to the frequency ν for the semiconductor laser with the injection current as a parameter. The envelopes of the gain curves are similar to those in Fig. 14.5, with a comb like structure that will be explained later.

The following describes the output of the laser as the injection current is increased. When the injection current is very small, the gain is low and the amplitude after each
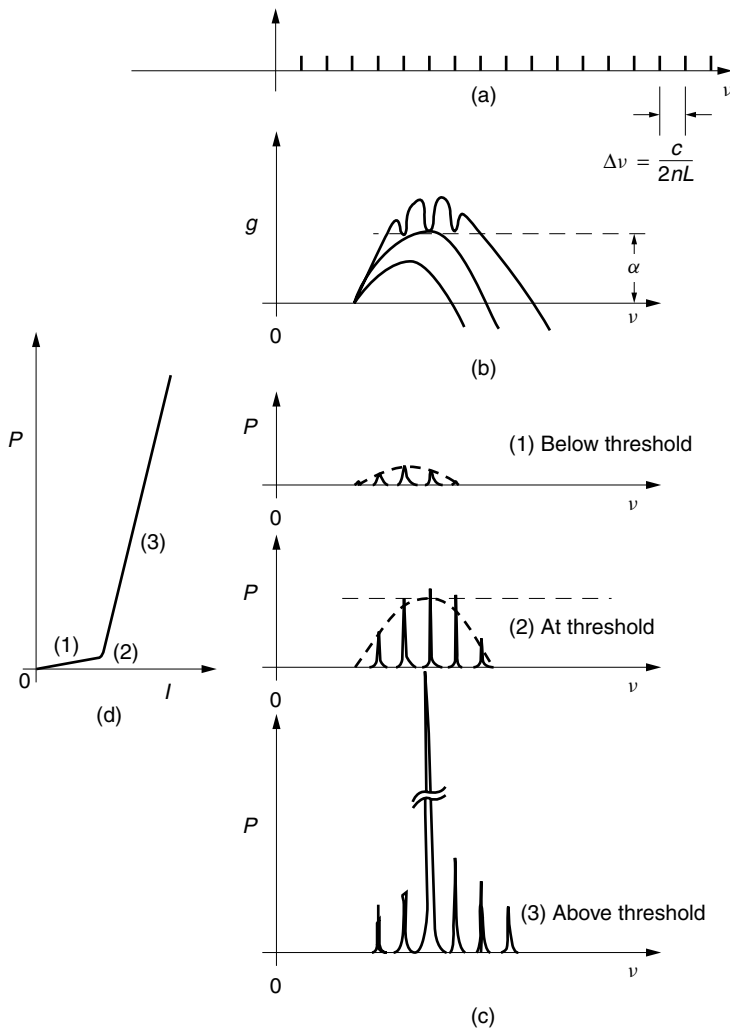

Figure 14.9 Gain curves and laser oscillation. (a) Resonance frequencies of the cavity. (b) Gain curves. (c) Output from the laser. (d) Power versus current characteristic of a laser.

round trip is smaller than the amplitude of the preceding trip because of the attenuation. Light with small amplitude is observed at the resonant frequencies of the cavity, as indicated in Fig. 14.9c(1), but the radiation is primarily due to spontaneous emission. As the injection current is increased, the height of the gain curve rises until it reaches the threshold value, namely, the gain is just canceled by the attenuation. At threshold, the amplitude after each round trip is the same as before. The output spectrum at threshold is shown in Fig. 14.9c(2). With a further increase in the injection current beyond the threshold, the gain g exceeds the attenuation α, and the amplitude of the light grows. What happens above threshold depends on the type of laser. The resonant frequencies are also called longitudinal modes. If the laser is a "quasi" single longitudinal mode laser, several modes may reach threshold, but only the mode that reaches threshold first keeps growing, as shown in Fig. 14.9c(3), and this mode clearly dominates the other lasing modes. In a truly multimode laser, the resonant frequencies are closely spaced and several will reach threshold at about the same time. These modes will begin to oscillate, and there is no large dominance of one mode over its neighbors. In a true single-mode laser, only one mode oscillates.

The output light power P versus bias current is shown in Fig. 14.9d. The output light is practically null until the bias current reaches the threshold current. Thereafter, the output light almost linearly increases with the bias current.

14.3   RATE EQUATIONS OF SEMICONDUCTOR LASERS

The rate equations for the semiconductor laser [8] are slightly different from those developed for the EDFA in the previous chapter, where both pump and signal powers were light powers. With the semiconductor laser, electrons are used for the pump and photons for the signal.

Electrons injected into the semiconductor junction in the form of a current are eventually converted into the emission of photons. The rate equations are differential equations that relate these two quantities: injected carrier density and photon density. The rate equations are used to obtain quantities such as the threshold current, the turn-on delay, and the upper limit on modulation frequency.

In previous sections that dealt with trying to find the power of amplification, the derivative with respect to length was used. However, in a laser, one is usually not interested in keeping track of how many times the light goes back and forth for amplification. The derivative with respect to time is often the more practical approach in laser systems.

$$\underbrace{\frac{dN}{dt}}_{\substack{\text{Rate of} \\ \text{electrons} \\ \text{introduced} \\ \text{into unit} \\ \text{volume} \\ \text{per unit} \\ \text{time}}} = \underbrace{\frac{J}{2ed}}_{\substack{\text{Number of} \\ \text{electrons} \\ \text{injected} \\ \text{into unit} \\ \text{volume} \\ \text{per unit} \\ \text{time}}} - \underbrace{Sb(N - N_\alpha)}_{\substack{\text{Number of} \\ \text{electrons} \\ \text{depleted by} \\ \text{stimulated} \\ \text{emission of} \\ \text{photons per} \\ \text{unit volume} \\ \text{per unit time}}} - \underbrace{\frac{N}{\tau_n}}_{\substack{\text{Number of} \\ \text{electrons} \\ \text{depleted by} \\ \text{spontaneous} \\ \text{emission or} \\ \text{escaping} \\ \text{from the} \\ \text{action region} \\ \text{per unit} \\ \text{volume} \\ \text{per unit time}}} \qquad (14.37)$$

$$\frac{dS}{dt} = \underbrace{Sb(N - N_\alpha)}_{} - \underbrace{\frac{S}{\tau_s}}_{} + \underbrace{\beta_s \frac{N}{\tau_n}}_{}$$

| Rate of photons generated per unit volume per unit time | Number of photons generated by stimulated emission per unit volume per unit time | Number of photons escaping from unit volume per unit time | Spectrum of spontaneous emission that overlaps with that of the stimulated emission | (14.38) |

where

    $2d =$ thickness of the active region

    $N =$ electron density

    $S =$ photon density

    $g =$ gain with respect to distance

    $a =$ gain constant with respect to distance

    $b =$ gain constant with respect to time and equal to va

    $J =$ injection current density

    $\tau_n =$ lifetime of the electrons in the conduction band before being lost by
        spontaneous emission or escape from the active region

    $\tau_s =$ lifetime of photons inside the cavity before going out of the cavity or
        being absorbed inside the cavity

    $\beta_s =$ fraction of spontaneously emitted photons whose spectrum coincides
        with that of the stimulated emission

Equation (14.37) is the rate of increase in conduction band electrons per unit volume per unit time. The rate is the contribution made by the injection current minus electrons recombined by stimulated emission minus the electrons lost by spontaneous emission and by escaping from confinement. Equation (14.38) is the rate of photons generated per unit volume per unit time, that is, the stimulated emission minus the photons that have escaped from the cavity plus the contribution of the spontaneous emission whose spectrum coincides with the stimulated emission. The last term is usually very small and is normally ignored ($\beta_s \approx 10^{-4}$–10^{-6}). In the following sections, the various quantities that can be derived from the rate equations will be presented.

The quantities τ_s, b, and J appearing in Eqs. (14.37) and (14.38) need further explanation. The lifetime τ_s of the photons inside the laser cavity is the inverse of the rate of disappearance of photons out of the laser cavity. For t seconds in the cavity, the light makes $vt/2L$ round trips. For each round trip, the light power is reduced by R^2 due to reflections at both end mirrors. For t seconds in the cavity, the light travels a distance vt, so that the power loss due to attenuation in the medium is $e^{-\alpha vt}$. Both losses may be represented by one parameter τ_s when $vt/2L$ is large. The lifetime τ_s satisfies

$$e^{-t/\tau_s} = (R^2)^{vt/2L} e^{-\alpha vt}$$

and hence

$$\frac{1}{\tau_s} = v\left(\frac{1}{L}\ln\frac{1}{R} + \alpha\right) \tag{14.39}$$

where v is the velocity in the active region and the identity $R = e^{\ln R}$ was used.

Next, b is explained. Using Eq. (14.26) and the relation $z = vt$, the first term of Eq. (14.27) can be rewritten as

$$\frac{dP}{dt} = b(N - N_\alpha)P \tag{14.40}$$

where

$$b = va \tag{14.41}$$

Next, a few words are added about the current density J. As shown in Fig. 14.7, the injection current I (not light intensity) is fed from the top electrode into the active region whose cross-sectional area is s and thickness is $2d$. The number of electrons brought into the active region per unit time is I/e, and the number N of electrons injected into unit volume during τ_n seconds therefore is $(I/es2d)\ \tau_n$ and

$$N = \frac{J}{2ed} \cdot \tau_n \tag{14.42}$$

where $J = I/s$ is the current per unit cross section or the current density in the active region and where the thickness of the active region is so short that the electron density was assumed uniform.

14.3.1 Steady-State Solutions of the Rate Equations

The steady-state solutions of Eqs. (14.37) and (14.38) will be obtained. The steady-state condition is

$$\frac{dN}{dt} = \frac{dS}{dt} = 0 \tag{14.43}$$

The threshold electron density and current and the output light power from the laser will be found.

14.3.2 Threshold Electron Density and Current

The electron density and the corresponding current that just initiates lasing action will be found. Before lasing, the photon density is

$$S_s \doteq 0$$

and from Eqs. (14.37) and (14.43) the electron density is

$$N = \frac{\tau_n}{2ed}J \tag{14.44}$$

The electron density linearly increases with the injection current density before lasing. As soon as the lasing starts and $S \neq 0$, from Eq. (14.38), the lasing steady-state condition implies

$$\left[b(N - N_\alpha) - \frac{1}{\tau_s} \right] S_s = 0 \tag{14.45}$$

where β_s was considered small and S_s is the steady-state photon density. The condition that Eq. (14.45) be satisfied even after lasing, when $S \neq 0$, is that the quantity inside the square brackets in Eq. (14.45) stays zero and

$$N = N_\alpha + \frac{1}{b\tau_s} \tag{14.46}$$

Note that Eq. (14.46) is independent of injection current. This means that, before lasing, N grows with J as in Eq. (14.44), but as soon as the lasing starts and then the steady state is reached, N stops growing and stays at this value, as indicated in Fig. 14.10. Physically speaking, after lasing starts, no sooner are the electrons injected into the active region than they recombine with holes and release photons. The electrons never have a chance to pile up, and the electron density stays at the steady-state value as in Eq. (14.46). This fact is explained by the comb-shaped gain function in Fig. 14.9b. The threshold electron density N_{th} is therefore

$$N_{th} = N_\alpha + \frac{1}{b\tau_s} \tag{14.47}$$

and the threshold current J_{th} that is needed for N to reach N_{th} is, from Eq. (14.44),

$$\frac{J_{th}}{2ed} = \frac{N_{th}}{\tau_n} \tag{14.48}$$

or, with Eq. (14.47),

$$\frac{J_{th}}{2ed} = \frac{1}{\tau_n}\left(N_\alpha + \frac{1}{b\tau_s}\right) \tag{14.49}$$
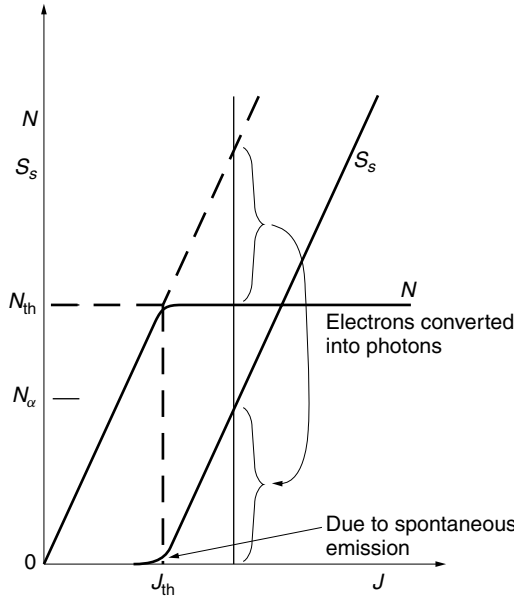

Figure 14.10   Photon and electron densities with respect to injection current J.

The right-hand side of Eq. (14.48) is associated with τ_n, which means that N_{th}/τ_n is the number of electrons either leaked out of the active region or converted into photons by spontaneous emission. The quantity J_{th} is the current needed to supply these lost electrons. It will soon become clear that it is important to keep J_{th} as small as possible for better laser performance.

14.3.3 Output Power from the Laser

The steady-state light output from the laser for a given injection current will be calculated. The steady state of Eqs. (14.37) and (14.38) gives

$$\frac{J}{2ed} = \frac{S_s}{\tau_s} + \frac{N}{\tau_n} \tag{14.50}$$

The right-hand side consists of the number of electrons converted into photons by stimulated emission and the number of electrons leaked out of the active region. As soon as lasing starts, N stops growing and stays at the value specified by Eq. (14.47) and

$$N = N_{th} \tag{14.51}$$

With Eqs. (14.48) to (14.51), S becomes

$$S_s = \frac{\tau_s}{2ed}(J - J_{th}), \quad J \geq J_{th} \tag{14.52}$$

S_s increases linearly with $(J - J_{th})$. If Eq. (14.52) is rewritten as

$$\frac{S_s}{\tau_s} = \frac{J - J_{th}}{2ed} \tag{14.53}$$

then the left-hand side is the rate of photon emission, and the right-hand side is the rate of electrons injected by the current above J_{th}. The electron density and the photon density are plotted as a function of injection current in Fig. 14.10. While the injection current is below the threshold, only the electron density increases with the injection current, and the photon density stays at zero. Once the injection current exceeds the threshold value, the situation reverses, and the photon density increases linearly with the injection current, while the electron density stays put at $N = N_{th}$.

It is interesting to check what happens to N if Eqs. (14.37) and (14.38) are used to calculate N beyond the threshold:

$$N = \tau_n \left(\frac{J}{2ed} - \frac{S_s}{\tau_s} \right) \tag{14.54}$$

The second term in the parentheses is the portion that is used for the stimulated emission. The rate of generation of S is replaced by Eq. (14.52), and Eq. (14.54) becomes

$$N = N_{th}$$

where Eq. (14.48) was also used. This confirms the earlier result of $N = N_{th}$ after lasing.

Next, an expression for the output power will be found. Equation (14.38) with $\beta_s = 0$ and $dS/dt = 0$ means that the number of photons generated inside the laser by stimulated emission (first term on the right-hand side) balances the number of photons leaked out and lost in the cavity (second term). The second term has two components, one component being the light leakage from the mirrors, that is, the laser output itself, and the other component being light lost due to attenuation in the cavity. The contribution S_s/τ_s for only the portion that leaked through the mirrors is found from Eq. (14.39) with $\alpha = 0$ as

$$\frac{1}{\tau_c} = \frac{v}{L} \ln \frac{1}{R} \tag{14.55}$$

If V is the volume of the active region, then VS_s/τ_c is the number of photons per second that escape from the active region of the laser into the outside world. The output light power from the cavity is therefore

$$P = h\nu V \frac{S_s}{\tau_c} \tag{14.56}$$

Insertion of Eq. (14.52) into (14.56) and rewriting the current density J in terms of the current I gives

$$P = \frac{h\nu}{e} \frac{\tau_s}{\tau_c}(I - I_{\text{th}}) \tag{14.57}$$

If $h\nu$ is approximated by the bandgap energy E_g in electron volts, then the output power is

$$P = E_g \frac{\tau_s}{\tau_c}(I - I_{\text{th}}) \tag{14.58}$$

Thus, the light output increases linearly with $I - I_{\text{th}}$ as indicated in Fig. 14.9d.

14.3.4 Time-Dependent Solutions of the Rate Equations

The physical quantities associated with the time-dependent solutions of Eqs. (14.37) and (14.38) will be found.

14.3.4.1 Turn-On Delay
A laser does not start lasing until the electron density reaches the threshold value, so that there is a turn-on delay. The turn-on delay time t_d for N to reach N_{th} will be calculated. Before lasing $S = 0$, and Eq. (14.37) becomes

$$\frac{dN}{dt} = \frac{J}{2ed} - \frac{N}{\tau_n} \tag{14.59}$$

and the turn-on delay is

$$t_d = \int_0^{N_{\text{th}}} \frac{dN}{\dfrac{J}{2ed} - \dfrac{N}{\tau_n}} \tag{14.60}$$

Integration gives

$$t_d = \tau_n \ln \left(\frac{J}{J - J_{\text{th}}} \right) \tag{14.61}$$

where Eq. (14.48) was used. When a step injection current such as shown in Fig. 14.11a is applied to the laser diode, N starts increasing as shown in Fig. 14.11b, and the laser diode does not start lasing until t_d seconds later as shown in Fig. 14.11c. From Eq. (14.61), one way of shortening the turn-on delay time is to raise the injection current. Equation (14.61) is often used to experimentally determine the value of τ_n. The logarithmic curve of $\ln[J/(J - J_{\text{th}})]$ versus t_d gives τ_n as its slope. The quantity τ_n is normally a few nanoseconds.

Pulsed modulation of the light is achieved by switching the bias current on and off. As the pulse rate is increased, the turn-on delay becomes a problem and limits the maximum bit rate. The laser with a lower threshold current has a shorter turn-on delay time, and this is one of the reasons for the desirability of a laser with a low threshold current mentioned earlier.
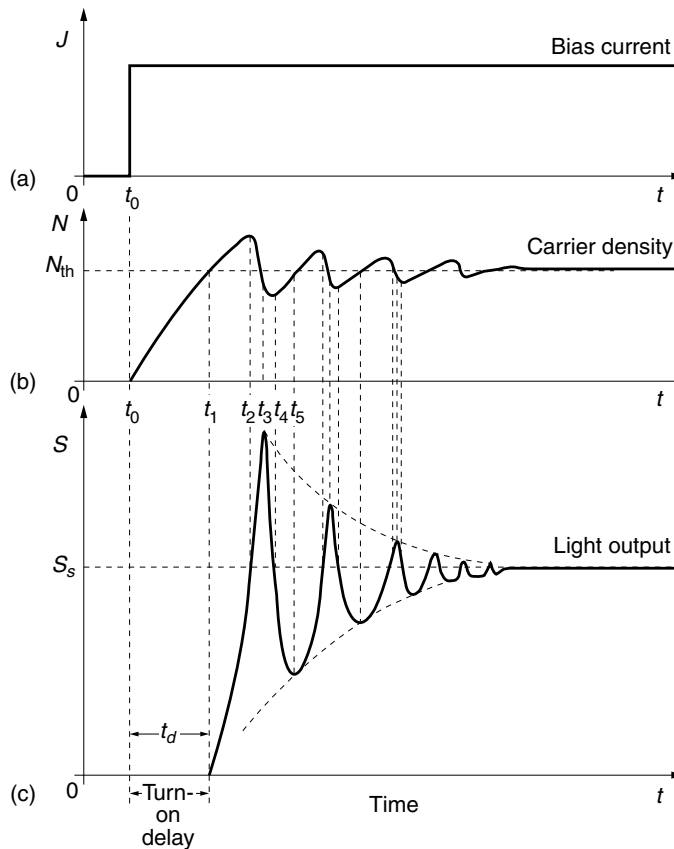

Figure 14.11 Explanation of the turn-on delay and the relaxation oscillation of a semiconductor laser. (a) Step injection current. (b) Carrier density. (c) Light output.

Another way to reduce t_d is biasing the injection current to $J = J_b$. The turn-on delay for such a case is calculated by changing the lower limit of the integral in Eq. (14.60):

$$t_d = \tau_n \ln \left(\frac{J - J_b}{J - J_{\text{th}}} \right) \tag{14.62}$$

A disadvantage of the biasing, however, is that as J_b approaches the threshold, the amount of emission (see Fig. 14.9 below threshold) for the off state of the pulse increases and the extinction ratio, which is the ratio of the light intensities for on and off states, becomes worse.

14.3.4.2 Relaxation Oscillation

When a laser diode is turned on, a transient decaying sinusoidal oscillation occurs as shown in Fig. 14.11. This oscillation is called *relaxation oscillation*. Along with the turn-on delay time, the relaxation oscillation limits the bit rate of the pulse modulation of the laser.

Referring to Fig. 14.11, let us examine the sequence of changes in the electron as well as the photon densities when a step injection current is applied.

1. As soon as the injection current is turned on, the electron density N starts to increase in accordance with Eq. (14.37) with $S = 0$. No lasing takes place until N reaches N_{th}.
2. When N reaches N_{th}, S begins to respond; however, the response of S is not instantaneous. It takes a few picoseconds for the field to build up in the cavity, and during this build-up time, N overshoots N_{th}.
3. Because N overshoots N_{th}, the rate of increase in S is further accelerated. As soon as S overshoots the steady-state value S_s, J cannot catch up with the consumption of N, and N starts to decay at $t = t_2$. As long as N is larger than N_{th}, S keeps on increasing but at a slower rate. However, as soon as N drops below N_{th} at $t = t_3$, S starts decreasing.
4. When S decays to smaller than S_s at $t = t_4$, N starts increasing because fewer electrons are participating in the stimulated emission.
5. As soon as N reaches N_{th}, S starts increasing and the second cycle of the oscillation begins.
6. In the second cycle of oscillation, S does not have to start from zero, and the time it takes to reach the steady state is less than in the first cycle. Thus, N has less time to go beyond N_{th} than in the first cycle. The amplitude of oscillation in the second cycle is therefore less than that of the first cycle.

14.3.5 Small Signal Amplitude Modulation

One of the biggest advantages of using a semiconductor laser is the ease with which the output is amplitude modulated. It can be modulated by simply modulating the injection current. In this section the modulation characteristics will be investigated using the rate equations.

A steady injection current J_s, set above the threshold current, is applied to the laser diode. A modulation current j is superimposed on the steady value J_s:

$$J = J_s + j \tag{14.63}$$

where

$$j << J_s \tag{14.64}$$

Both N and S deviate from their steady-state values.

$$N = N_{\text{th}} + n \tag{14.65}$$

$$S = S_s + s \tag{14.66}$$

The steady-state values satisfy these two equations:

$$\frac{J_s}{2ed} - S_s b(N_{\text{th}} - N_\alpha) - \frac{N_{\text{th}}}{\tau_n} = 0 \tag{14.67}$$

$$b(N_{\text{th}} - N_\alpha) - \frac{1}{\tau_s} = 0 \tag{14.68}$$

Insertion of Eqs. (14.63) through (14.66) into Eqs. (14.37) and (14.38) and then simplification with Eqs. (14.67) and (14.68) leads to

$$\frac{dn}{dt} = \frac{j}{2ed} - \left(bS_s + \frac{1}{\tau_n}\right) n - b(N_{\text{th}} - N_\alpha)s \tag{14.69}$$

$$\frac{ds}{dt} = bS_s n \tag{14.70}$$

where Eq. (14.68) was used twice for S_s as well as for s and the term with the product ns was ignored. By taking the derivative, the equations for n and s can be separated as

$$\left[\frac{d^2}{dt^2} + \gamma \frac{d}{dt} + \omega_r^2\right] \begin{bmatrix} n \\ s \end{bmatrix} = \begin{bmatrix} \dfrac{1}{2ed}\dfrac{dj}{dt} \\ \dfrac{bS_s}{2ed}j \end{bmatrix} \tag{14.71}$$

where

$$\gamma = \left(bS_s + \frac{1}{\tau_n}\right) \tag{14.72}$$

$$\omega_r^2 = b^2 S_s(N_{\text{th}} - N_\alpha) \tag{14.73}$$

Useful quantities will be obtained by solving Eq. (14.71) in the next few sections.

14.3.5.1 Time Constant of the Relaxation Oscillation

If the relaxation oscillation is to be analyzed properly, then the differential equation (14.71) has to be solved with the proper initial conditions. But if one is simply interested in finding the frequency or decay time of the free oscillation, then one need

only find the solution of the differential equation with the right-hand side of Eq. (14.71) set to zero:

$$\left(\frac{d^2}{dt^2} + \gamma \frac{d}{dt} + \omega_r^2 \right) s = 0 \tag{14.74}$$

Let us assume a solution of the form

$$s = s_0 e^{-j\omega t} \tag{14.75}$$

Inserting Eq. (14.75) into (14.74) gives

$$(-\omega^2 - j\gamma\omega + \omega_r^2)s_0 e^{-j\omega t} = 0 \tag{14.76}$$

and the value of ω that satisfies Eq. (14.76) is

$$\omega = -j\frac{\gamma}{2} \pm \sqrt{\omega_r^2 - \left(\frac{\gamma}{2}\right)^2} \tag{14.77}$$

The final solution is

$$s = s_0 \exp\left[-\frac{\gamma}{2}t \pm j\omega_r \sqrt{1 - \left(\frac{\gamma}{2\omega_r}\right)^2}\, t \right] \tag{14.78}$$

The relaxation oscillation decays as $e^{-(\gamma/2)t}$, where γ is given by Eq. (14.72).

Equation (14.72) for γ will be rewritten in terms of the operational and physical constants associated with the laser. If $N_{th} \gg N_\alpha$ is assumed, Eq. (14.68) becomes

$$bS_s = \frac{S_s}{\tau_s N_{th}} \tag{14.79}$$

Inserting Eqs. (14.48) and (14.53) into Eq. (14.79) gives

$$bS_s = \frac{1}{\tau_n} \frac{J - J_{th}}{J_{th}} \tag{14.80}$$

Insertion of Eq. (14.80) into (14.72) finally gives

$$\gamma = \frac{1}{\tau_n} \left(\frac{J}{J_{th}} \right) \tag{14.81}$$

This result indicates that the relaxation oscillation can be shortened by choosing a larger bias current J and by choosing $\tau_n J_{th}$ small. Let's further rewrite $\tau_n J_{th}$ by using parameters involving the geometry of the laser. From Eq. (14.49) the quantity $\tau_n J_{th}$ becomes

$$\tau_n J_{th} = 2ed \left(N_\alpha + \frac{1}{b}\frac{1}{\tau_s} \right) \tag{14.82}$$

where τ_s in Eq. (14.39) is repeated here,

$$\frac{1}{\tau_s} = v \left(\frac{1}{L} \ln \frac{1}{R} + \alpha \right) \tag{14.83}$$

Thus, $\tau_n J_{\text{th}}$ can be reduced, or equivalently the relaxation oscillation can be shortened by reducing any of the following: the thickness $2d$ of the active layer, N_α, $(1/L) \ln(1/R)$, or α.

14.3.5.2 Amplitude Modulation Characteristics

Let the laser be modulated at frequency ω_m by modulating the injection current density around the bias current J_0,

$$j = j_0 e^{-j\omega_m t} \tag{14.84}$$

The quantity bS_s on the right-hand side of Eq. (14.71) can be rewritten as $bS_s = \omega_r^2/b(N_{\text{th}} - N_\alpha)$ using Eq. (14.73). Combining this result and Eq. (14.68), Eq. (14.71) leads to

$$\frac{d^2 s}{dt^2} + \gamma \frac{ds}{dt} + \omega_r^2 s = \frac{\tau_s \omega_r^2}{2ed} j_0 e^{-j\omega_m t} \tag{14.85}$$

which is the forced vibration equation. The steady-state solution (a particular solution) can be found similar to Eq. (14.75) by assuming a solution

$$s = s_0 e^{-j\omega_m t} \tag{14.86}$$

Inserting Eq. (14.86) into (14.85) gives

$$s = \frac{\tau_s \omega_r^2 j_0}{2ed} \cdot \frac{1}{\sqrt{(\omega_r^2 - \omega_m^2)^2 + (\gamma \omega_m)^2}} e^{-j(\omega_m t + \phi)} \tag{14.87}$$

The magnitude of the modulated light given by Eq. (14.87) has a resonance. The resonance peak appears where the denominator of Eq. (14.87) is at the minimum, which is found by setting the derivative with respect to ω_m to be zero.

$$\omega_m^r = \omega_r \sqrt{1 - \frac{1}{2} \left(\frac{\gamma}{\omega_r} \right)^2} \tag{14.88}$$

By comparing Eq. (14.89) with (14.81), it is seen that $(\gamma/\omega_r)^2$ is much smaller than unity because τ_s is of the order of 10^{-12}s and τ_n is of the order of 10^{-9}s. Thus, the usable modulation bandwidth is more or less the same as ω_r. From a practical point of view, it is important to make ω_m^r or ω_r as large as possible.

As was done for γ, let us express ω_r in terms of the laser operational and physical parameters. The ω_r^2 in Eq. (14.73) can be split into the product of $bS_s \cdot b(N_{\text{th}} - N_\alpha)$. The bS_s term was already found in Eq. (14.80). The $b(N_{\text{th}} - N_\alpha)$ term is found from Eq. (14.68). Thus,

$$\omega_r^2 = \frac{J - J_{\text{th}}}{\tau_s \tau_n J_{\text{th}}} \tag{14.89}$$

The product $\tau_s\tau_n$ appearing in the denominator of Eq. (14.89) is the product of the time for the injected electrons to disappear by spontaneous emission (of the order of nanoseconds) and the time for the photons created by the stimulated emission to disappear after bouncing back and forth between the end mirrors (of the order of picoseconds). The maximum modulation frequency can be achieved by choosing J large, and making both τ_s and $\tau_n J_{th}$ small. The photon lifetime τ_s and the product $\tau_n J_{th}$ become small if $2d$, N_α, $(1/L)\ln(1/R)$, or α are made small, as mentioned in the previous section.

Figure 14.12 gives an example of the measured results [9]. The solid lines correspond to a laser with a 280-μm long cavity, and the dashed lines correspond to a laser with an 80-μm long cavity. The amplitudes of both curves are normalized by the value at $\omega_m = 0$. The laser with the shorter cavity has the shorter photon lifetime and hence a higher limit on the modulation frequency. With both lasers, the modulation frequency limits always increase with an increase in the injection current, as predicted by Eq. (14.89).

14.3.5.3 Comparisons Between Theoretical and Experimental Results
The theories presented thus far will be tested by two practical examples.

Example 14.1 Figure 14.13a is the vendor's specifications for an $Al_x Ga_{1-x}$ As laser diode, and Figs. 14.13b and 14.13c are the experimental results for the turn-on characteristics and the spectrum of this same laser diode. Calculate the theoretical bias voltage to injection current characteristics ($V-I$ curve) and compare it with the experimental curve. The cavity mirrors are cleaved surfaces. The power attenuation constant is $\alpha = 175 cm^{-1}$. The terminal contact resistance is $R = 0.5\ \Omega$. The following step-by-step instructions are intended to lead to the solution.

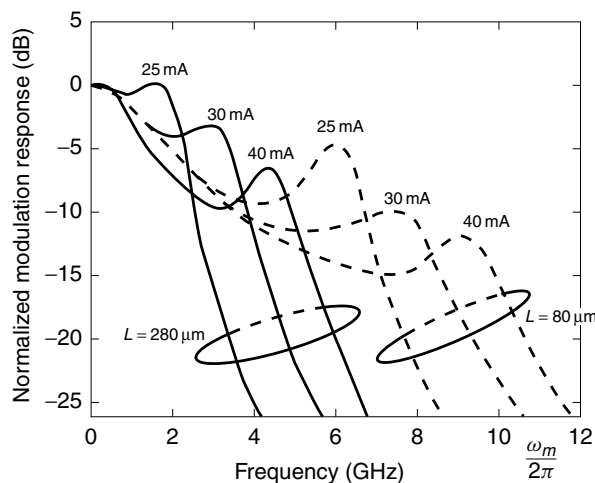**Figure 14.12** Amplitude modulation characteristics of the direct modulation of a laser diode. Solid line $L = 280$ μm. Dashed line $L = 80$ μm. (After R. Tucker, C. Lin, and C. A. Burrus [9].)

ACTUAL SIZE

LAS
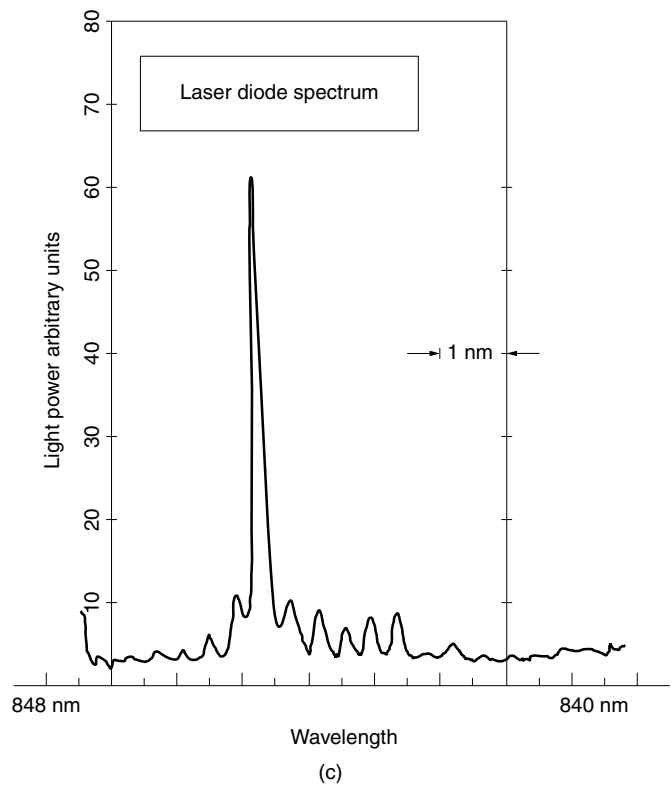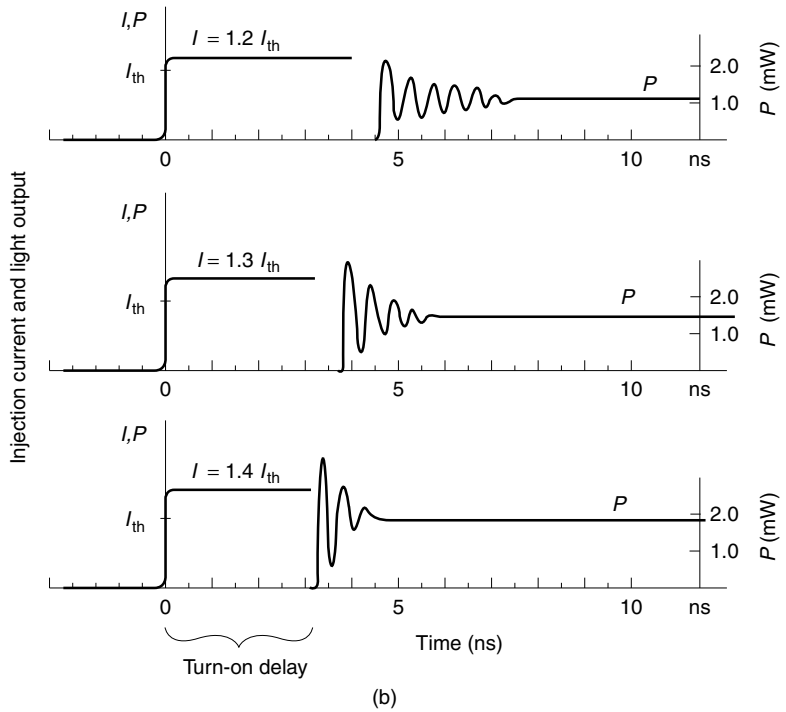
DIODE

TYPE LCW-10
TYPE LCW-10F
with FIBER PIGTAIL
MULTIMODE
GaAIAs CW
INJECTION LASER DIODE

FEATURING:
- CW OPERATION
- UP TO 14 mW OUTPUT POWER ON SELECTED UNITS
- CHOICE OF WAVELENGTH
- HIGH TEMPERATURE OPERATION
- LOW THRESHOLD CURRENT

DESCRIPTION: The LCW-10 is a multimode
CW GaAIAs double heterostructure laser diode.
This device features low threshold current and high output power.
The diodes are passivated for long life and reliability.
They offer good performance at elevated temperatures.
The LCW-10F is the fiber coupled version of the LCW-10.
This unit is available with standard fiber as noted below.
Custom fiber attachment available upon request.

Pom. I.. & I.. Information furnished with each device — Data at 27°C unless otherwise noted.

		Symbol	Min.	Typ.	Max.	Units
Total Radiant	LCW-10	Pom	4	7		mW
Flux at Rated I_1	LCW-10F*	Pom	1	2.0		mW
Peak Wavelength		λ_0	See Below	830	See Below	nm
Spectral Width @ 50% points		$\Delta\lambda$		2.5		nm
Source Size				0.2×7.0		μm
Rise Time of Radiant Flux		T_1		100	800	ps
Far Field Beam Divergence (LCW-10) @ 50% Points		$\theta_1 \times \theta_n$		10×35		degrees
Threshold Current		I_n		30	150	mA
Operating Current		I_v		115	$I_m + 50$	mA
Differential Quantum Efficiency				0.3		mW/mA
Forward Voltage at I_1		V_v		2.0		volts
Operating Temperature		T_n	0		60**	°C
Storage Temperature		T_v	−55		125	°C

*Standard fiber Digtail is all glass. 50 μm graded index core. 125 μm O.D. with N.A. = .20
**Selections to higher operating temperatures are available.

WAVELENGTH SELECTION

OPTION	WAVELENGTH RANGE
A	800 to 810 nm
B	810 to 840 nm
C	840 to 860 nm
D	860 to 880 nm

ABSOLUTE MAXIMUM RATINGS (CW)

Maximum Forward Current = lower of $I_m + 60$ or 210 mA
Maximum Reverse Voltage = 2.0 volts
Maximum Operating Temperature = 70°C
Maximum Storage Temperature = 140°C
Minimum Storage Temperature = 75°C
Maximum Radiant Output Power = 14 mW

(a)

Figure 14.13 Comparison among vendor's specification, experimental results, and theoretical calculations for an $Al_xGa_{1-x}As$ laser diode. (a) Laser diode specifications. (b) Turn-on characteristics of the laser diode. (c) Measured spectrum of the laser diode. (d) Gain curve of $Al_xGa_{1-x}As$. (After H. C. Casey and M. B. Panish [10]). (e) Properties of $Al_xGa_{1-x}As$ crystal.

(b)

Figure 14.13   (*Continued*)

(d)
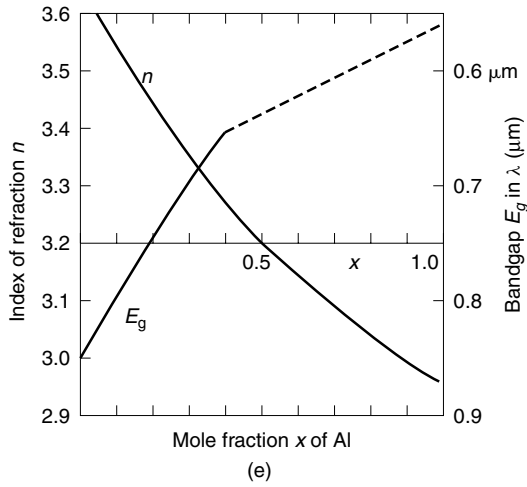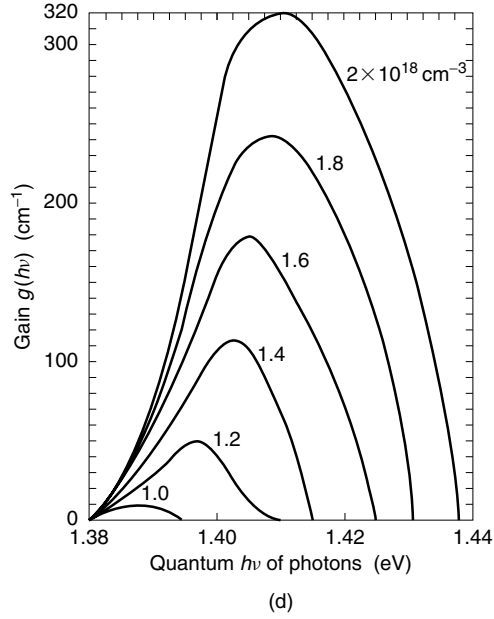

(e)

Figure 14.13   (*Continued*)

(a) Derive an expression that relates the carrier density and the quasi-Fermi levels. Approximate the Fermi–Dirac distribution by the Boltzmann distribution

$$f_c(E_2) = e^{-(E_2 - F_c)/kT} \tag{14.90}$$

so that the integral of Eq. (14.2) can be calculated in a closed form using

$$\int_0^\infty x^{1/2} e^{-x} \, dx = \frac{\sqrt{\pi}}{2} \tag{14.91}$$

(b) The calculations have to be done separately for carrier densities above and below the threshold carrier density. The threshold carrier density is determined by the spontaneous emission lifetime, which is obtainable from the turn-on delay time and the cavity length. The cavity length is obtained from the laser spectrum. The physical and optical properties of $Al_x Ga_{1-x} As$, which are controlled by the molar fraction x of Al, are

$$m_e^* = (0.067 + 0.082x)m_0 \tag{14.92a}$$

$$m_h^* = (0.5 + 0.29x)m_0 \tag{14.92b}$$

$$E_g = 1.424 + 1.247x \text{ eV} \cdot \text{s} \tag{14.92c}$$

$$n = (13.1 - 3x)^{1/2} \tag{14.92d}$$

where m_0 is the electron mass 9.109×10^{-31} kg and n is the index of refraction. The terminal voltage V is related to the difference between the quasi-Ferm levels.

$$eV = F_c - F_v \quad \text{(in electron volts)} \tag{14.93}$$

Solution

(a) With the Boltzmann distribution as an approximate quasi-Fermi distribution, the integrals for the carrier densities become

$$N = \frac{\sqrt{2}}{\hbar^3} \frac{m_e^{*3/2}}{\pi^2} \int_{E_c}^{\infty} (E_2 - E_c)^{1/2} e^{-(E_2 - F_c)/kT} \, dE_2 \tag{14.94}$$

$$P = \frac{\sqrt{2}}{\hbar^3} \frac{m_h^{*3/2}}{\pi^2} \int_{-\infty}^{E_v} (E_v - E_1)^{1/2} e^{-(F_v - E_1)/kT} \, dE_1 \tag{14.95}$$

where Eqs. (14.2) to (14.7) were used, and N and P are the negative and positive carrier densities, respectively. These integrals can be performed by putting

$$\frac{E_2 - E_c}{kT} = x_2$$

and

$$\frac{E_v - E_1}{kT} = x_1$$

The results are

$$N = N_c e^{(F_c - E_c)/kT}$$
$$P = N_v e^{(E_v - F_v)/kT} \tag{14.96}$$

where

$$N_c = 2 \left(\frac{\sqrt{2\pi km_0}}{h} \right)^3 \left(\frac{m_e^*}{m_0} T \right)^{3/2}$$
$$N_v = 2 \left(\frac{\sqrt{2\pi km_0}}{h} \right)^3 \left(\frac{m_h^*}{m_0} T \right)^{3/2} \tag{14.97}$$

Inserting the physical constants gives

$$N_c = 4.817 \times 10^{15} \left(\frac{m_e^*}{m_0} T \right)^{3/2} \text{cm}^{-3}$$

$$N_v = 4.817 \times 10^{15} \left(\frac{m_h^*}{m_0} T \right)^{3/2} \text{cm}^{-3}$$

(14.98)

The densities N_c and N_v are called the effective density of states for the negative and positive carriers, respectively. Comparing with Eq. (14.2) in format, Eq. (14.96) can be interpreted as if the energy states of the carriers are discretely concentrated at E_c and E_v with the density of states N_c and N_v rather than spread across the bands. The carrier densities N and P are simply obtained by multiplying N_c or N_v by $e^{(F_c - E_c)/kT}$ or $e^{(E_v - F_v)/kT}$, which are the quasi-Fermi distribution functions indicating the probability that the E_c and E_v levels are occupied [8]. Electrical neutrality requires

$$N + N_0 = P + P_0$$

(14.99)

where N_0 and P_0 are the densities of n and p dopants, respectively. The active layer is practically undoped so as to lower the loss of the cavity (increasing the doping increases the loss inside the cavity) and, hence,

$$N = P$$

(14.100)

Thus, from Eq. (14.96), the product NP gives

$$F_c - F_v = E_g + kT \ln \left(\frac{N^2}{N_c N_v} \right)$$

(14.101)

This is the desired relationship between the electron density and the Fermi level gap, which gives the terminal voltage V by Eq. (14.93).

In order to calculate m_e^*, m_h^*, and n, the molar fraction x has to be determined. The longest wavelength limit $\lambda = 0.846$ μm of the wavelength spectrum in Fig. 14.13c approximately corresponds to the energy bandgap and

$$E_g = h\nu = 1.467 \text{ eV}$$

where Planck's constant $h = 4.136 \times 10^{-15}$ eV · s in electron volts was used.

From Eq. (14.92c), the molar fraction x is determined to be

$$x = 0.0345$$

and the effective masses become

$$\frac{m_e^*}{m_0} = 0.0698$$

$$\frac{m_h^*}{m_0} = 0.510$$

The effective densities of states at $T = 293$ K are, from Eq. (14.98),

$$N_c = 0.446 \times 10^{18} \text{cm}^{-3}$$

$$N_v = 8.80 \times 10^{18} \text{cm}^{-3}$$

(b) The spontaneous emission lifetime τ_n is found by fitting the curve of Eq. (14.61) with the graphs in Fig. 14.13b. The values used for fitting are tabulated in Table 14.1. The average value is $\tau_n = 2.65$ ns.

Next, the length L of the cavity will be found using Fig. 14.13c. From Eq. (14.34), the cavity length is

$$L = \frac{\lambda^2}{2n \; \Delta\lambda}$$

Inserting $x = 0.0345$ into Eq. (14.92), the index of refraction is found to be $n = 3.6$. The wavelength λ and the separation between longitudinal modes $\Delta\lambda$ are read from Fig. 14.13c. Thus, the cavity length is

$$L = 248 \; \mu\text{m}$$

First, the $V-I$ curve below threshold will be found. Using Eq. (14.48), and letting w denote the width of the laser cavity as shown in Fig. 14.7, the relationship between injection current I and N is

$$
\begin{aligned}
N &= \tau_n \frac{I}{wL} \frac{1}{2ed} \\
&= 2.65 \times 10^{-9} \frac{I}{(7 \times 10^{-6})(248 \times 10^{-6})(1.6 \times 10^{-19})(0.2 \times 10^{-6})} \\
&= 4.77 \times 10^{25} I/\text{m}^3
\end{aligned}
\qquad (14.102)
$$

Hence, the carrier density (in cm^3) is

$$N = 4.77 \times 10^{19} I/\text{cm}^3$$

Inserting this result and N_c and N_v into Eq. (14.101) gives

$$F_c - F_v = (1.628 + 50.57 \times 10^{-3} \ln I) \text{ eV} \qquad (14.103)$$

where $I = 0$ is excluded and where Boltzmann's constant $k = 8.63 \times 10^{-5}$ eV/mol $\cdot$ K in electron volts was used.

Table 14.1   Turn-on delay time and output light power versus J/J_{th}

$\dfrac{J}{J_{th}}$	t_d (ns)	τ_n (ns)	P (mW)
1.2	4.8	2.67	1.1
1.3	3.9	2.66	1.47
1.4	3.3	2.63	1.92

The amount of time for one man to finish a workload of 5 man-months is 5 months. Similarly, if one electron possesses 5 eV of energy, then that electron has a potential of 5 volts.

Since $F_c - F_v$ is in electron volts, the bias voltage V_b that can give $(F_c - F_v)$ eV is, from Eq. (14.93),

$$eV_b = (F_c - F_v) \text{ eV}$$

The potential V of each electron is

$$V_b = (F_c - F_v) \text{ volts}$$

Keep in mind that N does not exceed N_{th}. Thus, from Eq. (14.101), V_b stops increasing as soon as N reaches N_{th}, no matter how I is increased, as the measured curve in Fig. 14.14 indicates.

Next, the threshold carrier density and the corresponding threshold current will be found. From Eq. (14.29) at threshold, the gain satisfies

$$g_{\text{th}} = \frac{1}{L} \ln \frac{1}{R} + \alpha$$
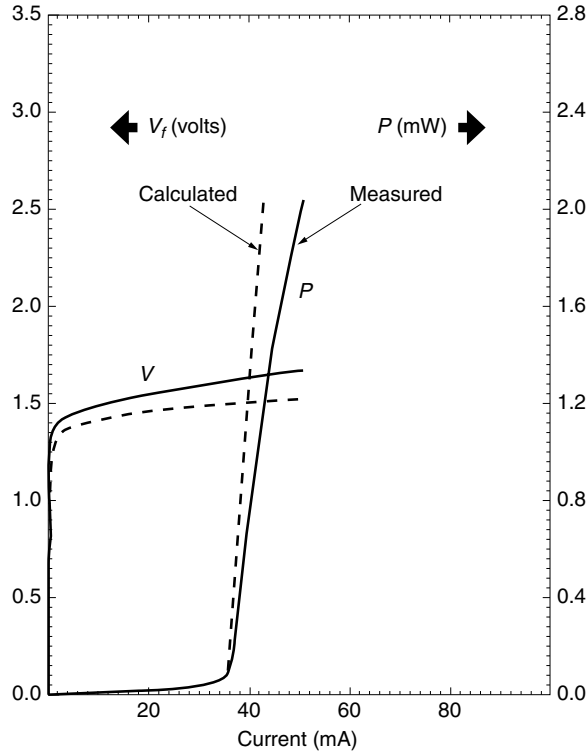
Figure 14.14 Measured (solid line) and calculated (dashed line) V–I curve and P–I curve of an $Al_x Ga_{1-x} As$ laser diode.

With the given value $\alpha = 175\text{cm}^{-1}$, the threshold gain becomes

$$g_{\text{th}} = 221 \text{ cm}^{-1}$$

The gain spectrum in Fig. 14.13d [10] is replotted as a function of the carrier density in Fig. 14.15. The curve is quite linear. The threshold electron density for $g = 221 \text{ cm}^{-1}$ is

$$N_{\text{th}} = 1.7 \times 10^{18} \text{ cm}^{-3}$$

The current needed to supply N_{th} is

$$I_{\text{th}} = \frac{wL2ed}{\tau_n} N_{\text{th}}$$

From Eq. (14.102),

$$I_{\text{th}} = 35.6 \text{ mA}$$

which is close to the measured value. The corresponding terminal voltage is 1.459 volts from Eq. (14.103). The external terminal potential V_e is

$$V_e = \begin{cases} IR + (F_c - F_v) \text{ volts} & \begin{array}{l} \text{below the threshold,} \\ I < 35.6 \text{ mA} \end{array} \\ IR + 1.459 \text{ volts} & \begin{array}{l} \text{above the threshold,} \\ I > 35.6 \text{ mA} \end{array} \end{cases}$$

Using Eq. (14.103), the calculated and measured V_e are compared in Table 14.2. □
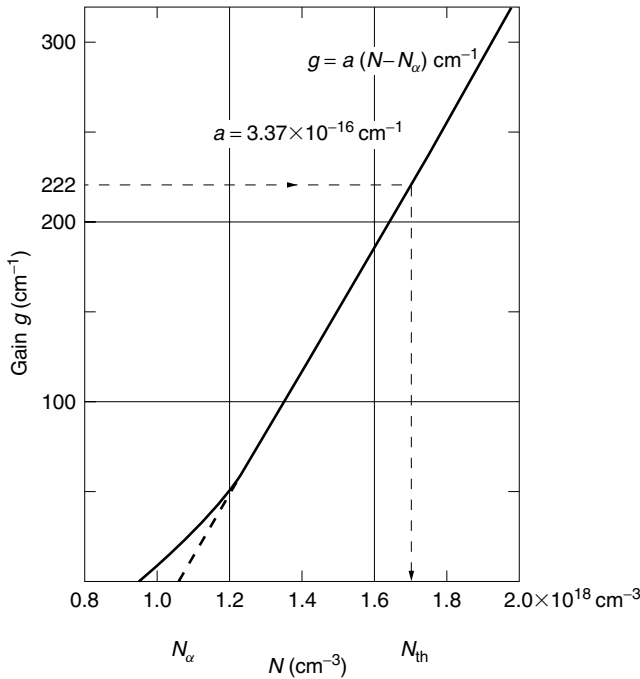
Figure 14.15 Linearized gain with respect to the carrier density N for GaAs.

Table 14.2   Terminal voltage compared to injection current

I (mA)	IR (volts)	$F_c - F_v$ (volts)	Calculated V_e (volts)	Measured V_e (volts)
10^{-1}	0.5×10^{-4}	1.159	1.159	1.15
1	0.5×10^{-3}	1.275	1.275	1.35
2	10^{-3}	1.310	1.311	1.37
5	2.5×10^{-3}	1.357	1.360	1.42
35	17.5×10^{-3}	1.459	1.477	1.58
50	25×10^{-3}	1.459	1.484	1.62

Example 14.2

(a) With the same laser diode as studied in Example 14.1, obtain the theoretical light output versus injection current curve.

(b) Calculate ω_r and $1/\gamma$ at $I = 1.4 I_{\text{th}}$. Compare the theoretical rise time t_r with the value in the specification sheet. The rise time t_r is related to the cutoff frequency f_m^r of the modulation by Eq. (16.85) as

$$t_r f_m^r = 0.35$$

Solution

(a) The output power is given by Eq. (14.58). From Eqs. (14.39) and (14.55) the output power is

$$P_{\text{out}} = E_g \frac{\dfrac{1}{L} \ln \dfrac{1}{R}}{\dfrac{1}{L} \ln \dfrac{1}{R} + \alpha} (I - I_{\text{th}}) \text{ W} \tag{14.104}$$

Insertion of the parameters gives

$$P_{\text{out}} = 0.31(I - I_{\text{th}}) \text{ W}$$

The calculated results are plotted with the experimental curve in Fig. 14.14. The theoretical curve puts out slightly more power than the experimental curve.

(b) The parameter γ is given by Eq. (14.81) and τ_n is obtained from Table 14.1.

$$\frac{1}{\gamma} = 1.9 \times 10^{-9} \text{s}$$

The frequency ω_r is given by Eq. (14.89) and τ_s is given by Eq. (14.83):

$$\omega_r = 1.657 \times 10^{10} \text{ rad/s}$$

$$f_r = 2.63 \text{ GHz}$$

From Eq. (14.88),

$$f_m^r = 2.629 \text{ GHz}$$

The rise time is

$$t_r = \frac{0.35}{2.629 \times 10^9} = 0.133 \times 10^{-9}\text{s} = 133 \text{ ps}$$

The datasheet in Fig. 14.13a gives a rise time of 100 ps.   □

14.4 CONFINEMENT

The overall dimensions of the laser diode shown in Fig. 14.7 are typically $200 \times 200 \text{ }\mu\text{m}^2$ in base and 75 μm in height with an active region typically 0.1–0.2 μm thick, 200 μm long, and 10 μm wide. Compared to most types of lasers, the dimensions of the laser diode are indeed very small. In this small region, one has to confine carriers, injection current, and photons.

For best performance, it is essential to confine all three quantities effectively. Proper design of the confinement is one of the most decisive factors in laser diode performance. Effective confinement lowers the threshold current. As discussed earlier, lowering the threshold current J_{th} shortens both the turn-on delay time and the period of the relaxation oscillation and raises the upper limit of the modulation frequency. A lower threshold current also means that less thermal heat is generated, thereby reducing heat sink problems and the temperature dependence of the performance. The sections to follow look at ways to achieve the desired confinement of carriers, injection current, and photons.

14.4.1 Carrier Confinement

In order to build a high-efficiency laser diode, it is important to maintain maximum carrier density with minimum injection current. The double heterojunction is formed by sandwiching the active layer by layers with a wider energy bandgap. Potential barriers formed by the wider energy bandgap material bounce back the carriers once injected into this region and confine the injected carriers inside the active layer. Thus, a high carrier concentration is established in the active layer. In Fig. 14.16, three kinds of junctions are compared, and these are (a) the homojunction, (b) the single heterojunction, and (c) the double heterojunction. The top row diagrams are the energy bands before the p-n junction is formed, those in the middle are the energy bands after the junction is formed, and those on the bottom are the energy bands when a forward bias is applied.

The operation of the homojunction, which is the basis of all others, will be explained first. As soon as the n- and p-type layers are joined, electrons that are majority carriers in the n-type layer start diffusing into the p-type layer as minority carriers. Conversely, holes in the p-type layer start diffusing into the n-type layer.

The diffusion causes a redistribution of the carriers, and as a consequence, a potential difference is established between p- and n-type layers. To understand the origin of this potential difference, let us once again consider the n-type material before it is joined. For every electron that breaks loose from the n-type atom to become a negative carrier, there is a positively charged immobile ion left behind. Thus, overall, the n layer is electrically neutral. In the same way, the p layer is also electrically neutral before it is joined. For every positive carrier (hole) that is created, a negatively charged immobile
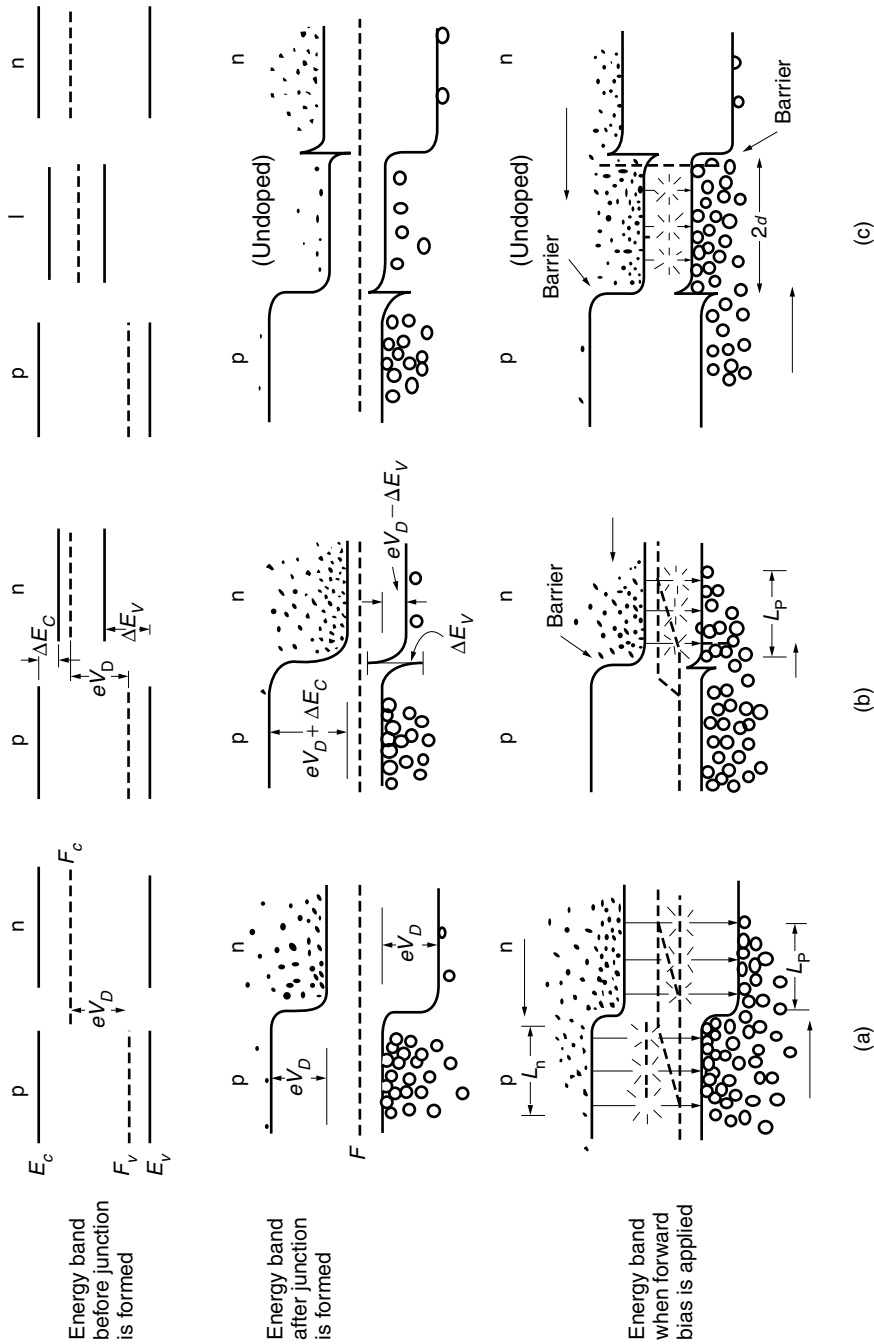
Energy band
before junction
is formed

Energy band
after junction
is formed

Energy band
when forward
bias is applied

E_c

F_c

F_v

E_v

F

n

p

eV_D

eV_D

eV_D

L_n

L_p

(a)

p

n

ΔE_C

ΔE_V

eV_D

$eV_D + \Delta E_C$

$eV_D - \Delta E_V$

ΔE_V

Barrier

L_p

(b)

p

n

(Undoped)

(Undoped)

Barrier

Barrier

$2d$

(c)

Figure 14.16 Comparison of three kinds of p-n junctions. (a) Homojunction. (b) Single heterojunction. (c) Double heterojunction.

ion is left behind in the crystal lattice. As soon as the contact is made, electrons in the n-type layer diffuse into the p-type layer, leaving immobile positively charged ions behind. As a result, the n-type layer starts to have a positive potential. For the same reason, the diffusion of the holes from the p-type layer into the n-type layer results in charging the p-type layer to a negative potential. The potential difference V_D between the two layers is called the *diffusion potential* or *contact potential*.

The diffusion of the electrons does not go on forever. As the diffusion progresses, the diffusion potential also keeps increasing. The polarity of the diffusion potential is such that the associated Coulomb force on the carriers is in the opposite direction to the direction of the diffusion force. At the equilibrium of the two forces, the movement of the electrons and holes ceases. At equilibrium, the Fermi levels in the two layers line up as shown in the middle row of Fig. 14.16, but steps are created between the energy levels. When a forward bias is applied, the steps of the energy levels are decreased. Electrons in the n-type layer start flowing into the p layer, and the holes in the opposite direction. As the flow of electrons penetrates into the p region, the electrons have a chance to recombine with a sea of holes and to emit light by spontaneous emission. The density of electrons decays as e^{-x/L_n} (exponentially with distance of penetration) where L_n is the diffusion length of electrons. The region of emission is spread over approximately L_n from the junction. Similarly, the diffusion length of the holes in the n-type layer is L_p. In the case of the homojunction, both p- and n-type layers near the junction emit light, and the region of emission is spread over approximately $L_n + L_p$.

Next, the function of the heterojunction will be explained. The heterojunction is made of p- and n-type layers with different energy bandgaps as shown in Fig. 14.16b. The middle diagram shows the configuration of the energy bands after the junction is made. The Fermi levels of p and n layers line up with each other. The band structure of the p layer moves up. The conduction band of the p layer becomes higher than that of the n layer.

The final shape of the conduction band can be drawn by smoothly connecting the conduction bands of the two layers. The shape of the valence band near the junction can be obtained by drawing lines parallel to those of the conduction band. As a consequence, the step between the conduction bands of the p- and n-type layers is $eV_D + \Delta E_c$ where ΔE_c is due to the original difference of the conduction bands between the p and n layers. This step is larger than eV_D of the homojunction. The step between the valence bands of the p- and n-type layers is $eV_D - \Delta E_v$, which is smaller than eV_D of the homojunction. When a forward bias is applied to the junction, there is an imbalance between the flow of electrons and holes because of the imbalance between the height of steps in the conduction and valence bands as indicated in the bottom diagram. The electrons hardly penetrate into the p-type layer because of the barrier, but holes are able to penetrate the n-type layer. Hence, the recombination takes place only in the n-type layer in a region within L_p from the junction, as shown in Fig. 14.16b. The region of recombination is reduced to roughly half, compared to the homojunction, and the carrier concentration can be doubled for the same injection current.

Finally, the double heterojunction will be explained. The double heterojunction consists of two single heterojunctions on both sides of the active region, as shown in Fig. 14.16c. As shown in the middle figure, the junction between the p-type layer and the center layer makes a barrier against electrons while the junction between the n-type layer and the center layer makes a barrier against holes. When a forward bias is

applied, holes migrate from the p-type layer to the center layer, and electrons migrate from the n-type layer to the center layer. However, penetration of carriers from the center layer to the outer layers is effectively blocked by the barriers. It is only in the center layer that both electrons and holes are present for recombination. The region of emission is concentrated in this center region of thickness $2d$. The carrier concentration $N = \tau_n J / 2ed$ in Eq. (14.44) can be raised by choosing a small thickness $2d$. The value of $2d$ is normally 0.1–0.2 μm. Compared to the homojunction $L_n + L_p = 6$ μm and single heterojunction $L_p = 3$ μm, the carrier density of the double heterojunction can be 30–60 times greater for the same current.

It is worthwhile at this point to look at some specific examples of commonly used materials for p-n junctions. Examples of host semiconductor materials include crystals of valence 4 atoms such as germanium (Ge) or silicon (Si), and compounds made of equal numbers of valence 3 and 5 atoms such as gallium arsenide (GaAs) and indium phosphide (InP). A variation of the latter is to use a mixture of valence 3 atoms in combination with the appropriate number of valence 5 atoms, as in $Al_xGa_{1-x}As$, where x is the molar fraction of Al atoms. With a Ge or Si crystal, an n-type semiconductor is formed by adding an impurity to the host of valence 5 or greater like P, As, or Sb, and a p-type semiconductor is formed by adding an impurity of valence 3 or less like B or Ga. A configuration that is often used for the double heterostructure is to use GaAs as the center layer, with p-doped $Al_xGa_{1-x}As$ on one side, and n-doped $Al_xGa_{1-x}As$ on the other side. In the case of the double heterojunction formed by $Al_xGa_{1-x}As$, the energy bandgap is changed by the molar fraction x. Aside from the increase in the energy bandgap, an increase in x results in a decrease in the refractive index of the layer.

It may be added that if the thickness $2d$ of the active layer in the double heterojunction is further reduced to the order of 10 nm, the motion of the electrons becomes restricted and the quantized nature of the energy levels must be taken into account. In this case, the double heterojunction becomes a quantum well laser that displays different features in threshold current, bit rate, and temperature dependency and will be described in more detail in Section 14.12.

14.4.2 Confinement of the Injection Current

Any injection current that flows in a region other than the designed active region increases the apparent threshold current. In order to keep the threshold current low, the injection current has to be confined to the desired region.

Various ingenious methods of funneling the current into the active region of the laser diode have been reported [11]. Five examples will be presented:

1. Narrow stripe electrode.
2. Raised resistivity by proton bombardment.
3. Barricade by a back-biased p-n junction layer.
4. Dopant-diffused channel.
5. Modulation of layer thickness.

A brief description of each method will be presented with illustrations. In all the illustrations, the coding for the shaded areas will be unified. The n-type region will be

indicated by slashing down to the left, and the p-type region by slashing down to the right.

14.4.2.1 Narrow Stripe Electrode

Figure 14.17a shows the structure of the electrode stripe laser. This structure is the simplest of all types. The narrowness of the electrode is a means of confinement. Lasers whose active region lateral dimension (width) ranges from 10 to 20 μm can use this configuration. An insulating layer of SiO_2 is deposited except for the center stripe region. A metal layer is then deposited that serves as the 10–20 μm wide electrode. Even though the deposition of SiO_2 as the insulator is simple, a drawback is the low heat conductivity.

14.4.2.2 Raised Resistivity by Proton Bombardment

Electrons are funneled into a narrow region by a resistivity wall. The resistivity of a semiconductor can be raised locally by bombarding the semiconductor with high-energy
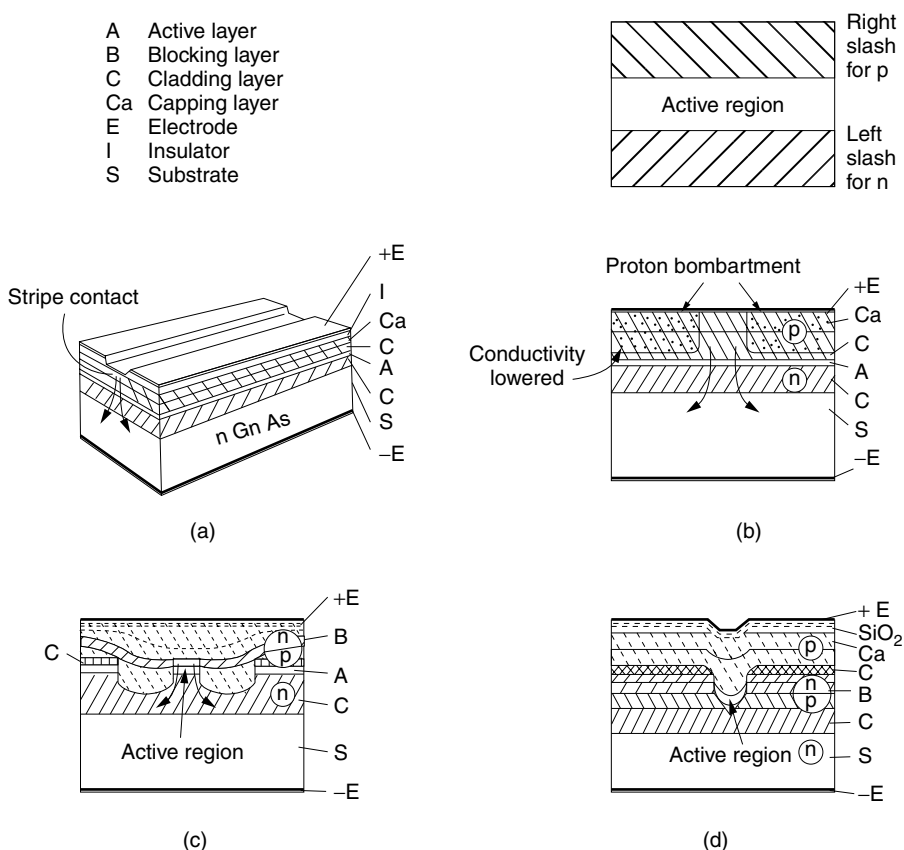
Figure 14.17 Geometries of laser diodes. (a) Electrode stripe laser. (b) Proton bombarded stripe laser. (c) Double-channel planar buried heterostructure (DC-PBH) laser. (d) Buried crescent (BC) laser. (e) Channeled substrate planar (CSP) laser. (f) V-grooved substrate buried heterostructure (VSB) laser. (g) Terraced substrate (TS) laser. (h) Stripe substrate laser. (i) Transverse junction stripe (TJS) laser. (j) Constricted double heterojunction (CDH) laser.
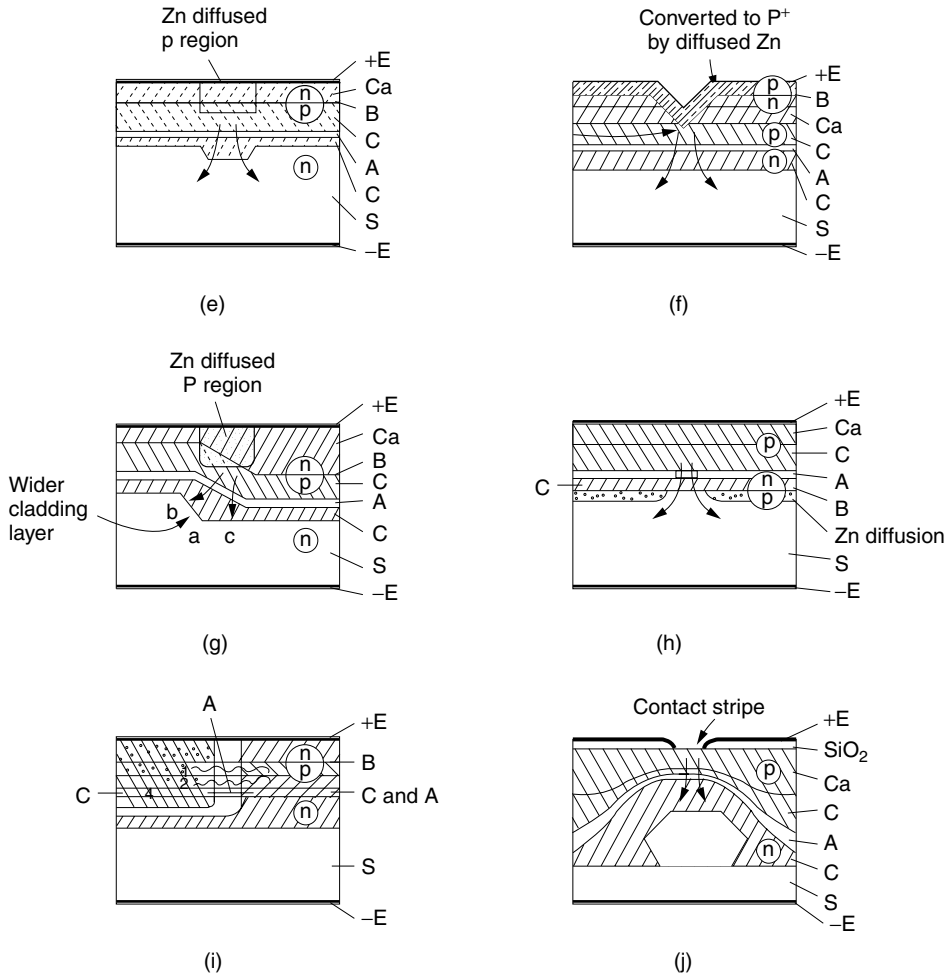
Figure 14.17   (*Continued*)

protons. Figure 14.17b shows the cross section of a proton-bombarded stripe laser. The proton-bombarded region has increased resistivity due to the damage caused by the bombardment. The injected current is funneled into the region that has escaped the bombardment. In some designs, the bombardment is allowed to penetrate as far as the active layer for even tighter confinement. Another advantage of this method is better heat conduction than the SiO_2 insulator used in the previous method.

Test results [12] show that the 10-Ω resistance of the n-type GaAs becomes 10^8 Ω after bombardment with a 3-MeV proton beam of dose $10^{13}/cm^2$. The resistivity increases 10^7 times.

14.4.2.3 *Barricade by a Back-Biased p-n Junction Layer*
When a p-n junction is back-biased, the current is blocked by the high impedance across the junction. The aperture made on the barricade provides confined electrons. The simplest example is the case when the SiO_2 layer in Fig. 14.17a is replaced by an

n-type semiconductor layer so that the top two semiconductor layers form a back-biased p-n junction. The technique of the back-biased p-n junction is widely used, and a few types of lasers that use this technique are included here.

The structure of the double-channel planar buried heterostructure (DC-PBH) laser is fabricated as shown in Figs. 14.17c. The current cannot pass through the blocking p-n junction layer indicated by B and flows through the top surface of the mesa.

Another laser that uses the blocking p-n junction is the buried crescent (BC) laser [13] shown in Fig. 14.17d. Only the active layer inside the V groove will lase, as the current cannot get to the active layer on the sides because of the blocking p-n junction underneath indicated by B. A stripe electrode is used to reinforce the confinement of the injection current. This laser gets its name from the fact that the active layer is shaped like a crescent rather than a rectangle.

The method of the back-biased p-n junction is used more often in combination with the method of the diffusion of dopants than by itself. Windows for the current are created by locally converting the p-n junction into either a p-p junction or an n-n junction by diffusing dopants, as will be explained in the next section.

14.4.2.4   Dopant-Diffused Channel

The conversion is done locally by diffusing the dopants. Diffusion of either zinc (Zn) or cadmium (Cd) (group II) is commonly used to convert the semiconductor to p-type, and sulfur (S) (group VI) to convert to n-type. The channeled substrate planar (CSP) laser shown in Fig. 14.17e uses this method. In the center region, Zn is diffused through the p-n blocking layer. The n layer is converted into a p-type semiconductor and the underlying p layer becomes more strongly p type. The current channel is thus created in the center. This current channel is sometimes extended close to the active region for better confinement of the current.

Another type of laser that uses the same diffusion technique is the V-grooved substrate buried heterostructure (VSB) laser shown in Fig. 14.17f. The V groove is made so that only the tip of the Zn-diffused p-type region reaches the p-type layer of the laser. Thus, the size of the current window is small for better confinement.

The terraced substrate (TS) laser shown in Fig. 14.17g is another example. A substrate with a step in the center is used. On the substrate, the layers are grown in the same order as other types. The Zn-diffused p region directly connects the positive electrode to the p layer to form a current channel. The active region is tilted so that the cladding layer is wider near the center of the active region. As will be explained in the next section, the tapered width of the cladding layer improves the confinement of the photons inside the active layer.

The stripe substrate laser shown in Fig. 14.17h uses the dopant layer differently. The Zn-diffused p layer is not used to open a channel; rather, it is used as a component layer of the blocking p-n junction. The surface of the substrate is first treated by Zn diffusion to create a p-type layer except for a narrow region in the center. An n-type layer, followed by an active layer, followed by a p-type layer, is grown to form a laser with a current channel in the center.

The transverse junction stripe (TJS) laser [14] shown in Fig. 14.17i uses not only Zn diffusion but also the differences in the forward-biased p-n junction impedance. The top two layers form a back-biased p-n junction and no current flows vertically. The extensively Zn-diffused upper left section becomes a p^+ region. Between the left and right regions in the third and fifth layers, p-n junctions are created.

All possible paths below the blocking p-n layer are indicated by the wavy arrows in Fig. 14.17i. Even though all paths are forward-biased p-n junctions, the active region indicated by a straight arrow has the least impedance because of the narrower energy bandgap of the C layer material, and the injection current is confined to flow horizontally through the active layer.

14.4.2.5 Modulation of the Layer Thickness

The constricted double heterojunction (CDH) laser shown in Fig. 14.17j takes a slightly different approach to confine injection current. A difference in resistivity is established by the differences in layer thickness. The cladding−active−cladding layers are grown over a substrate that has a protrusion on the top surface. Both the cladding and the active layers are made thinnest in the center section so that the resistivity is the lowest, and the current selectively flows in the center.

14.4.3 Light Confinement

Since the laser light is amplified by going back and forth in the active region, it is important for the light to be properly confined in the active region in both the transverse (vertical) and lateral (horizontal) directions. Let us first deal with transverse confinement.

In designing the transverse dimension (thickness) of the active layer, the following considerations are made:

1. Because the higher order modes create side lobes in the radiation pattern of the laser that make the coupling of the laser output into an optical fiber more difficult, the fundamental mode is used exclusively. The upper limit on the thickness $t = 2d$ is determined from the cutoff of the first higher order mode. From Eq. (9.32), the thickness must satisfy

$$t \leq \frac{\lambda}{2\sqrt{n_1^2 - n_2^2}} \tag{14.105}$$

2. Deciding the thickness of the active layer is a compromise between a higher efficiency of the active layer and a narrow beamwidth of the output light.

From these two considerations the thickness of the active layer is selected to be around $0.1-0.2$ μm for most lasers in the range of $0.85-1.55$ μm.

Light confinement in the vertical (transverse) direction is achieved by means of refractive index guiding, which is based on total internal reflection from the boundaries between the core and cladding layers. Refractive index guiding can be used to confine the light in the lateral (horizontal) direction as well. An alternate approach for lateral confinement is to use gain guiding, a technique that is unique to lasers. The following few sections will concentrate on lateral light confinement.

14.4.3.1 Gain Guiding

The stripe electrode laser will be used for the sake of explanation. Figure 14.18 shows the carrier concentration distribution $N(y)$, the gain distribution $g(y)$, and the refractive index distribution $n(y)$ also with respect to the y (lateral) axis for the case that J is
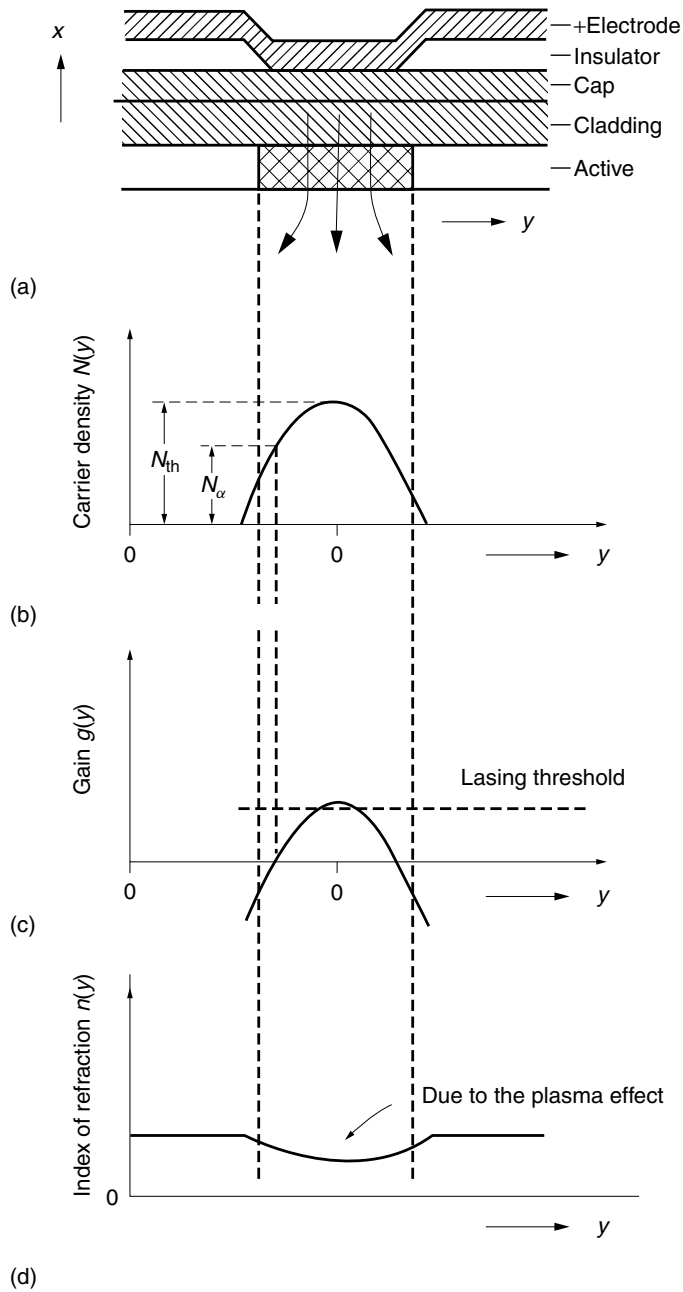
Figure 14.18 Stripe electrode laser and the distribution function of parameters: carrier concentration in the center creates an index dip due to the plasma effect. (a) Active region. (b) Carrier density distribution. (c) Gain distribution. (d) Distribution of the index of refraction.

slightly above J_{th} at $y = 0$. The injection current density J is at its maximum in the center and almost zero at both sides of the active region. The distribution of the carrier concentration roughly follows the current distribution. The gain $g(y)$, in turn, follows the distribution of the carrier concentration in accordance with

$$g(y) = a[N(y) - N_\alpha] \tag{14.106}$$

In short, the $g(y)$ curve more or less follows that of J, except that the curve is lowered by aN_α. As the junction current is increased, $g(y)$ increases and the maximum of $g(y)$ located in the center first reaches the threshold and initiates lasing at the center. The photons now become available for stimulation. The intensity of generated photons is also highest in the center region. The combination of high gain and high stimulated emission further accelerates the stimulating emission near the center. Thus, once the lasing starts near the center where the gain is maximum, the location of the lasing is pinned down at that location even without other light-guiding mechanisms. Such a phenomenon that lasing stays in the region of the highest gain is called *gain guiding*. The gain-guiding principle can be utilized as the sole guiding mechanism, but one has to be aware of potentially undesirable side effects, which include the carrier-induced plasma effect, hole burning, and self-focusing. These are discussed in the sections to follow.

14.4.3.2 *Plasma-Induced Carrier Effect*
Being charged particles, the carriers are subjected to Coulomb's force by the electric field **E** of the lightwave. Oscillation of the charges creates an oscillating polarization. The phase of the oscillation, however, is shifted from the applied field due to the mass inertia of the electrons. The oscillating electrons with the shifted phase decrease the index of refraction (see boxed note). This reduction of the refractive index is called the *plasma effect* of the electrons. The quantitative expression for the decrease in the refractive index due to the plasma effect is

$$\Delta n = \frac{e^2 N}{2\omega^2 \epsilon_0 \epsilon_r m_e^*} n \tag{14.107}$$

where N is the electron concentration, n is the refractive index in the absence of the plasma effect, $\epsilon_0 \epsilon_r$ is the dielectric constant of the active region, and m_e^* is the effective mass of the electron. The coefficient of Eq. (14.107) becomes $\sim 10^{-2}$ with $N = 10^{25}$ m^{-3}, and $\Delta n/n$ is about 1%. Considering the fact that the refractive index step that confines the light in the core of the optical fiber is only 0.5%, the plasma effect is of a comparable magnitude.

The refractive index distribution has a shallow minimum at the center due to the plasma effect, as shown at the bottom of Fig. 14.18. This index dip tends to diverge the light beam, and the divergent beam moves out of the region and does not lase. The light beam that remains in the center does lase, as long as threshold conditions continue to be satisfied. The net result is that the gain guiding keeps the light beam in the center. However, the situation becomes more complex when J is increased well above J_{th}, as will be shown next.

An extremely simplified proof of Eq. (14.107) will be presented here. Let the **E** field of the light be represented by

$$\mathbf{E} = \mathbf{E_0}e^{-j\omega t} \tag{14.108}$$

The equation of motion due to the Coulomb force exerted by **E** on a particular electron with charge e and effective mass m_e^* is

$$m_e^* \frac{dv}{dt} = eE_{ox}e^{-j\omega t} \tag{14.109}$$

where the direction of the x axis is taken in the same direction as **E**. It is also assumed that there are no collisions between the electrons that impede the motion of the electron. Insertion of Eq. (14.108) into (14.109) followed by integration gives

$$v = j\frac{eE_{ox}}{\omega m_e^*}e^{-j\omega t} \tag{14.110}$$
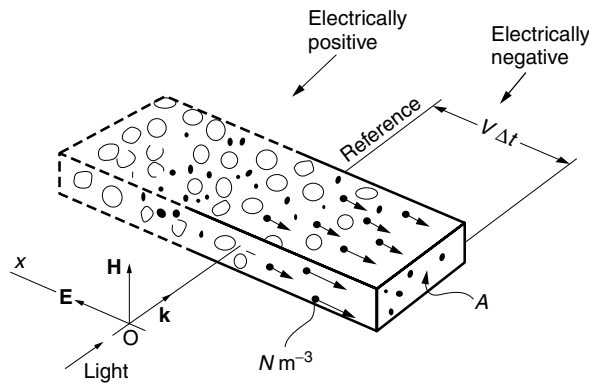
Figure 14.19 The movement of charge across a reference cross section is the plasma current.

In a short time Δt this particular electron moves a distance $v\Delta t$. In the absence of collisions, all electrons move by the same amount $v\Delta t$, leaving the heavy ions behind. With reference to a particular cross section, the total volume of electrons that are pushed out is $Av\Delta t$, as shown in Fig. 14.19. The total charge ΔQ that has moved through the reference cross section is

$$\Delta Q = eNAv\Delta t \tag{14.111}$$

The density J_{px} of the plasma current, which is the movement of the charges across a unit area of the reference cross section, is

$$J_{px} = \frac{1}{A}\frac{\Delta Q}{\Delta t} \tag{14.112}$$

Inserting Eqs. (14.110) and (14.111) into Eq. (14.112) gives

$$J_{px} = j\frac{e^2}{\omega m_e^*}NE_{ox}e^{-j\omega t} \tag{14.113}$$

More generally,

$$\mathbf{J_p} = j\frac{e^2}{\omega m_e^*}N\mathbf{E}$$

The oscillation of the free electrons contributes to the total current, and Maxwell's equation becomes

$$\nabla \times \mathbf{H} = j\frac{e^2}{\omega m_e^*}N\mathbf{E} + \frac{d\mathbf{D}}{dt} \tag{14.114}$$

Using Eq. (14.108) in (14.114) leads to

$$\nabla \times \mathbf{H} = -j\omega\epsilon_0\epsilon_r\left(1 - \frac{e^2 N}{\omega^2\epsilon_0\epsilon_r m_e^*}\right)\mathbf{E} \tag{14.115}$$

The value in the large parentheses is unity when $N = 0$. One way of looking at Eq. (14.115) is that it is Maxwell's equation with a modified dielectric constant. In terms of the refractive index $n = \sqrt{\epsilon_r}$, the modified index of refraction n' is

$$n' = n\sqrt{1 - \frac{e^2 N}{\omega^2\epsilon_0\epsilon_r m_e^*}}$$

Finally, $\Delta n = n' - n$ is approximated as

$$\Delta n = \frac{e^2 N}{2\omega^2\epsilon_0\epsilon_r m_e^*}n \tag{14.116}$$

14.4.3.3 Kink in the Characteristic Curve

Another phenomenon closely related to the lateral mode confinement is a kink appearing in the curve of the light output versus injection current. As the injection current is increased, the distributions of the refractive index, carrier concentration, and light intensity all pass through various states. The transitions of these changes are shown in Fig. 14.20. The curves in Fig. 14.20a are with the least injection current and Figs. 14.20b and 14.20c are with larger injection currents. The gain guiding explained in Fig. 14.18 was for an injection current slightly above threshold and corresponds to the case in between Figs. 14.20a and 14.20b.

As the injection current is increased above the threshold, the number of electron–hole pairs that are annihilated by stimulated emission increases nonlinearly. The supply of electrons from the injection current cannot keep up with the rate of annihilation, and the distribution curve of the carrier concentration starts to have a dip in the center, as indicated in Fig. 14.20b. Another way of explaining this is to draw upon the results of Section 14.3.2, where it was shown that, in the region of lasing, the carrier concentration stays clamped at N_{th} no matter how high J is increased above J_{th}. The dip in the carrier concentration curve is called *hole burning*. Where the hole burning takes place, the index of refraction is raised because of the reduction in the plasma effect and a local maximum is formed, as indicated by the bottom graph in Fig. 14.20b. This local maximum of the refractive index forms a light-guiding structure that steers the light toward the center and creates a further shortage of carriers in the center, which in turn raises the index of refraction and steers even more light toward the center. These repeated actions confine the light tightly in the center. This phenomenon is called *self-focusing*. As self-focusing sets in, there is a certain range in which an increase in injection current does not effectively increase the light output because the lasing is confined only to the place where the carrier concentration is low.
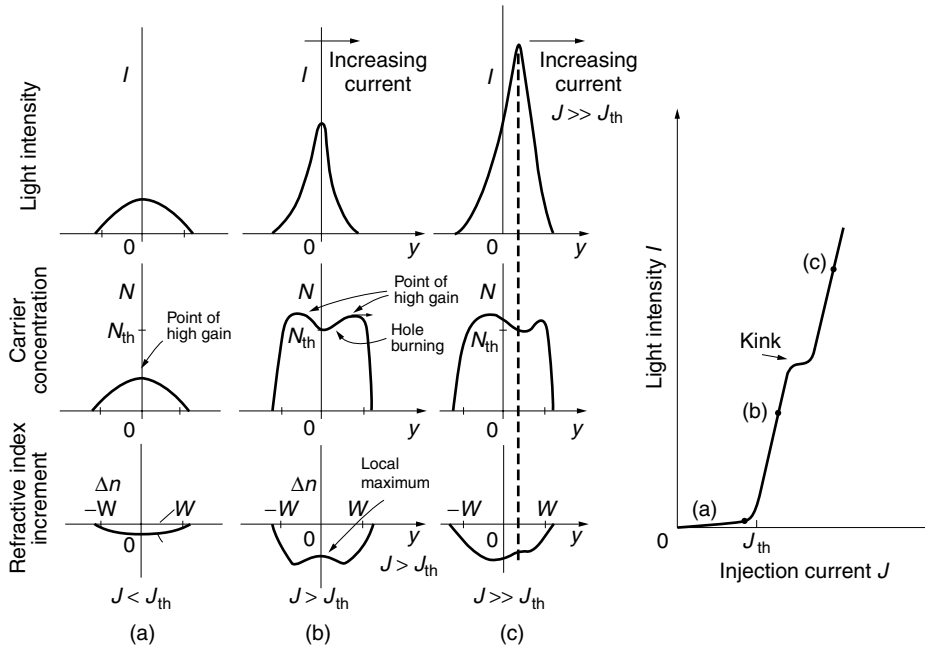
Figure 14.20 Lateral light confinement in a diode laser. (a) Below threshold. (b) Self-focusing. (c) Competition between self-focusing and gain guiding.

This ineffective increase in the light output is displayed as a kink in the curve of light output versus injection current, as shown in the right-hand side of Fig. 14.20.

Because of the hole burning in the center, the distribution of the carrier concentration builds up the maxima on both edges of the active region, as shown in the middle figure in Fig. 14.20b. These maxima of the carrier concentration have the potential to become gain guiding, because a higher carrier concentration is more susceptible to gain guiding. Now the laser beam has a choice to stay in the center by the self-focusing or to move toward the edge by the gain guiding, as shown in Fig. 14.20c. Thus, this distribution of the carrier concentration creates an instability. Even a slight fluctuation triggers the shift of the light beam to the two peaks of the carrier concentration curve, and the light beam will be divided into two beams inside the active region. If the active region is wide enough to support the higher order modes, the next higher order mode that has two intensity peaks will start to be excited. The division of the light intensity creates undesirable side lobes in the radiation pattern of the laser.

14.4.3.4 Stabilization of the Lateral Modes

The kink in the characteristic curve can be removed by preventing the hole burning of the carriers. The first method to prevent the hole burning is to decrease the width of the active region to a value less than the diffusion length of the carriers. The width of the active region should be less than $1-2$ μm.

Another method is to use dielectric waveguiding instead of gain guiding, namely, to use the refractive index step between the active region and its adjacent media in the horizontal direction as well as in the vertical direction. The buried heterostructure type lasers such as the DC-PBH laser in Fig. 14.17c and the BC laser in Fig. 14.17d
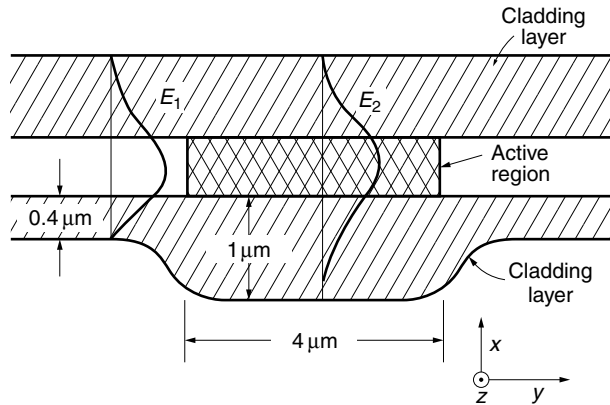
Figure 14.21   Waveguide for laterally confining the light in the active layer of a CSP laser. (After H. Yonezu [8].)

are good examples. The active regions of all these lasers are fenced in by a medium of lower refractive index on all four sides.

An example of a waveguiding method of a special kind is the CSP laser shown in Fig. 14.17e. An enlarged view is shown in Fig. 14.21. The lightwave is confined by a waveguide structure. The width of the bottom cladding layer is constricted to about 0.4 μm all along the bottom except for the active region in the center. The thickness of the cladding layer in the center is about 1 μm, and the width of the thicker center region is about 4 μm. In the region of the constricted cladding layer, the tail of the evanescent wave is pushed up toward the active layer, and the effective index of refraction in the region of the thinner cladding layer is smaller than that of the thicker central cladding region, just like the strip-loaded guide mentioned in Section 10.5.3, thus forming a dielectric waveguide effect in the horizontal direction.

The next few sections will be devoted to the description of the properties of semiconductor lasers.

14.5   WAVELENGTH SHIFT OF THE RADIATION

There are many reasons why wavelength purity and stability are important light source attributes. Material and waveguide dispersion deteriorates the transmission capacity of fiber-optic communication, and a narrow bandwidth of the wavelength of the laser source can minimize these dispersion effects. The requirement for wavelength stability of the source becomes even more severe when the communication system employs superheterodyne detection. A slight drift in the wavelength of the local oscillator laser diode causes the IF frequency to walk out of the IF amplifier bandwidth (see Section 12.6.1).

Wavelength division multiplexing is another example of a system requiring a stable frequency source (see Section 16.3.1). Wavelength division multiplexing is used to expand the capacity of fiber-optic transmission, and an unstable source wavelength creates problems of crosstalk between channels. Yet another problem can arise when the source is modulated. When a laser is amplitude modulated by directly modulating

the injection current, an undesirable frequency modulation results. This is because the wavelength of the laser is dependent on the injection current.

The wavelength of the laser oscillation is determined by $\lambda = 2nL/p$ from Eq. (14.33); therefore, any wavelength shifts are either due to n, p, or L. It so happens that for semiconductor lasers the amount of heat expansion in L is a negligible effect, and n and p are the only two parameters that have to be considered. They are influenced by injection current and temperature. While the injection current lowers the refractive index n due to the plasma effect, the temperature raises n. The mode number p shifts due to the temperature dependence of the gain curve.

The wavelength shift due to n is continuous, while that due to p is discontinuous with respect to the injection current. The two cases will be treated separately.

14.5.1   Continuous Wavelength Shift with Respect to Injection Current

Figure 14.22 illustrates the change in wavelength versus injection current in the horizontal plane and the corresponding output light spectrum in the vertical axis. While the injection current is low and below the threshold current, the carrier concentration increases linearly with the injection current. As the carrier concentration increases, the plasma effect becomes important. The plasma effect lowers the refractive index of the active region by Δn_p. Thus, the resonance wavelength of the cavity *decreases* with injection current in the region below threshold according to Eq. (14.33). This effect continues until the injection current reaches the threshold.

As the injection current is increased beyond the threshold, the carrier concentration no longer increases but remains clamped at N_{th} (See Section 14.3.2), and hence the
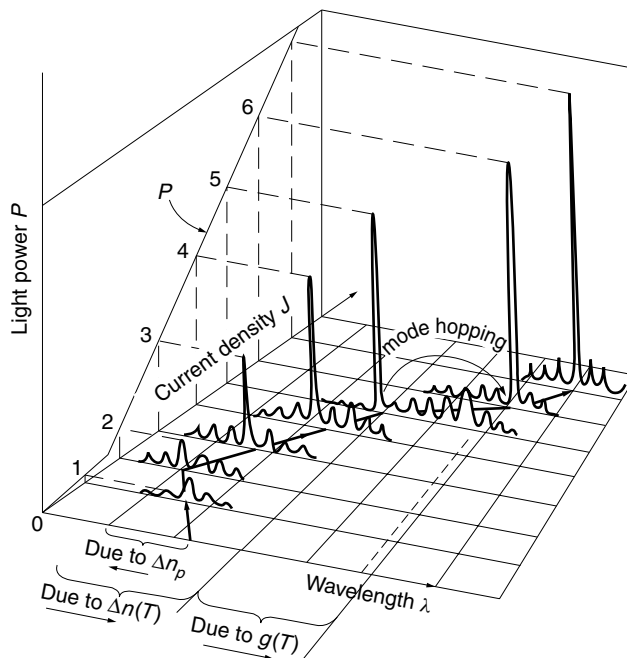
Figure 14.22   Shift of the power spectrum of a laser diode with respect to the injection current.

plasma effect stops increasing. With a further increase in the injection current, the temperature effect that increases the refractive index takes over, and the resonant wavelength of the cavity *increases*. This reverses the direction of the spectrum shift with respect to the injection current in Fig. 14.22.

Now, with a further increase in the injection current, the maximum of the gain curve starts to shift toward the longer wavelengths because the bandgap energy $E_g(T)$ is reduced with an increase in temperature T [15].

$$E_g(T) = E_0 - \frac{\alpha T^2}{\beta + T} \tag{14.117}$$

where E_0 is the bandgap energy at 0 K, T is the temperature in kelvin units, α is 4.5×10^{-4} eV/K, and β is 204 K for GaAs and 327 K for $Ga_x In_{1-x} As_y P_{1-y}$.

The wavelength of the peak gain *increases* approximately 0.23 nm per degree for a multimode laser and 0.1 nm per degree for a single-mode laser.

14.5.2 Mode Hopping

As far as the longitudinal modes are concerned, there are three basic types of laser diodes. The first type is a true single-mode laser, where only one longitudinal mode oscillates. The second is a "quasi" single-mode laser, where several longitudinal modes oscillate, but only one mode dominates, as shown in Fig. 14.9c. The third type is truly multimode, where several modes oscillate, and no one mode has a large dominance over its neighboring modes. This discussion will concern the second type. Once a laser diode starts lasing at a particular wavelength, the stimulated emission tends to stay at that wavelength until the center of the gain curve shifts by a large amount. When the wavelength does shift due to the temperature rise, it hops one or more longitudinal modes, even with less than a few milliampere additional increase in injection current. This shift is a discrete jump, as opposed to the previous shifts, which were continuous. This phenomenon is called *mode hopping*.

The mode hopping in the single-mode laser will be illustrated in more detail using Fig. 14.23. Figure 14.23a shows the shape of the gain curve when oscillating in the p_nth longitudinal mode at one temperature. The gain curve has a dip around the wavelength of emission. This is because the heavy consumption of the carriers that participate in the transition of $h\nu_{p_n}$ affects the supply of carriers that participate in the transition near $h\nu_{p_n}$. This dip is called *spectral hole burning*. Because of the spectral hole burning near the center of the gain curve, even though the maximum of the gain curve shifts gradually with temperature, the wavelength of the oscillation hops with increasing injection current in such a sequence as shown in Figs. 14.23b and 14.23c [8].

In the high injection current region, a hysteresis phenomenon is observed in the curve that represents the wavelength versus injection current. The light wavelength follows a different path for increasing current than for decreasing current. This is partially explained by the fact that once the laser starts lasing at a particular wavelength, the stimulated emission tends to stay at that wavelength.

One of the effective countermeasures against mode hopping is mode locking that uses a cladding layer doped with a nonlinear saturable absorber like a Te compound [16] or a multi-quantum-well layer deposited on one of the end reflectors [17]. At lower light intensities the absorber absorbs light, but at higher intensities, the absorber becomes saturated and no longer absorbs. Once one mode establishes a pattern at a high power level, it stays in that mode because of the lower loss.
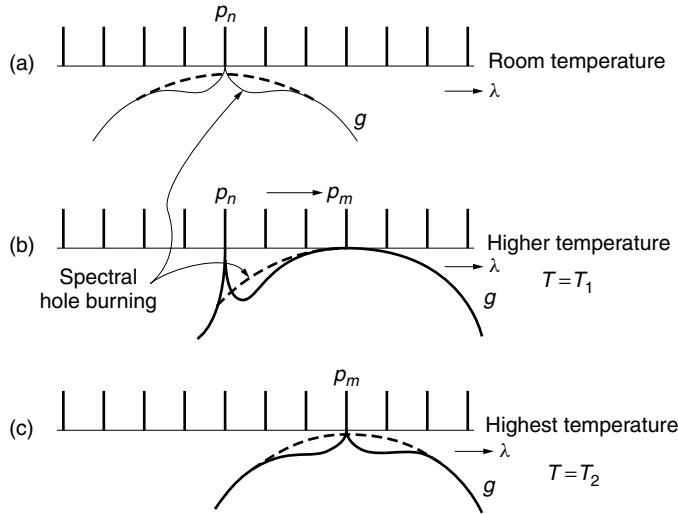
Figure 14.23 Illustration of mode hopping. (After H. Yonezu [8].)

Another method of reducing the wavelength shift due to the temperature effect is to use an externally servocontrolled thermoelectric cooling element.

14.6 BEAM PATTERN OF A LASER

It is important to design the beam pattern of a laser so as to efficiently couple its output power into an optical fiber or any other optical component. For now, the radiation pattern in only the vertical direction (in the x direction in Fig. 14.7) will be considered. As explained in Section 1.2, the expression for the beam pattern is essentially the Fourier transform of the aperture field of the laser.

$$E(\theta) = \frac{1}{j\lambda z} \int_{-\infty}^{\infty} E(x)e^{-j2\pi fx}\, dx\bigg|_{f=(\sin\theta)/\lambda} \qquad (14.118)$$

where $E(x)$ is the aperture field of the laser in the x direction and $\exp[jk(z_i + x_i^2/2z_i)]$ is suppressed.

Figure 14.24 summarizes the beam patterns for typical one-dimensional aperture field distributions $E(x)$. Figure 14.24a is the beam pattern of a rectangular aperture field distribution

$$E(x) = \Pi\left(\frac{x}{w}\right) \qquad (14.119)$$

where w is the width of the aperture field. Insertion of Eq. (14.119) into (14.118) gives the beam pattern in the vertical plane.

$$E(\theta) = \frac{1}{j\lambda z} w\,\mathrm{sinc}\left(w\frac{\sin\theta}{\lambda}\right) \qquad (14.120)$$
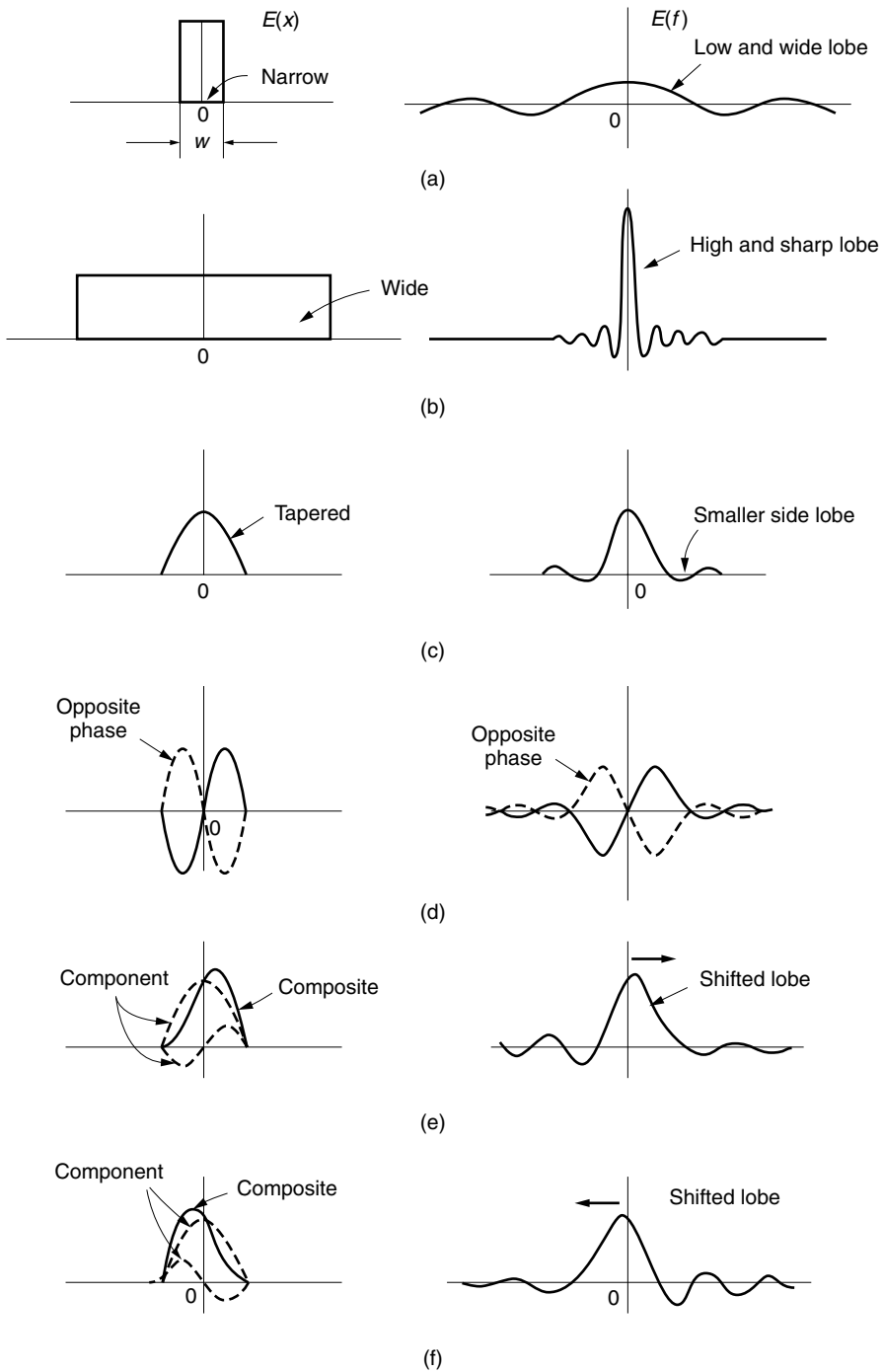
Figure 14.24 Aperture field $E(x)$ and corresponding far-field distribution $E(f)$. (a) Narrow aperture. (b) Wide aperture. (c) Single sinusoidal hump. (d) Double sinusoidal hump. (e) Single + double humps. (f) Single + double (opposite phase) humps.

The beamwidth, which is defined as the width between the nulls of the main lobe, is

$$\Delta\theta = 2\sin^{-1}\left(\frac{\lambda}{w}\right) \tag{14.121}$$

Recognize from Eqs. (14.120) and (14.121) that if a narrow beam is desired, the aperture field w has to be wide, as shown in Fig. 14.24.

It must be cautioned that the width of the aperture field is in general different from the thickness of the active layer of the laser because of the contribution of the evanescent field in the cladding layers. In fact, the spread of the evanescent field is significantly beyond the thickness of the active layer, as will be illustrated in Example 14.3.

Next, the sinusoidal hump aperture field shown in Fig. 14.24c is taken as an example to explain the case when the amplitude is tapered from the center toward the edges of the aperture.

$$E(x) = \Pi(x)\cos(\pi x) \tag{14.122}$$

$$E(\theta) = \frac{1}{2j\lambda z_i}\left[\text{sinc}\left(\frac{\sin\theta}{\lambda} - \frac{1}{2}\right) + \text{sinc}\left(\frac{\sin\theta}{\lambda} + \frac{1}{2}\right)\right] \tag{14.123}$$

For the derivation of Eq. (14.123), see Problem 1.4.

Compared to the case of the rectangular aperture field $\Pi(x)$, the beam of the tapered aperture field has much lower side lobe levels, but the beamwidth is slightly broadened. The lower side lobe levels usually mean better coupling to the optical fiber.

Next, the aperture intensity distribution with two humps, as shown in Fig. 14.24d, will be examined in order to gain some insight into the case when the laser output contains higher transverse modes. The aperture amplitude distribution is

$$E(x) = \Pi(x)\sin(2\pi x) \tag{14.124}$$

The radiation field is

$$E(\theta) = \frac{1}{2\lambda z_i}\left[\text{sinc}\left(\frac{\sin\theta}{\lambda} + 1\right) - \text{sinc}\left(\frac{\sin\theta}{\lambda} - 1\right)\right] \tag{14.125}$$

As shown in Fig. 14.25d, the null appears in the center of the main lobe. This is because the contribution of the aperture field of positive sign exactly cancels the contribution of the negative sign along the centerline. As a matter of fact, any mode with an antisymmetric aperture distribution creates a null in the center of the main lobe, whereas modes with symmetric distributions have a maximum in the center.

Next, the superposition of Figs. 14.24c and 14.24d is considered, as shown in Figs. 14.24e and 14.24f. This situation approximates the case when the active layer of the laser is excited by the fundamental and the next higher order mode. The resultant radiation pattern is distorted and shifted from the center. The direction of the shift depends on the phase of the higher order mode with respect to the fundamental mode. Disturbances such as temperature changes in the active layer affect the phase relationship between the modes so that the central radiation lobe appears to jitter. If the optical fiber does not accept the whole radiation pattern from the laser, this jitter causes a fluctuation in the input power to the fiber and creates noise in the fiber-optic
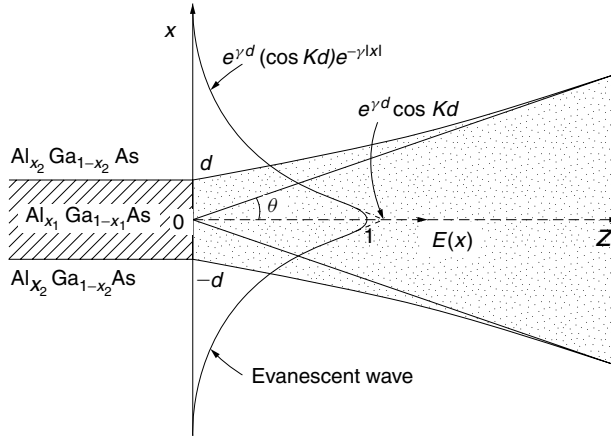
Figure 14.25   Distribution of aperture field intensity.

system. This kind of noise is called the *modal noise* of the laser. Lasers in which only the fundamental mode is excited are naturally free from modal noise.

Example 14.3 Al_xGa_{1-x} As is used for both the active and cladding layers of a laser diode but with different values of fractional molar values of x. If the thickness $2d$ of the active layer is 0.1 μm, what should be the values of x for the active layer and cladding so that the laser oscillates with a half-power beamwidth of $\pm 17°$? The wavelength of oscillation is $\lambda = 0.84$ μm and the bandgap energy for the active layer is 1.462 eV. Assume that the normalized thickness V of the active layer is smaller than $\pi/8$ radians, and assume that the aperture field can be approximated by the expression

$$E(x) = e^{\gamma d}(\cos Kd)e^{-\gamma|x|} \tag{14.126}$$

for both active and cladding layers, as indicated in Fig. 14.25. The TE mode will be used.

Solution   The beam pattern is found by inserting Eq. (14.126) into (14.118), but one has to be careful about the absolute value sign. The integral has to be performed for the positive and negative regions separately.

$$|x| = \begin{cases} x & \text{for } x > 0 \\ -x & \text{for } x < 0 \end{cases}$$

$$E(\theta) = C \left[\int_{-\infty}^{0} e^{\gamma x - j2\pi f x}\, dx + \int_{0}^{\infty} e^{-\gamma x - j2\pi f x}\, dx \right]_{f=(\sin\theta)/\lambda} \tag{14.127}$$

where

$$C = \frac{1}{j\lambda z_i} e^{\gamma d} \cos Kd$$

The result of the integration is

$$E(\theta) = C \frac{2\gamma}{\gamma^2 + (k\sin\theta)^2} \tag{14.128}$$

Normalizing Eq. (14.128) by $E(0)$ gives

$$\frac{E(\theta)}{E(0)} = \frac{1}{1 + \left(\dfrac{k \sin \theta}{\gamma}\right)^2} \tag{14.129}$$

The angle θ_b for the half-power is

$$\left(\frac{E(\theta_b)}{E(0)}\right)^2 = \tfrac{1}{2} \tag{14.130}$$

Equations (14.129) and (14.130) give

$$\sin \theta_b = \frac{\gamma}{k}(\sqrt{2} - 1)^{1/2} \tag{14.131}$$

Equation (14.131) means that as γ is decreased the laser beam pattern sharpens. This is because the depth of penetration $1/\gamma$ of the evanescent wave into the cladding layer is increased and the source size is increased.

Next, an approximate expression for γ will be found. Since the second term on the left-hand side of Eq. (9.27), $(Kd)^2 + (\gamma d)^2 = V^2$, is nonnegative, and since $V < \pi/8$ as stated in the problem, then

$$Kd < \frac{\pi}{8} \tag{14.132}$$

which enables us to approximate

$$\tan Kd \doteqdot Kd \tag{14.133}$$

with less than 5% error. This approximation in Eq. (9.61), $\gamma d = Kd \tan Kd$, gives

$$\frac{\gamma}{K} \doteqdot Kd \tag{14.134}$$

Equation (9.27) can be written as

$$V^2 = (Kd)^2 \left[1 + \left(\frac{\gamma}{K}\right)^2\right] \tag{14.135}$$

The second term on the right-hand side in square brackets can be neglected because $Kd < \pi/8$ in Eq. (14.134). Approximating Eq. (14.135) as $V^2 = (Kd)^2$ and using Eq. (9.28), $V = kd\sqrt{n_1^2 - n_2^2}$, leads to

$$K \doteqdot k\sqrt{n_1^2 - n_2^2} \tag{14.136}$$

Finally, putting Eq. (14.136) back into (14.134) gives

$$\gamma = k^2(n_1^2 - n_2^2)d \tag{14.137}$$

Now, let us calculate the fractional molar value x_1 for the active layer. The value of x for $\lambda = 0.84$ μm and $E_g = 1.464$ eV is, from Eq. (14.92c),

$$x_1 = 0.03 \tag{14.138}$$

and n_1 is, from Eq. (14.92d),

$$n_1 = 3.61 \tag{14.139}$$

The necessary equations and numbers are now available to allow us to determine x_2. Equation (14.131) determines the value of γ for a given θ_b. With $\theta_b = 17°$, $\gamma = 3.40 \ \mu\text{m}^{-1}$ or the penetration depth $1/\gamma = 0.29 \ \mu\text{m}$, which is about three times the thickness of the active layer. The value of n_2 is calculated by introducing the parameters found so far into Eq. (14.137):

$$n_2 = 3.44 \tag{14.140}$$

From Eq. (14.92d), the fractional molar value for the cladding layer is finally $x_2 = 0.42$. The answers are

$$x_1 = 0.03$$
$$x_2 = 0.42 \qquad \square$$

14.7   TEMPERATURE DEPENDENCE OF L–I CURVES

One of the weakest points of the semiconductor laser is the strong dependence of the output power on temperature. Figure 14.26 shows the general pattern of the change in the curves of the output power versus bias current with temperature as a parameter [18]. As the temperature increases, the threshold current increases, and the slope quantum efficiency η (or external quantum efficiency) decreases. The slope quantum efficiency η is the derivative of the light output with respect to the injection current at an operating point. Almost all physical parameters depend on the temperature and an analytic expression is too cumbersome to be practical.

An amazing fact, however, is that simple empirical formulas match quite well with the measured characteristics of almost all types of lasers. These empirical formulas are

$$I_{\text{th}} = I_{\text{th0}} e^{T/T_0} \tag{14.141}$$

$$\eta = \eta_0 e^{-T/T_0'} \tag{14.142}$$

where T_0 and T_0' are called the characteristic temperatures of the threshold current and the external quantum efficiency, respectively. I_{th0} and η_0 are the threshold current and the external quantum efficiency projected to zero temperature.

The fluctuation of the output power due to temperature can be estimated immediately for a given I_{th0}, η_0, T_0, and T_0' by noting the fact

$$P = \eta(I - I_{\text{th}}) \quad \text{for } I > I_{\text{th}} \tag{14.143}$$

Insertion of Eqs. (14.141) and (14.142) into Eq. (14.143) gives the temperature fluctuation of the output power of the laser:

$$\frac{P(T + \Delta T)}{P(T)} = e^{-\Delta T/T_0'} \left(1 + \frac{1 - e^{\Delta T/T_0}}{m - 1} \right) \tag{14.144}$$
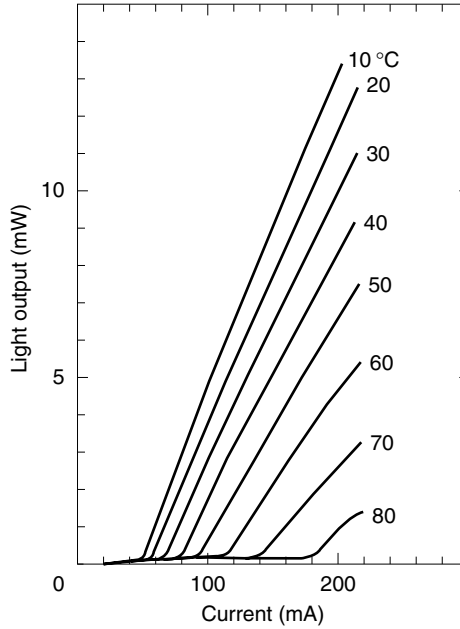
Figure 14.26   Temperature dependence of the L–I curve. (After M. Kitamura et al. [18].)

where

$$m = \frac{I}{I_{th0}e^{T/T_0}} = \frac{I}{I_{th}} \tag{14.145}$$

The factor m is called the *overdrive parameter*. The conclusion of Eq. (14.144) is that the larger m is, or equivalently, the smaller the I_{th} of the laser is, the less the temperature-induced power fluctuation of the laser is. This is another important reason why the threshold current of the semiconductor laser has to be kept as low as possible. (Other reasons were a fast turn-on time in Section 14.3.4.1, a faster decay time of the relaxation oscillation in Section 14.3.5.1, and a higher modulation frequency in Section 14.3.5.2.)

The power fluctuation of a GaAs laser is around 2 dB for a temperature excursion of 25 °C. It is much larger than the fluctuation of a light-emitting diode (LED) for the same temperature excursion. Most fiber-optic communication systems require a power stability of better than 0.5 dB. To meet these stability requirements, an electronic circuit for automatic power control (APC) is necessary.

14.8   SEMICONDUCTOR LASER NOISE

Fluctuations in amplitude (AM noise), in frequency (FM noise), and in phase (PM noise) accompany almost all radiating sources to varying degrees. The laser diode is no exception. The importance of the noise depends on how the laser diode is used. What is significant for one application may be insignificant for another application. The same holds true for different techniques used within the same application. For example,

when digital intensity modulation is employed in an optical communication system, the laser noise has little influence on the performance of the system. However, when analog modulation is employed, a much higher signal to noise ratio is demanded, and the laser noise has to be carefully considered. When the laser diode is used as a local oscillator laser, the noise of the laser diode becomes an important entity regardless of whether digital or analog modulation is used. In short, the significance of the noise consideration depends on the usage of the laser.

The following are the major causes of noise from a laser diode:

1. Noise due to external optical feedback.
2. Noise associated with relaxation oscillation.
3. Noise due to mode hopping.
4. Partition noise.
5. Noise due to spontaneous emission.
6. Noise due to fluctuations in temperature and injection current.

14.8.1   Noise Due to External Optical Feedback

The reflectivity R of the mirror of the semiconductor laser is normally small for the benefit of a shorter photon lifetime τ_s, which leads to a higher limit on the modulation frequency ω_0. The smaller R, however, means that the light reflected from the load easily enters inside the active region and the operation of the laser is critically influenced by the reflected wave.

Let us first consider the case where the external reflector [19] is within a few centimeters of the laser, and externally and internally reflected waves are coherent. With the optical feedback, ripples appear in the light power P versus injection current I curve, as shown in Fig. 14.27. The period of the ripple becomes shorter as the reflector moves away from the laser. The cause of the ripple is the external optical feedback. As the injection current is increased, the wavelength of oscillation is shifted (see Section 14.5.1). The phase relationship between the externally reflected and internally reflected waves alternates between in phase and out of phase. If the reflected wave enters the laser in phase with the internal wave that has just reflected from the laser cavity mirror, both waves enhance each other in the active region of the laser and the reflectivity of the mirror is effectively increased. The increase in the effective reflectivity of the mirror increases the lifetime τ_s of photons inside the cavity and, according to Eq. (14.53), increases the output light. Thus, the ripples appear in the P–I curve.

Now consider what happens when the distance between the external reflector and the laser is increased well beyond a few centimeters. Assume for the time being that the light remains coherent. For large distances, the noise appears even for a nominally fixed injection current. The phase ϕ of the wave reflected from the distance L is $\phi = 4\pi L/\lambda$. The change in phase $\Delta\phi$ for a change in wavelength $\Delta\lambda$ is
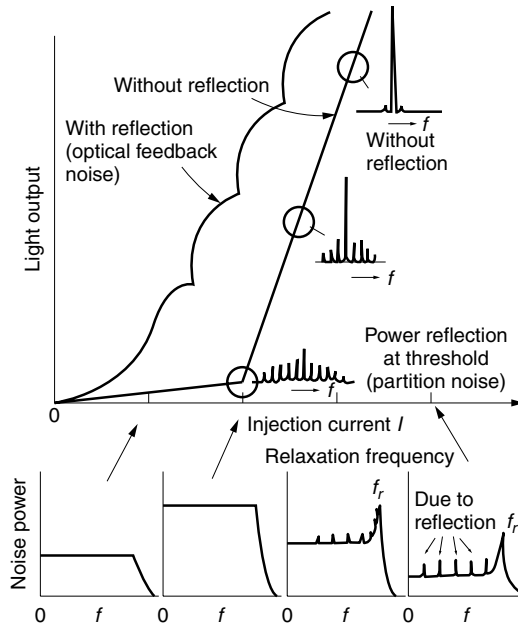
$$\Delta\phi = \frac{d\phi}{d\lambda}\Delta\lambda$$

Figure 14.27 Laser diode noise.

and

$$\Delta\phi = -4\pi \frac{L}{\lambda} \frac{\Delta\lambda}{\lambda} \qquad (14.146)$$

$\Delta\phi$ is accentuated by a factor of L/λ. This is called the *long-line effect*. For a kilometer-long fiber, the value of L/λ is as large as 10^9 and the wavelength fluctuations due to the current supply or temperature become large enough to change the condition of the interference between the internally and externally reflected waves. This noise appears clearly as notches in the frequency spectrum shown at the bottom of Fig. 14.27.

The countermeasures against the noise due to external optical feedback are:

1. The use of an isolator that prevents the reflected wave from entering the laser diode. The only drawback of this method is that it adds complexity to the fabrication.
2. An increase in the reflectivity R of the end mirrors reduces the noise. The increase in R, however, increases τ_s by Eq. (14.83) and this method is at the sacrifice of lowering the limit of the frequency of amplitude modulation, Eq. (14.89).
3. Removal of the coherency of the output light reduces the noise, at the cost of a reduction in the useful frequency bandwidth. Choose a multilongitudinal mode laser or single longitudinal mode laser whose spectral purity is intentionally degraded by introducing a few hundred megahertz modulation to the injection current [8].
4. Avoid external reflectors wherever possible. If it is not possible to avoid them, reduce the reflectivities of the external reflectors by such methods as antireflective coatings or index-matching fluids.

14.8.2 Noise Associated with Relaxation Oscillation

Relaxation noise occurs when the laser diode is directly pulse modulated by modulating the current. Every time the current pulse is on, the carrier density oscillates in such a way as shown in Fig. 14.11b. This oscillation modulates the plasma effect in the active region of the laser, and the resonance frequency of the cavity is modulated accordingly. This phenomenon is known as the *chirp noise* associated with direct pulse modulation. The countermeasure is to operate the laser at a higher current in order to increase γ in Eq. (14.81) and quickly attenuate the relaxation oscillation.

14.8.3 Noise Due to Mode Hopping

Mode hopping was explained in Section 14.5.2. Every time the transition from one mode to another occurs, the frequency as well as the amplitude of the oscillation jumps. Mode hopping creates both AM and FM noise. As mentioned in Section 14.5.2, the countermeasures are the use of a saturable cladding layer or tight temperature control by a servolooped thermoelectric cooling element.

14.8.4 Partition Noise

Partition noise is quite similar to the mode hopping noise. In the case of the multilongitudinal mode laser, several modes are excited at the same time. The relative phase and amplitude of the modes are fluctuating, even though the total output power looks steady. The partition noise is a source of FM noise and markedly increases near the threshold current. As the injection current is increased, the number of modes that are excited at the same time decreases, and the partition noise decreases.

The countermeasure is to use a single-longitudinal mode laser, such as will be mentioned in Section 14.9. Some multimode lasers when operated at high injection current have only one dominant longitudinal mode.

14.8.5 Noise Due to Spontaneous Emission

Inherent unwanted spontaneous emission is another source of noise. This noise spreads almost over the entire frequency spectrum. The noise spectrum excited by the spontaneous emission, however, has a peak at the relaxation frequency f_r as shown in Fig. 14.27.

One way to minimize the effect of spontaneous emission noise is to increase the injection current, thereby increasing the ratio of stimulated emission preferentially to the spontaneous emission. The ratio A/B of Einstein's coefficients is proportional to ν^3 and higher frequency lasers are more subject to spontaneous emission noise.

14.8.6 Noise Due to Fluctuations in Temperature and Injection Current

Temperature and current fluctuations are likely to influence any radiating source, but the laser diode even more so. The FM noise is the most significant. Typical values of the frequency shift due to temperature is 12 GHz per degree and that due to the injection current is 2 GHz per mA. It is important to control both of these by using an automatic power control circuit and a thermoelectric feedback loop. In the event that a laser diode is used as the local oscillator of a coherent detection system, there is a good

chance that the IF will walk out of the band of the IF amplifier if the thermoelectric feedback is not provided.

In the following sections, lasers with special features will be presented.

14.9 SINGLE-FREQUENCY LASERS

Some applications require true single-frequency lasers. The laser has to be designed to operate in a single longitudinal mode, and also the waveguide of the laser cavity has to be designed to support only the lowest order lateral as well as transverse mode. This is necessary to ensure a clean, single frequency. Figure 14.28 and Example 14.5 illustrate the spectrum splitting that is observed if higher order lateral modes begin to lase.

Let us assume that both the thickness and the width of the active layer have already been designed to have a single mode in these two directions; our attention will be concentrated only on achieving single-mode operation in the longitudinal direction. Laser diodes that operate in the single longitudinal mode (SLM) include the following:

1. Surface emitting (SE) laser.
2. Distributed feedback (DFB) laser, and distributed Bragg reflector (DBR) laser.
3. Diode laser pumped solid-state laser.

14.9.1 Surface Emitting Laser

If the frequency spacing between adjacent longitudinal modes is wide compared to the frequency bandwidth of the laser gain curve, the laser can be operated in a single longitudinal mode. As seen from Eq. (14.34), the spacing between longitudinal cavity modes is inversely proportional to the length of the cavity. A surface emitting laser

Due to higher order lateral modes

λ
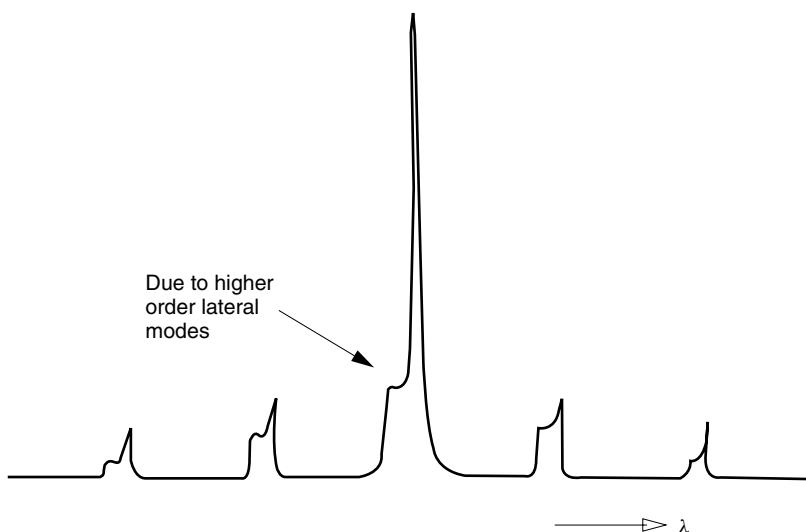
Figure 14.28 Laser spectrum with higher lateral modes.
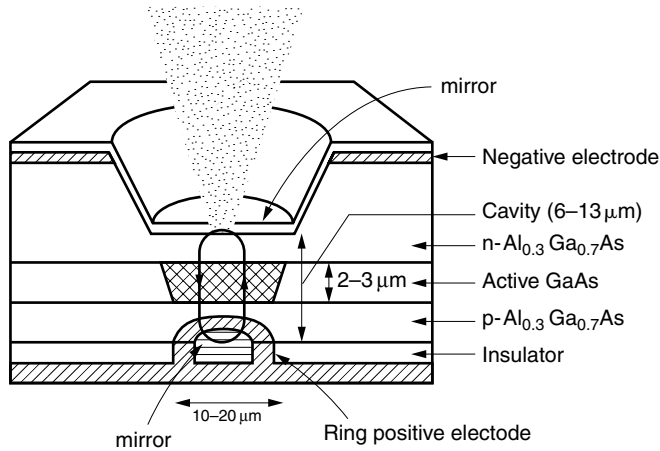
Figure 14.29 Surface emitting (SE) laser. Sometimes this laser is called a vertical cavity surface-emitting laser (VCSEL).

such as shown in Fig. 14.29 has a much shorter cavity length than the edge emitting laser and operates in a single longitudinal mode. The typical cavity length of the SE laser diode is 6–13 μm [20] while that of the normal edge emitting laser diode is 150–250 μm. The wavelength spacing between the longitudinal modes of the SE laser is at least 20 times wider than that of the normal laser diode.

Because the active layer is as short as 2–3 μm, the reflectivity of the mirrors has to be large to meet the threshold condition given by Eq. (14.29). Laser action is obtained by providing high reflectivity mirrors with reflectivities larger than 97%. The SE laser diode is sometimes called a vertical cavity surface-emitting laser (VCSEL).

Other advantages of the VCSEL are the following:

1. Planar technology used to fabricate other electronic or optic components can be used to fabricate the laser as well. Integration of components on a wafer is made easier (monolithic fabrication).
2. Two-dimensional arrays of lasers are possible. These arrays are suitable for the implementation of such devices as optoelectronic interconnects [21].
3. Testing during fabrication is easier.

The disadvantage is the higher threshold current needed to run the laser.

14.9.2 Laser Diodes with Bragg Reflectors

The majority of the end surfaces of the laser cavities so far mentioned have been cleaved facets. The output frequency of the laser diode can be stabilized significantly if the cleaved end facets are replaced by gratings, because the grating selectively reflects a particular wavelength of light while the cleaved surface does not have such selectivity. Figure 14.30 shows a diagram of a distributed Bragg reflection (DBR) [22] laser that employs the sharp frequency dependence of a grating. One or both facets are replaced by corrugated reflectors.
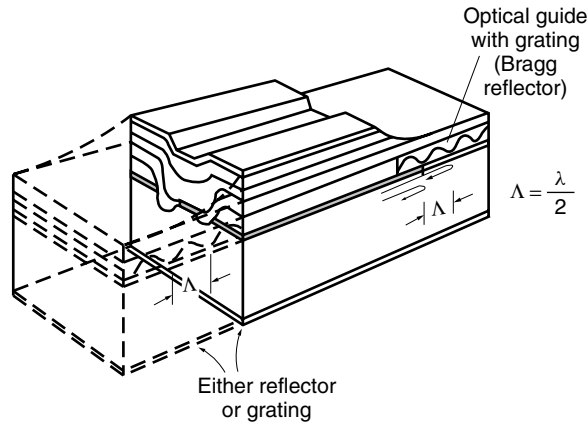
Figure 14.30 Distributed Bragg reflection (DBR) laser.

The corrugated optical guide used as the Bragg reflector does not necessarily have to be located at the end of the cavity. It can be inside the active region or a separate optical guide adjacent to the active layer or the cladding layer. Such a laser is called a distributed feedback (DFB) laser. The DFB laser shown in Fig. 14.31 has the corrugation in a separate guide in order to reduce the loss in the active layer. Both DBR and DFB lasers operate on the same principle.

A heuristic explanation will now be given with a DFB laser whose active region is corrugated along the entire length as shown in Fig. 14.32. Figure 14.32 highlights two possible paths inside the active region. One path is for light that passes straight through the corrugation. The other path is light that is doubly reflected, first at PP' and then at QQ'. For the growth that leads to laser oscillation, it is necessary for all such paths to interfere constructively.

The phase relationship for constructive interference will be found first [23]. Let us assume that the light satisfying the Bragg condition reflects and reverses its direction of propagation when it encounters a peak of the corrugation, but not between the peaks. The reflection centers are discretely spaced by $\lambda/2$. Referring to Fig. 14.32, the
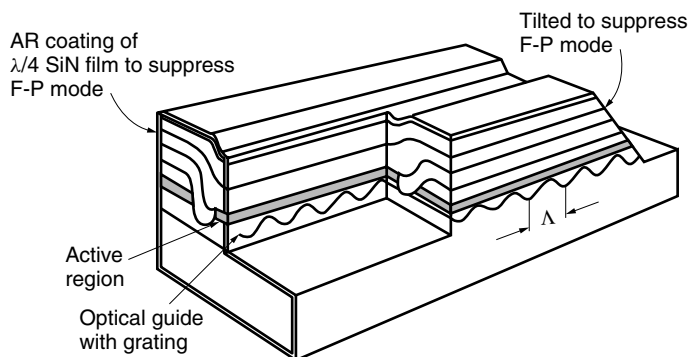
Figure 14.31 Distributed feedback (DFB) laser.
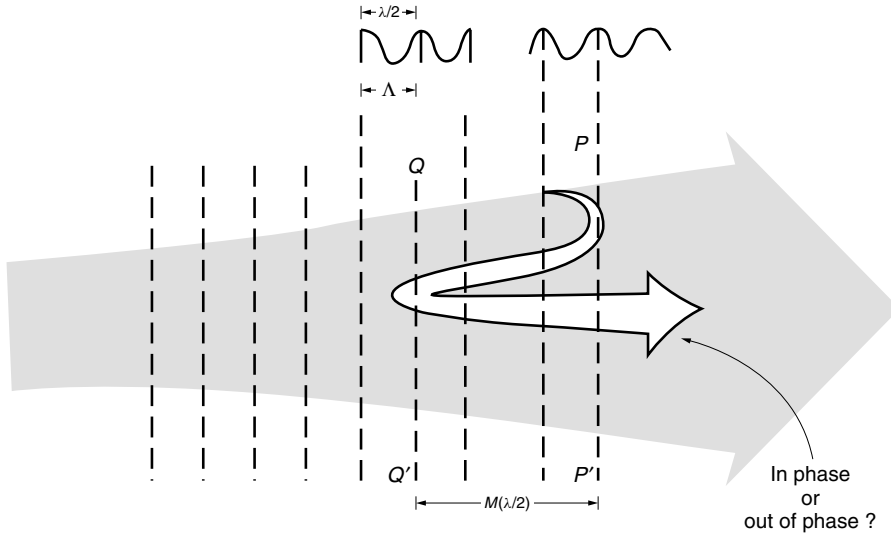
Figure 14.32 Resonance condition of the DFB laser cavity. The difference between the straight-through path and the doubly reflected path is $m\lambda$.

difference between the straight-through path and the doubly reflected path is $m\lambda$, where m is an integer. Does this mean that the lightwaves propagating in the same direction after reflection are always in phase if the frequency satisfies the Bragg condition? The answer is no. The phase shift at each reflection center of the corrugated dielectric grating was left out.

Recall Eq. (5.55) of the increment of the wave joined after each reflection in coupled-mode theory.

$$R(x) = tR_0 + jrS_0 \qquad (14.147)$$

The last term on the right-hand side is interpreted as the contribution of the wave reflected from the discontinuity. Note that this term is an imaginary number and has a phase shift equal to $\pi/2$ radians. The reflection centers QQ' and PP' pictured in Fig. 14.32 each impart a $\pi/2$ phase shift to the reflected light for a total phase shift of π radians with respect to the straight-through path. The doubly reflected light destructively interferes with the straight-through light, and the amplitude does not grow.

We are going to stretch our simple approach further and use basic arithmetic to analyze the situation.

When Bragg's condition is satisfied, the reflections from the corrugated reflectors enhance each other. Bragg's condition that the reflected wave is pointed backward in the axial direction is

$$2\Lambda\beta_0 = 2q\pi \qquad (14.148)$$

where Λ is the period of the corrugation, β_0 is the propagation constant of the active region, and q is an integer. Equation (14.148) can be rewritten in terms of frequency as

$$\nu_{Bq} = \frac{v}{2\Lambda}q \qquad (14.149)$$

The nth cavity resonance frequency including the above-mentioned π-radian phase shift at both ends is obtained as

$$\frac{4\pi}{v} v_{cn} L_e + \pi = 2\pi n \tag{14.150}$$

where L_e is the effective length of the cavity and is represented by a large integer number (~ 1000) M as

$$L_e = M\Lambda \tag{14.151}$$

From Eqs. (14.150) and (14.151), the nth cavity resonance frequency is

$$v_{cn} = \frac{v}{2\Lambda} \frac{1}{M} \left(n - \tfrac{1}{2} \right) \tag{14.152}$$

Figure 14.33 shows the frequencies of the two types of resonances. Visualize two sets of combs of frequency spectra v_{Bq} and v_{cn} whose spacing of spectra (teeth of the comb) are vastly different. The spacing of v_{cn} is about 1000 times more dense than that of v_{Bq}. The optimum lasing frequency is where the two frequencies overlap; that is,

$$v_{cn} = v_{Bq} \tag{14.153}$$

From Eqs. (14.149), (14.152), and (14.153), the ideal integer is

$$n = Mq + \tfrac{1}{2} \tag{14.154}$$
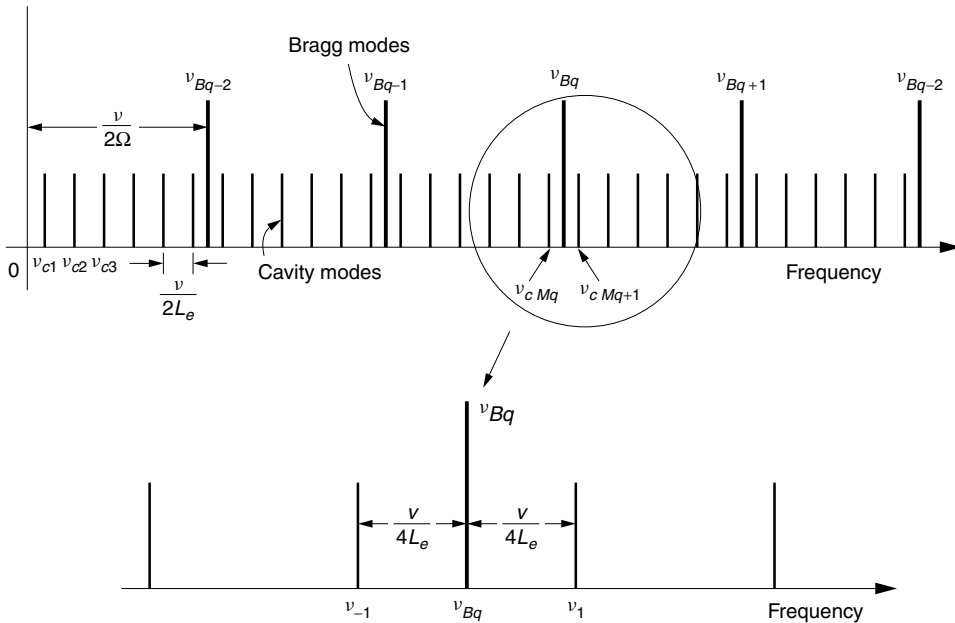
Figure 14.33 Relationship between the Bragg modes and cavity modes of a DFB laser. (After H. Kogelnik and C. V. Shank [23].)

Unfortunately, there is no integer n that can satisfy Eq. (14.154) and the optimum condition does not exist by itself. Let us closely examine the spectrum ν_{cn} near $n = Mq$ using Eqs. (14.149), (14.151), and (14.152). The frequencies ν_{cn} and $\nu_{c(n+1)}$ will be relabeled as ν_{-1} and ν_1, respectively.

$$\nu_{-1} = \nu_{Bq} - \frac{v}{4L_e}$$

$$\nu_1 = \nu_{Bq} + \frac{v}{4L_e} \tag{14.155}$$

The spectrum is shown in the bottom figure of Fig. 14.33. There are two cavity resonance frequencies symmetric with ν_{Bq} but there is no ideal cavity resonance frequency that coincides with the Bragg frequency. It is only after shifting the cavity resonance frequency spectrum to match the Bragg frequency that the optimum operation of the DFB laser can be achieved. Such means are described next.

14.9.3 $\lambda/4$ Shift DFB Lasers

The DFB laser [24] oscillates at two frequencies ν_{-1} and ν_1 as shown in Fig. 14.33 because of the π-radian term on the left-hand side of Eq. (14.150). This may be remedied by adding another π radians to the phase of the doubly reflected wave. The additional π-radian phase shift can be created by introducing a $\pi/2$-radian phase shift in the corrugated grating. Referring once again to Fig. 14.32, imagine that the peak at PP' is shifted over by $\lambda/4$. The distance between PP' and QQ' becomes $(m\lambda/2 + \lambda/4)$, and the total path difference for the doubly reflected path becomes $(m\lambda + \lambda/2)$. In terms of phase, this difference is $2m\pi + \pi$, and thus a π-radian phase shift has been introduced to counteract the π radians from the reflections.

Figure 14.34 illustrates methods of operating the DFB laser on a single longitudinal mode. In Fig. 14.34a, the $\lambda/4$ phase shift was not introduced, and the two frequencies ν_1 and ν_{-1} in Eq. (14.155) are present. In Figs. 14.34b–d, a $\lambda/4$ phase shift was introduced by three different methods. In the first method, the $\lambda/4$ shift is introduced by introducing a $\Lambda/2$ shift in corrugation, noting $\lambda = 2\Lambda$. This shift is achieved by removing one-half period of the corrugation, in other words, by reversing the phase of the grating in the right half of the corrugation. This kind of grating was fabricated by projecting an interference pattern made by He–Cd laser beams (0.4416 μm) into photoresist. The phase reversal of the corrugation is achieved by using a combination of negative and positive photoresists or by inserting a phase shift plate in one side of the corrugated grating. The frequency of the $\lambda/4$ shift DFB laser is exactly on the Bragg frequency, as indicated on the left of Fig. 14.34b.

The $\lambda/4$ phase shift can also be created by etching off some of the height of the corrugation at an empirically determined height Δh and length Δl, as shown in Fig. 14.34c.

The next method shown in Fig. 14.34d uses an external reflector in order to create the required π-radian shift in the cavity. The cleaved facet of the laser cavity is first coated with an SiN film and then a gold film reflector. The thickness of the SiN film is designed to create the phase shift needed for the DFB laser to oscillate at the Bragg frequency.

The last method shown in Fig. 14.34e operates in a slightly different manner [25]. Multielectrodes are deposited on a DBR laser as shown in Fig. 14.35. The left section
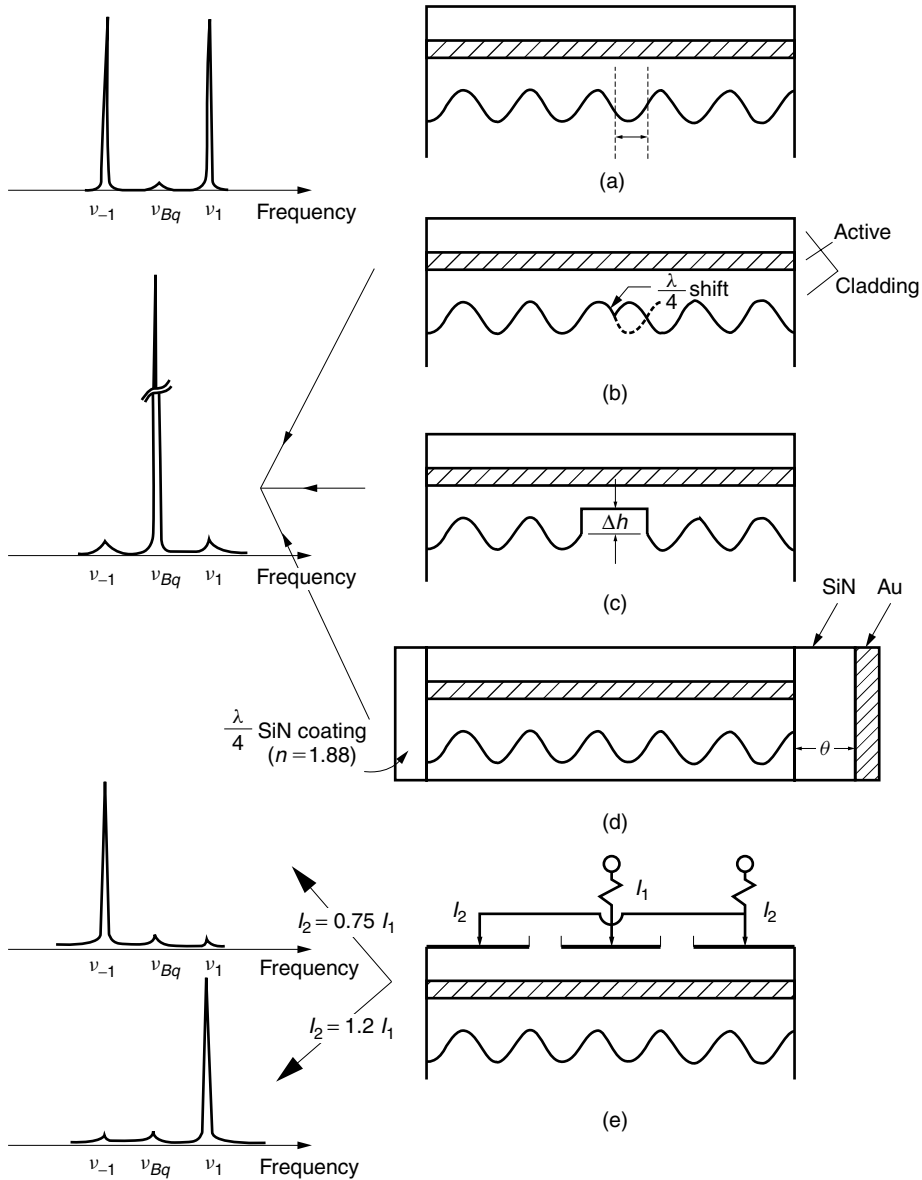
Figure 14.34 Single longitudinal mode (SLM) operation of the DFB lasers. (a) Corrugated grating. (b) $(\Lambda/2 = \lambda/4)$ shift in grating. (c) Phase shift by etching. (d) Phase shift by coating. (e) Phase control by multielectrodes.

plays the role of the active region, the center section plays the role of the phase control region, and the right section acts as a fine tunable Bragg reflector. The tuning resolution is so fine that only one of the two possible modes is differentially favored, so as to oscillate at one frequency. The frequency of the laser can be either ν_{-1} or ν_1 depending on the ratio of the current I_1 of the center electrode and the current I_2 of the right electrode.
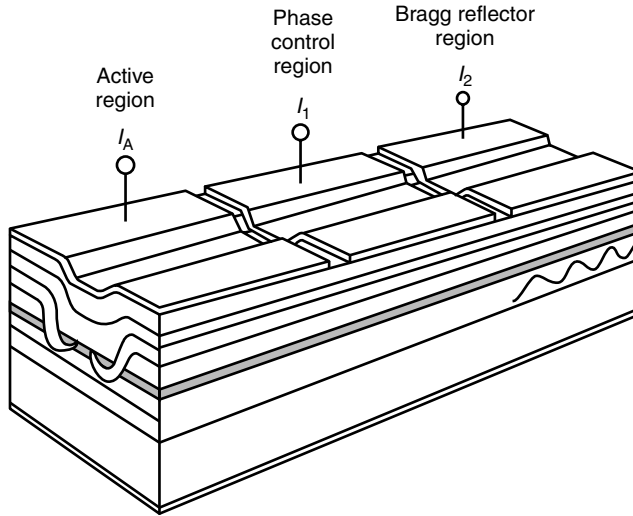
Figure 14.35   Combination of DFB and DBR lasers for wavelength tuning.

An increase in the injection current increases the carrier concentration and that, in turn, decreases the index of refraction because of the plasma effect (see Section 14.4.3.2). The decrease in the index of refraction n increases v and hence increases the Bragg frequency expressed by Eq. (14.149). In short, an increase in the injection current increases the frequency of the Bragg reflection. Thus, an increase in current I_2 shifts the optimum feedback efficiency to a higher frequency and switches the laser frequency to ν_1. Conversely, a decrease in current I_2 switches the frequency to ν_{-1} as indicated in Fig. 14.34e. It should be added that by shifting both I_1 and I_2 in the proper ratios, the position of ν_1 (or ν_{-1}) can be shifted continuously.

Example 14.4   Due to the ease of fabrication, the third-order Bragg frequency is often used. In this case, some light reflects in directions other than the exact backward direction and creates radiation loss as well as stray light. Find the general expression for the direction of radiation from the corrugated grating fabricated in the cladding layer and then find the directions of scattering other than the backward direction.

Solution   With the geometry as shown in Fig. 14.36, let us assume that the sources of radiation are the bottom points of the corrugation because they are the points of the largest interaction with the active region underneath. The propagation constant of the evanescent wave is the same as the propagation constant β_0 of the active region. Referring to point O, the phase at P' is

$$\phi_{P'} = \beta_0 \Lambda \tag{14.156}$$

The phase at P of the wave emanating from point O is

$$\phi_P = n_2 k \Lambda \cos\theta \tag{14.157}$$
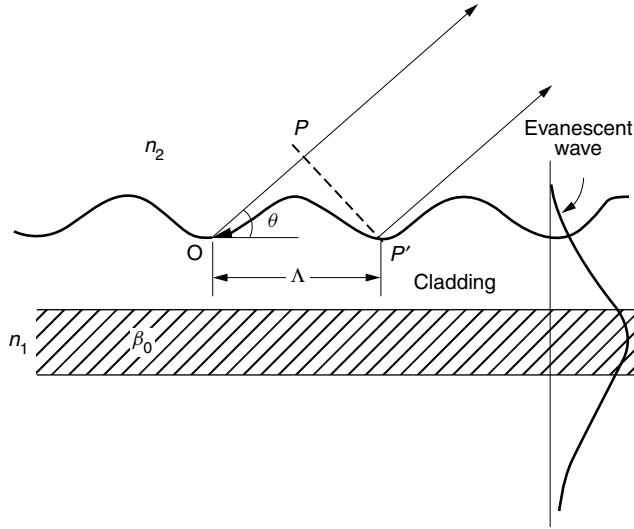
Figure 14.36   Directions of the radiation from the corrugated grating.

where n_2 is the index of refraction of the radiating medium and k is the free-space propagation constant. The angle θ is the angle of radiation. The peaks of the radiation pattern appear in such directions that the waves at P and P' are in phase.

$$\beta_0 \Lambda - n_2 k \Lambda \cos \theta = 2m\pi \tag{14.158}$$

$$\cos \theta = \frac{\beta_0 \Lambda - 2m\pi}{(n_2 k / \beta_0)\beta_0 \Lambda} \tag{14.159}$$

It should be realized that the backscattered wave ($\theta = \pi$) is special in that it propagates exclusively inside the core medium and never goes out of the core and its propagation constant is β_0 rather than $n_2 k$. The value of Λ for this case is obtained from Eq. (14.159), but by replacing $n_2 k$ by β_0 it is obtained directly from Eq. (14.148). The required corrugation period of the qth order Bragg reflection is hence, $\Lambda = 2q\pi/\beta_0$. The directions of radiation other than the backward direction are obtained by inserting this value of Λ into Eq. (14.159) as

$$\cos \theta = \frac{N_0}{n_2}\left(1 - 2\frac{m}{q}\right) \tag{14.160}$$

where $N_0 = \beta_0/k$ is the effective refractive index for the fundamental mode, Eq. (9.44), and is close to n_1. Solutions for the third-order frequency, $q = 3$ with the assumption $N_0 \doteq n_2$, are

θ	m
$0°$	0
$70°$	1
$110°$	2
$180°$	3

Phasefronts drawn to scale are shown in Fig. 14.37. Wavefronts scattered from the adjacent scattering centers are seen in phase.   □
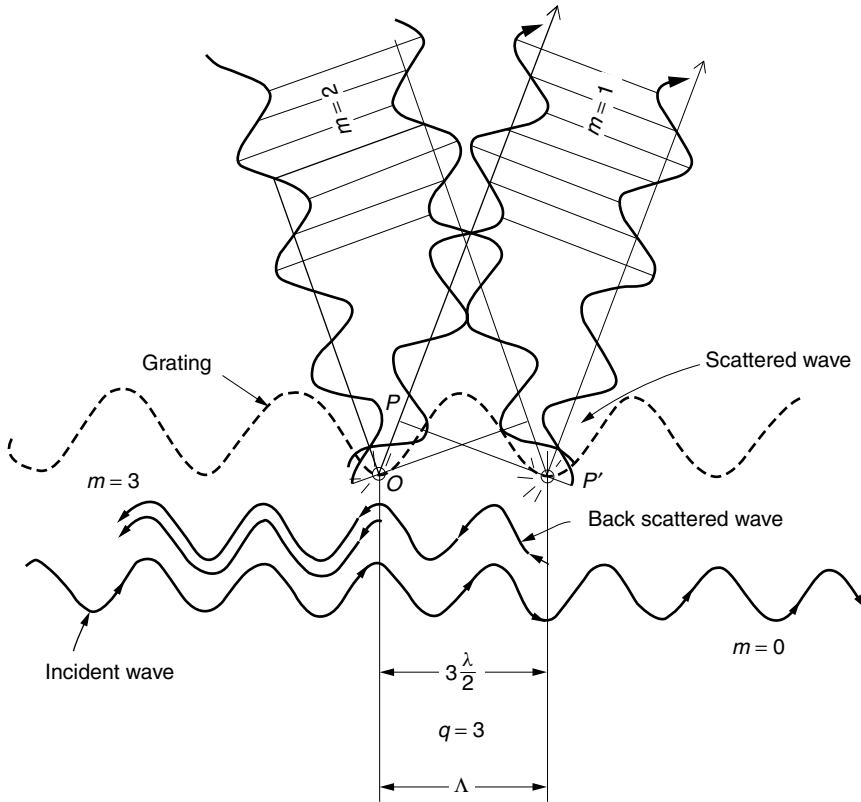
Figure 14.37   Wavefront of the scattered wave from a corrugated grating with $q = 3$, $\Lambda = 3\lambda/2$.

Example 14.5   Taking the example of a metal resonator box, examine the influence of the lateral modes. The resonance mode TM_{nmp} of a metal resonator box is considered. The metal box has the same dimensions as the active layer of the semiconductor laser shown in Fig. 14.38.

Solution   The solution

$$E = A \sin k_x x \cdot \sin k_y y \cdot \sin k_z z \tag{14.161}$$

has to satisfy

$$k_x^2 + k_y^2 + k_z^2 = (n_1 k)^2 \tag{14.162}$$

in order to satisfy the wave equation

$$\nabla^2 E + (n_1 k)^2 E = 0 \tag{14.163}$$
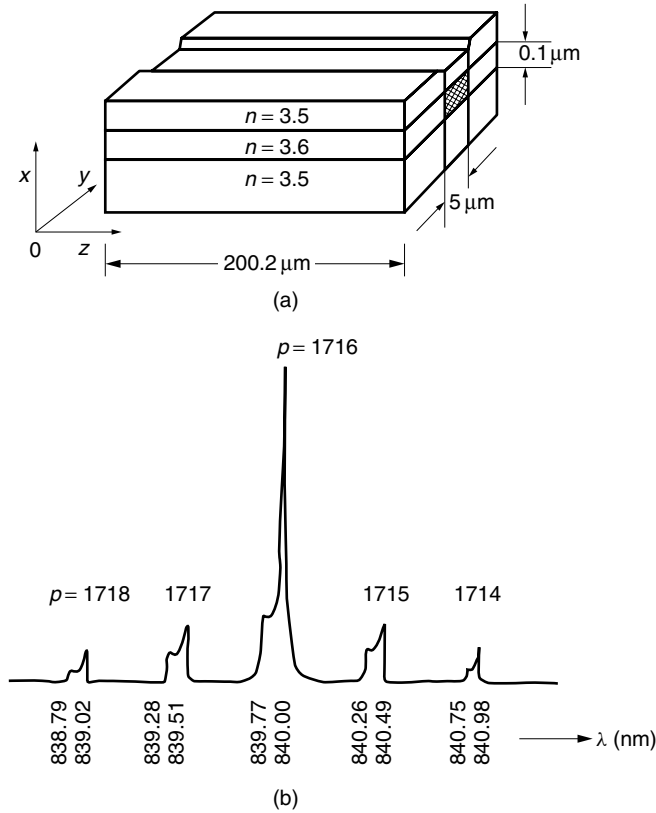
Figure 14.38 Influence of the lateral modes on the resonance wavelength. (a) Dimensions of a laser diode. (b) Spectrum of the modes of a resonator metal box that has the same dimensions as the active layer of the laser diode shown in (a).

k_x, k_y, k_z are determined by the boundary conditions that $E = 0$ on the box walls. Inside the rectangular cavity with dimensions L_x, L_y, L_z,

$$k_x L_x = n\pi$$
$$k_y L_y = m\pi \tag{14.164}$$
$$k_z L_z = p\pi$$

Insertion of Eq. (14.164) into (14.162) gives

$$\left(\frac{n\pi}{L_x}\right)^2 + \left(\frac{m\pi}{L_y}\right)^2 + \left(\frac{p\pi}{L_z}\right)^2 = (n_1 k)^2$$

Hence,

$$\lambda = \frac{2n_1}{\sqrt{\left(\dfrac{n}{L_x}\right)^2 + \left(\dfrac{m}{L_y}\right)^2 + \left(\dfrac{p}{L_z}\right)^2}} \tag{14.165}$$

The value of p can be determined by inserting the given condition $n = m = 0$ and $\lambda_{00p} = 0.84$ μm into Eq. (14.165):

$$p = \frac{2n_1}{\lambda_{00p}}L_z = \frac{2(3.6)(200.2)}{0.84} = 1716$$

Then, wavelength λ_{01p} of TM_{01p} is

$$\lambda_{01p} = \frac{2n_1}{\sqrt{\left(\dfrac{m}{L_y}\right)^2 + \left(\dfrac{p}{L_z}\right)^2}} = \frac{2(3.6)}{\sqrt{\left(\dfrac{1}{5}\right)^2 + \left(\dfrac{1716}{200.2}\right)^2}}$$

$$= 8.3977 \text{ nm}$$

A table of calculated values is given below. Note that λ_{01p} is always shorter than λ_{00p}.

p	λ_{00p} (nm)	λ_{01p} (nm)
1714	840.98	840.75
1715	840.49	840.26
1716	840.00	839.77
1717	839.51	839.28
1718	839.02	838.79

Figure 14.38b shown the spectrum and resembles Fig. 14.28. □

14.9.4   Diode Pumped Solid-State Laser

A neodymium-doped yttrium–aluminum–garnet (Nd:YAG) laser is a laser that can be operated in a single longitudinal mode over a much longer range of cavity lengths than the semiconductor lasers. The neodymium YAG laser is not a *semiconductor* laser but is a *solid-state* laser [1]. Contrary to the semiconductor lasers, the solid-state lasers have discrete energy levels and the frequency bandwidth of the gain curve is about one-thousandth of those of the semiconductor lasers. This makes single longitudinal mode operation easier.

Figure 14.39a shows the geometry and Fig. 14.39b shows the dimensions of a ring resonator type solid-state laser. One immediately realizes that the dimensions of the cavity are about a hundred times bigger than that of a semiconductor laser. Even with these large cavity dimensions, the laser can still maintain single longitudinal mode operation because of the narrow frequency bandwidth of the gain curve of the solid-state laser.

For a 2.5-mm full roundtrip laser cavity, the frequency spacing of the cavity modes $\Delta f = c/2n_1L$ is 33 GHz. The frequency bandwidth of the Nd:YAG gain curve is around 1.2 GHz, and there is no chance that two longitudinal modes are excited simultaneously. With the proper design and alignment of the reflectors, it is fairly easy to suppress the higher transverse modes, so that the Nd:YAG laser can be made to oscillate in a single transverse mode as well as a single longitudinal mode.
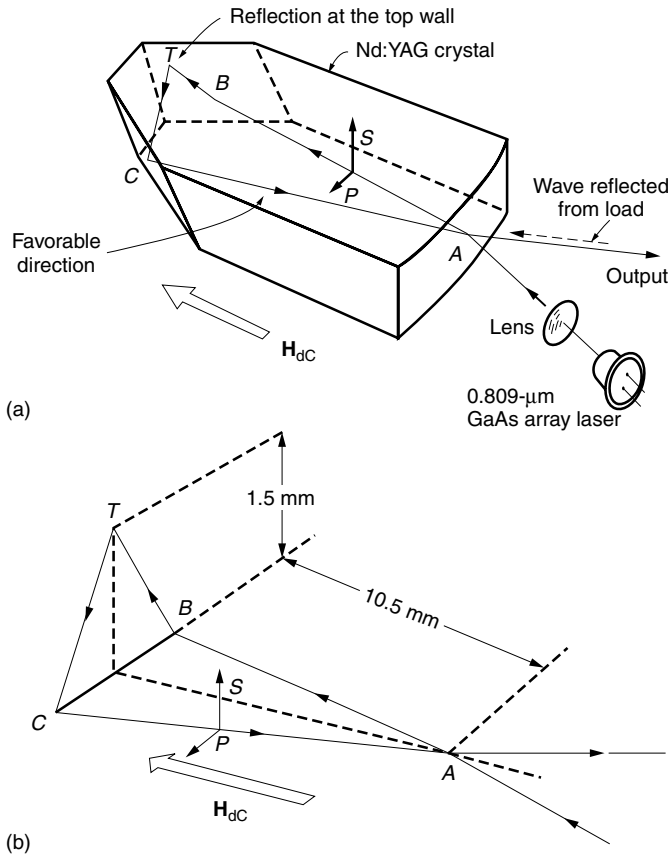
Figure 14.39 Diode pumped solid-state ring laser. (a) Geometry of MISER laser. (b) Light path in the MISER cavity.

The neodymium YAG unidirectional ring laser has such advantages as:

- Single-frequency spectrum.
- Narrow laser linewidth with a short-term (1 ms) frequency bandwidth of 5 kHz and a long-term bandwidth of 100 kHz.
- Immunity to reflections from the load.
- No spatial hole burning in the laser cavity (see Section 14.4).

The disadvantages are:

- Nonplanar structure.
- Difficulty of direct modulation of either frequency or amplitude.
- More complicated structure than semiconductor lasers because the laser has to be optically pumped by a GaAs semiconductor laser of 0.809-μm wavelength of moderately high power.

The monolithic isolated single-mode end-pumped ring (MISER) [26] laser is an example of a laser that took advantage of the large dimensions of the solid-state laser cavity as well as the magnetooptic property of a Nd:YAG crystal.

Next, an explanation will be given on how to accomplish the unidirectional resonance in the MISER laser. As shown in Fig. 14.39b, the full round trip takes the path *ABTCA*, which forms two isoclinal triangles, *ABC* in the horizontal plane and *BTC* in the vertical plane. Total internal reflection is used as mirrors at *B*, *T*, and *C*. Recall that the phase shifts associated with total internal reflection for the $E_\parallel$ and $E_\perp$ components are different as expressed by Eqs. (2.88) and (2.89). In general, the combination of the mirror surface tilt and the differential phase shift between $E_\parallel$ and $E_\perp$ creates an elliptically polarized wave. Let us refer to this effect as a geometrically induced change in the state of polarization. If a magnetic field is applied to the crystal as indicated in Fig. 14.39, the Faraday effect (see Section 5.4.1), which is a magnetooptic effect, will also cause a change in the state of polarization. For one direction of travel around the ring, the Faraday effect acts to subtract the geometrically induced polarization change, while for the other direction of travel, the Faraday effect increases the polarization change. At the output coupler, the reflectivity depends on the state of polarization, and the polarization with the highest reflectivity is favored to oscillate, while the oscillation of the other polarization is suppressed. Lasing occurs in one direction of travel only, and hence the ring resonator is termed unidirectional.

What is the advantage of a unidirectional ring resonator over bidirectional resonators? The answer is higher single-mode power. To understand why, the process of spatial hole burning needs to be explained. When the axial mode begins to lase in a bidirectional-type resonator, a standing-wave pattern is created inside the cavity. The locations of the maxima and the nulls are fixed in space. There is no stimulated emission at the null positions. The spatially modulated gain is referred to as spatial hole burning. In the unidirectional resonator, there is a traveling wave excited in one direction but not the other. There is no standing-wave pattern, and therefore no spatial hole burning. The traveling-wave-type laser cavity permits a larger maximum output light power into a single axial mode than the standing-wave-type cavities.

Any light reflected back into the MISER cavity from the load has to go around the cavity in the unfavorable direction, and the laser operation is far less susceptible to externally reflected waves.

Example 14.6   What is the maximum full-round-trip length in the MISER laser cavity that still maintains the single longitudinal mode operation? Assume the frequency bandwidth of the gain curve is 1.2 GHz and the index of refraction of the Nd:YAG crystal is $n = 1.82$. Also assume that the lasing mode coincides with the center of the gain curve.

Solution   As shown in Fig. 14.40, a frequency spacing of 0.6 GHz will ensure a single longitudinal mode if the cavity mode is at the gain center. Hence, from Eq. (14.36),

$$L \le \frac{c}{2\Delta f n} = 13.7 \text{ cm} \tag{14.166}$$

This L is substantially longer than the $6 - 13$-μm cavity length required by the surface-emitting semiconductor lasers described in Section 14.9.1 for single longitudinal mode operation.   □

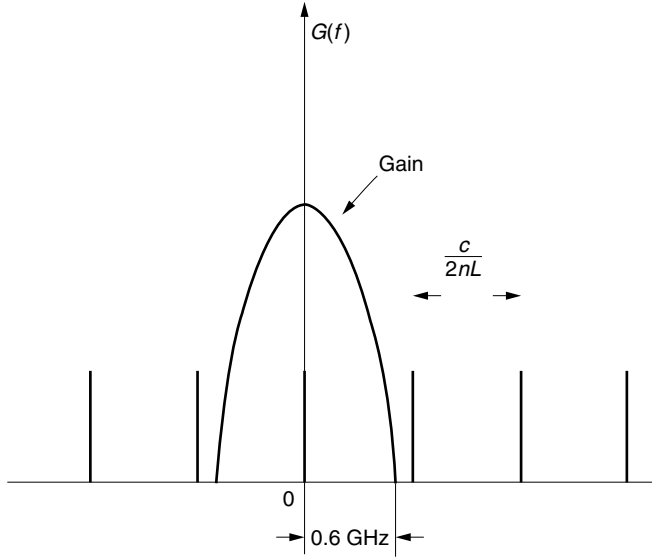**Figure 14.40** Design of the cavity for a Nd:YAG MISER laser.

14.10 WAVELENGTH TUNABLE LASER DIODE

Wavelength tunable lasers are needed as devices for wavelength division multiplexing and as local oscillator lasers for coherent detection. A description of the general principle of wavelength tuning of the DFB laser is given first, followed by that of the superstructure grating (SSG) laser.

14.10.1 Principle of Frequency Tuning of the DFB Laser

With regard to the structure of the DFB laser shown in Fig. 14.41, the lasing conditions will be found [27,28]. The ratio of the fields before and after one trip is

$$rRe^{-j\phi_1 - j\phi_2 - 2(\alpha - g)L} \tag{14.167}$$

where r is the reflection coefficient of the Bragg reflector and R is that of the end mirror, ϕ_1 is the phase shift taking place in the Bragg reflector, and ϕ_2 is the phase delay during one round-trip travel. Let

$$\phi = \phi_1 + \phi_2 \tag{14.168}$$

$$A = rRe^{-2(\alpha - g)L} \tag{14.169}$$

The threshold condition that the wave is enhanced after each trip is

$$Ae^{j\phi} = 1 \tag{14.170}$$

Equation (14.170) reduces to

$$A = 1 \tag{14.171}$$

$$\phi = 2m\pi \tag{14.172}$$

Figure 14.41   Structure of the DFB laser.

Equation (14.171) is the threshold condition that after each round trip the amplitude starts to grow. Equation (14.172) is the condition that after each round trip constructive interference takes place.
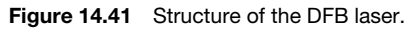
The values of r and ϕ_1 of the Bragg reflector are obtained from coupled mode theory [29]:

$$r = \frac{-jK \sinh \gamma L}{\cosh \gamma L + (d_i + j\Delta\beta) \sinh \gamma L} \tag{14.173}$$

where

$$\gamma^2 = K^2 + (d_i + j\Delta\beta)^2 \tag{14.174}$$

$$\Delta\beta = \beta - \beta_0 = \frac{2\pi}{\lambda}n_b - \pi/\Lambda \tag{14.175}$$

and where Λ is the period of the corrugation of the grating, K is the coupling coefficient of the corrugation of the grating, d_i is the loss constant of the material from which the Bragg reflector is made, and n_b is the equivalent refractive index of the Bragg reflector.

Next, the shift of the lasing wavelength due to the injection of the tuning current will be explained graphically. First, the lasing conditions, Eqs. (14.168) and (14.172), are rewritten as

$$Y_1 = -\phi_1$$
$$Y_2 = \phi_2 - 2m\pi \tag{14.176}$$

and the lasing condition is

$$Y_1 = Y_2 \tag{14.177}$$

Figure 14.42 shows a typical graph of the Bragg reflector loss and phase shift as a function of wavelength. The upper curve shows a quantity related to the mirror loss, that is, the light that does not reflect back from the Bragg reflector. The phase shift Y_1 due to the reflection by the Bragg reflector is shown by the lower curve.

Figure 14.43 shows the plot of ϕ_2 that consists of the phase shift during the round trip and

$$\phi_2 = \frac{2\pi}{\lambda}(n_p l_p + n_a l_a) \tag{14.178}$$

where n_p and n_a are the refractive indices of the phase controller and the active region, respectively, and l_p and l_a are their lengths.

The phase ϕ_2 decreases almost linearly with λ for a small range of λ. The condition of Eq. (14.172) repeats every 2π radians. Y_2 (solid lines) represents the phase ϕ_2 in the region of 0 to 2π radians and Y_2 is obtained from ϕ_2 by subtracting $2m\pi$, where m is an integer called the *longitudinal mode number* of the laser. The shift of ϕ_2 when n_p and n_a are decreased by increasing the tuning current is shown by the dotted lines. The curve of Y_2 shifts toward a shorter wavelength.
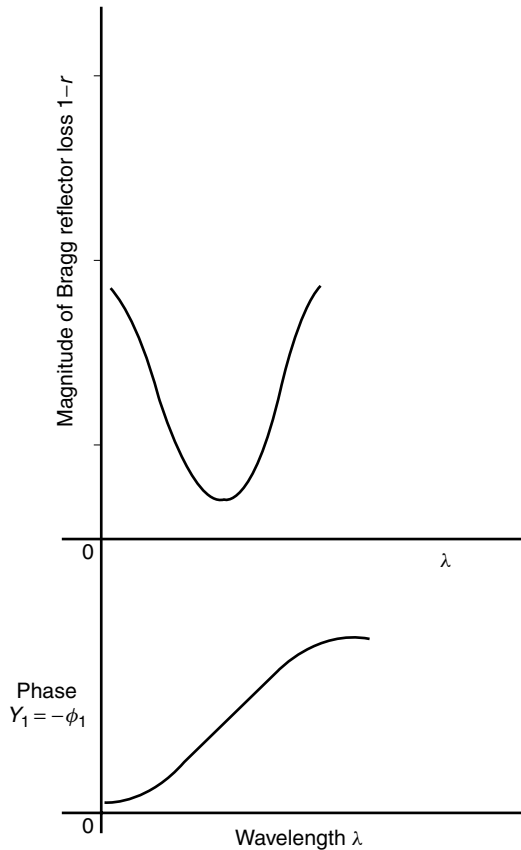
Figure 14.42   Characteristics of the Bragg reflector with respect to wavelength.
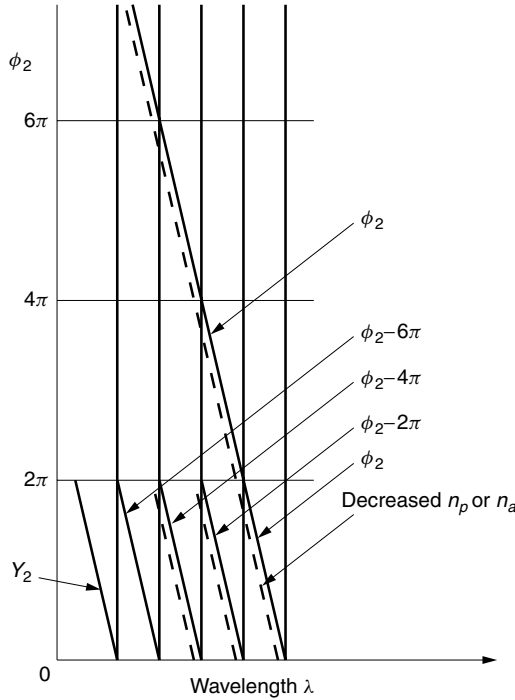
Figure 14.43 Phase delay ϕ_2 associated with one round trip, which continually increases with $1/\lambda$. The phase of the mth longitudinal mode is represented by $Y_2 = \phi_2 - 2\pi m$.

14.10.1.1 Tuning of Wavelength by the Phase Controller Tuning Current I_p Alone

Referring to the solid lines in Fig. 14.44, $Y_1 = Y_2$ is satisfied at four intersections 1, 2, 3, and 4 in the phase diagram. The corresponding mirror losses are indicated by circles in the upper curve.

The threshold point is determined by the smallest mirror loss. Among the four wavelengths, the mirror loss is the smallest at point 2 and lasing starts at this wavelength.

As I_p is increased, the Y_2 curves start to shift toward the left and the intersections move to 1′, 2′, 3′, and 4′. For instance, the operating point 2 shifts to 2′.

As I_p is increased, point 2 climbs to a higher point 2′ on the mirror loss in the upper curve while point 3 slides down to a new point 3′. As soon as 3′ comes to a point lower than point 2′, the operation point hops to 3′, a longer wavelength. This is the phenomenon of mode hopping. The operating point will keep shifting to point 3″ as I_p is further increased. The wavelength becomes shorter until the next hopping occurs, at which time the wavelength hops to a longer wavelength. The process repeats and the maximum tuning range is limited to between 2′ and 3′, as indicated in Fig. 14.45. This is the case when only the phase controller tuning current I_p is varied.

14.10.1.2 Tuning of Wavelength by the Bragg Reflector Tuning Current I_b Alone

As the Bragg reflector tuning current I_b is increased, both the phase and the Bragg reflector loss shift toward a shorter wavelength, as shown in Fig. 14.46.
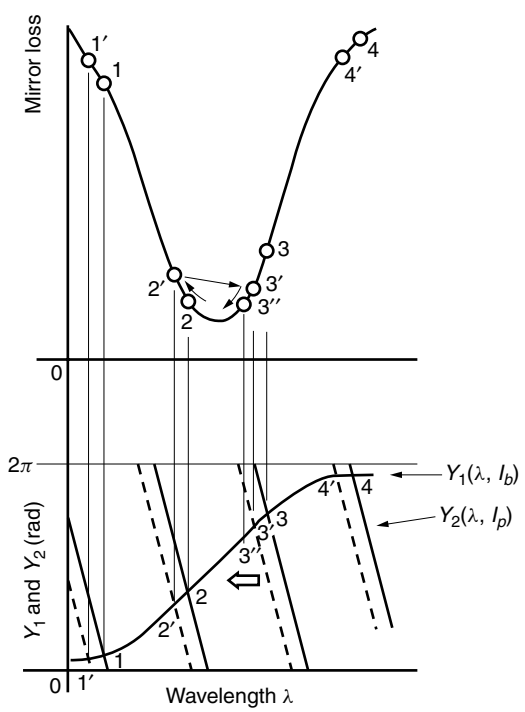
Figure 14.44 Shift of the lasing condition due to the injection of the phase control current. (After K. Kobayashi and I. Mito [27].)
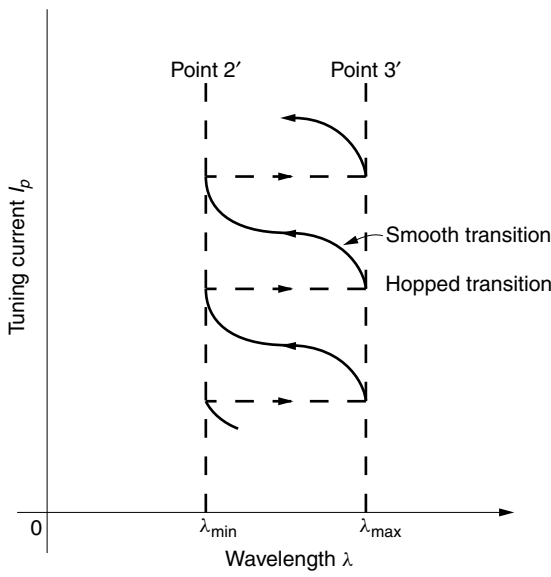
Figure 14.45 Range of wavelength tuning by I_p alone. The path of the operating point repeats and the tuning range is limited. (After K. Kobayashi and I. Mito [27].)
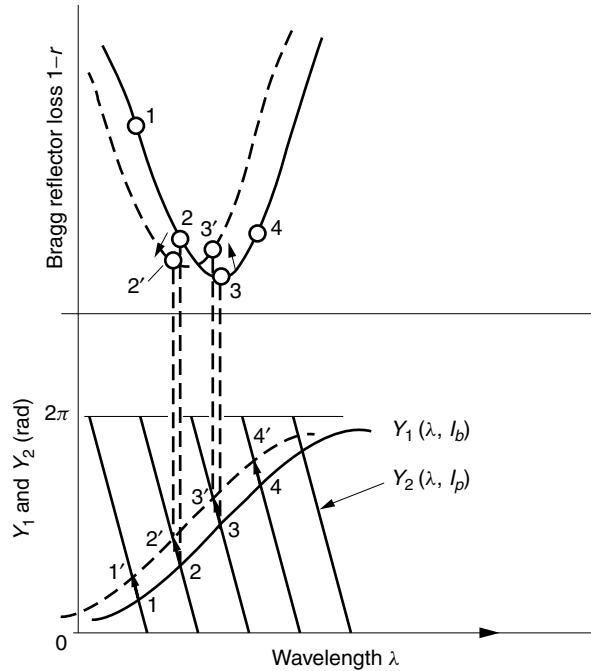
Figure 14.46 Shift of operating point with hopping as I_b is increased. (After K. Kobayashi and I. Mito [27].)

There are four intersections 1, 2, 3, and 4. Among the four intersections, 3 has the lowest Bragg reflector loss and the lasing takes place at 3 when I_b is zero.

As the tuning current I_b is increased, these intersections 1, 2, 3, and 4 move to the upper left to 1′, 2′, 3′ and 4′, as indicated in the bottom of Fig. 14.46, and the wavelength of operation becomes shorter. The corresponding points of the Bragg reflector loss are indicated by the numbers in the top graph.

Among the satisfied phase conditions, it is always with the lowest Bragg reflector loss that lasing takes place. With the top graph of Fig. 14.46, the operating point is at 3 when I_b is zero, but as I_b is increased, the Bragg reflector loss moves up to a new point 3′. At the same time, operating point 2 moves downward to 2′. As soon as 2′ becomes lower than 3, the wavelength of operation hops from point 3 to 2′ and there are no in-between operating points. If I_b is further increased, the operating point will hop to 1′.

Thus, the wavelength of operation decreases with increasing I_b but with a series of wavelength hopping as shown in Fig. 14.47, and no continuous tuning is achievable.

14.10.1.3 Continuous Wavelength Tuning by Combining I_p and I_b

By combining the phase controller and Bragg reflector tuning currents alternately, continuous wavelength tuning is possible. The phase controller Y_2 is shifted first, and then the Bragg reflector phase Y_1 is shifted to follow the shift of the Y_2.

Figure 14.48 explains this mode of operation. Let's start from the operating point 1. First, Y_2 is moved to the left by injecting I_p and the operating point moves toward point 2. Then Y_1 is moved toward the left by injecting I_b and the operating point
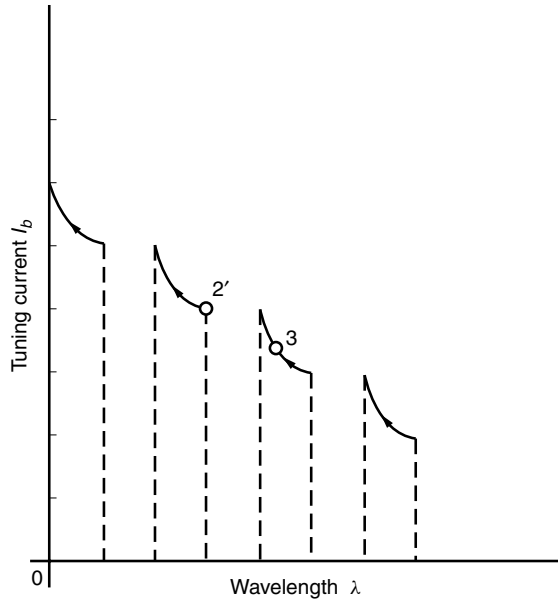
Figure 14.47   Decrease in wavelength of operation when I_b alone was increased. Note existence of hopping. (After K. Kobayashi and I. Mito [27].)
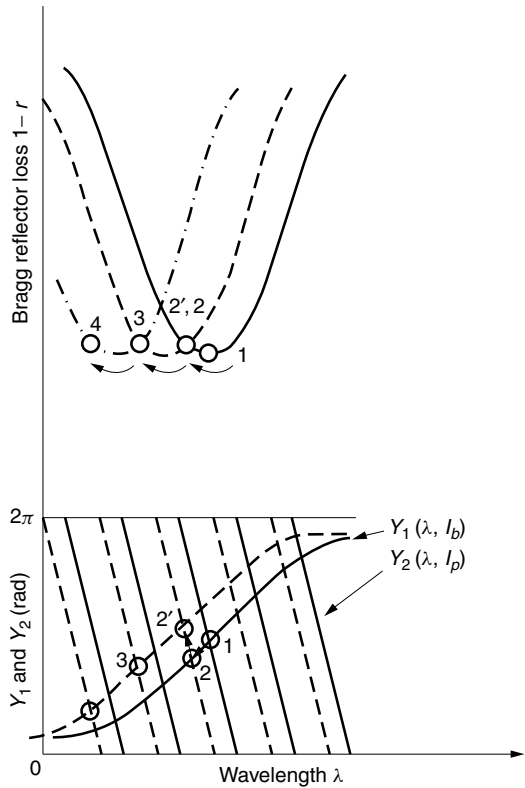
Figure 14.48   Continuously tunable laser diode. (After K. Kobayashi and I. Mito [27].)

moves by a small amount to point $2'$. Next, I_p is increased and the operating point is moved further to the left to point 3. Thus, by alternately changing I_p and I_b, the operating wavelength can be shifted continuously as shown in Fig. 14.49.

The tunable range of a tunable DFB laser, however, is at most 1% of the center wavelength because it is limited by the amount of change Δn in the refractive index of the Bragg reflector. The maximum amount of change Δn in the refractive index by the plasma effect of the injection current is around 1%. The operation of the SSG laser diode, which has a much wider range than the tunable DFB laser, will be presented in the next section.

14.10.2 Superstructure Grating Laser Diode (SSG-LD)

The SSG-LD [30,31] made it possible to expand the tuning range by a factor of 10 over the tunable DFB lasers using the vernier effect between the reflection peaks of two superstructure gratings whose reflection peaks are spaced slightly differently.

The distribution of the refraction index of the superstructure grating is shown in Fig. 14.50a. It is a superstructure in the sense that substructures are repeated to form an overall structure. The substructures are repeated with a period of Λ_s. Each substructure is a grating and the period is chirped so that the reflectivity is uniform for a wide band of frequencies. The reflection center for a lower frequency is at the leftmost of each substructure $a_1, a_2, a_3, \ldots, a_n$ and that of a higher frequency is at the rightmost of each substructure $b_1, b_2, b_3, \ldots, b_n$. It should be noted that the spacing $a_{n-1} - a_n$ for the lower frequency and $b_{n-1} - b_n$ for the higher frequency
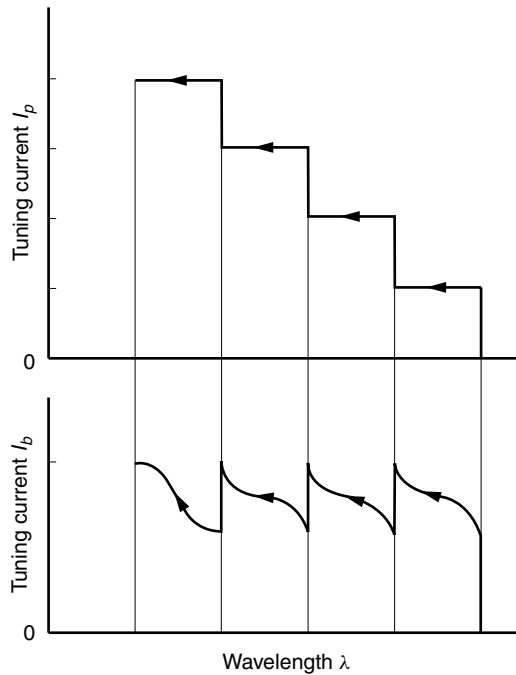
Figure 14.49 Tuning currents of I_p and I_b for continuous tuning operation. (After K. Kobayashi and I. Mito [27].)
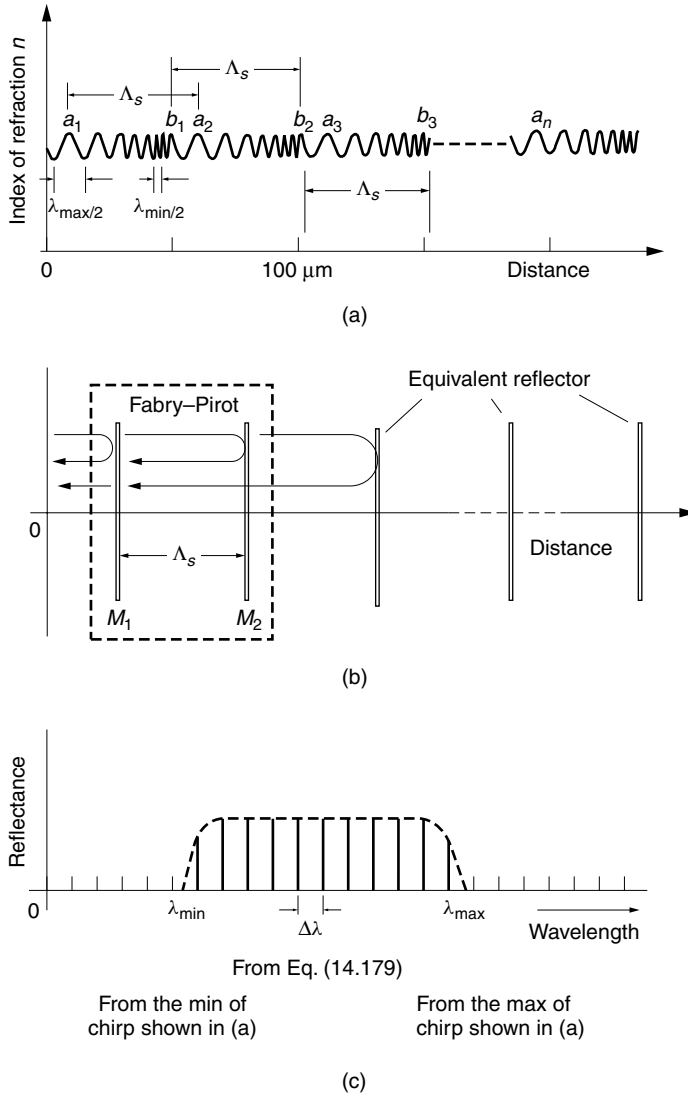
Figure 14.50 Superstructure grating laser diode. (a) Refractive index distribution of the superstructure grating. (b) Equivalence of superstructure grating to a Fabry–Pérot resonator. (c) Spectrum of reflection peaks of the superstructure grating. (After Y. Tohmori et al. [30].)

are both Λ_s. Thus, the superstructure grating can approximately be regarded as an array of nonfrequency-dependent scattering centers spaced at Λ_s, as shown in Fig. 14.50b. The reflection from such an array structure can be regarded as multiple reflections taking place in a Fabry–Pérot resonator with its reflector spacing Λ_s (see Section 3.1.1). The reflection characteristic from the superstructure is similar to that of the Fabry–Pérot resonator. The spacing $\Delta\lambda$ of the reflection peaks of such a Fabry–Pérot resonator is

$$\Delta\lambda = \frac{\lambda^2}{2n\Lambda_s} \tag{14.179}$$

where n is the refractive index of the grating region. The injection current can change the value of the refractive index, and thus the spacing $\Delta\lambda$ of the reflection peaks is controlled by the injection current. Figure 14.50c shows the pattern of the reflection peaks with respect to the wavelength. The configuration of the substructure determines the shape of the envelope of the reflection peaks (see Section 1.4.9). The minimum light wavelength is determined by $\lambda_{min}/2$, which is the shortest period of the chirp structure shown in Fig. 14.50a, and the maximum wavelength λ_{max} is determined by $\lambda_{max}/2$, which is the longest period of the chirp structure.

Next, the vernier effect will be explained. The SSG laser diode (SSG-LD) has two superstructure gratings at the front and rear ends of the diode as shown in the cutout view of the SSG-LD in Fig. 14.51. These two superstructure gratings are similar except for their period Λ_s. One of them is slightly shorter than the other. Let us say for now the period Λ_s of the front grating is slightly shorter, and hence the period $\Delta\lambda$ given by Eq. (14.179) is slightly wider than that of the rear grating. Figure 14.52 shows the reflection patterns back to back.

In order to build up the amplitude, the lightwave has to pass not just once but repeatedly through the active region. When the wavelength of the reflection peaks of the front and rear superstructure gratings coincide, the light of this wavelength is reflected at both ends. Repeated passage of the lightwave through the active region becomes possible, and lasing takes place. For instance, Fig. 14.52 shows the configuration of three wavelengths at λ_n, λ_n', and λ_n''. These are three possible matches but λ_n' and λ_n'' are outside the envelope of the reflection peaks, and their reflectivities are too small to lase. The shape of the envelope has to be designed so that λ_n' and λ_n'' are outside the envelope. As mentioned earlier, the shape of the envelope is manipulated by the shape of the chirp in the substructure shown in Fig. 14.50a.
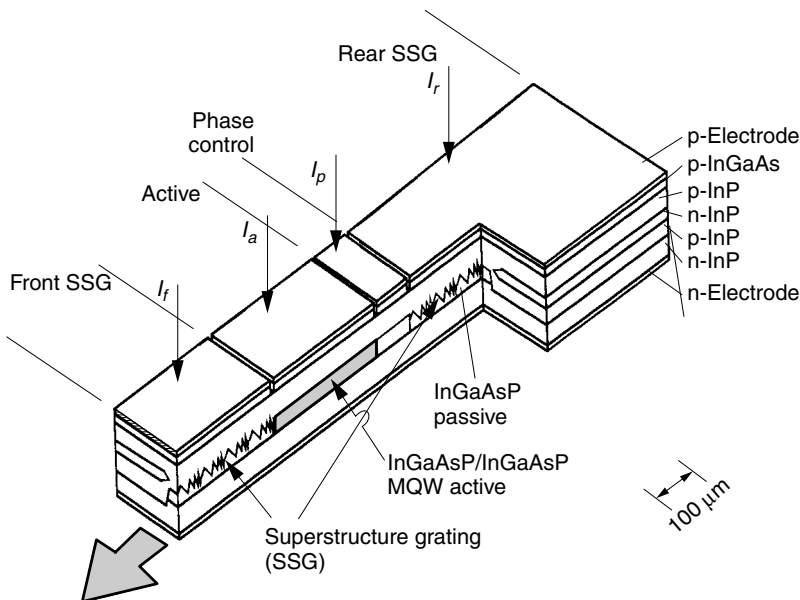

Figure 14.51 Schematic drawing of the multiple phase shift SSG-DBR laser. (After Y. Tohmori et al. [30].)
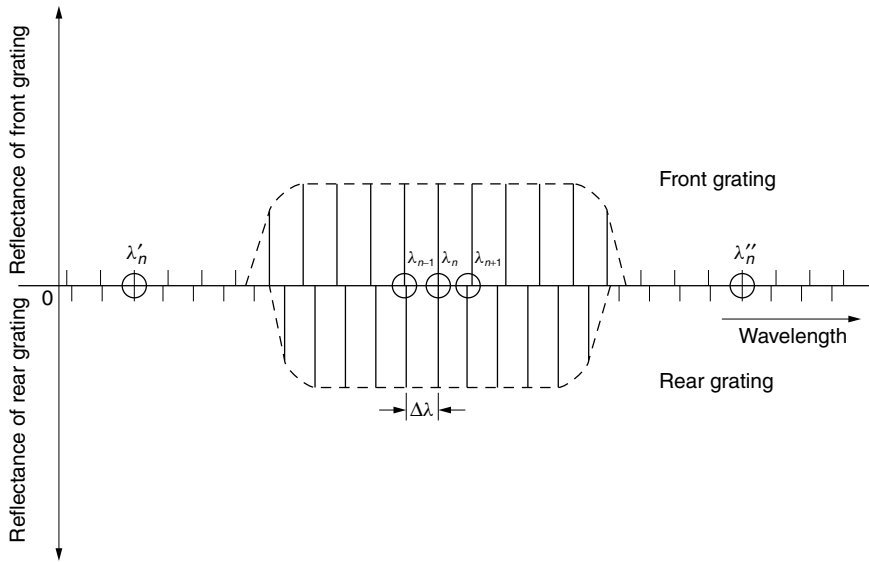
Figure 14.52   Principle of stepping the wavelength of the SSG-LD.

Next, the manner of the wavelength tuning will be explained. If an electric current is injected into the grating regions, the refractive index n is decreased, the spacing $\Delta\lambda$ of the reflection peaks expands, and each peak shifts toward a longer wavelength (toward the right). Now, if the tuning current is applied only to the rear grating, the lower spectrum in Fig. 14.52 shifts to the right while the upper spectrum is unchanged, and the lasing wavelength will shift to λ_{n+1}, where the two reflection peaks will meet. On the other hand, when the tuning current is applied only to the front grating, the lasing wavelength will hop to λ_{n-1}. If both tuning currents are applied, a finer tuning of the wavelength of oscillation is possible.

Only a small amount of shift of the reflection peaks shown in the circles in Fig. 14.52 can create a substantial wavelength shift. This resembles the action of the vernier scale where with a slight movement of the vernier scale, the position of the matched graduation of the regular and vernier scale moves over a large number of graduations.

In addition to the front and rear grating, the laser is equipped with a phase control region. This region is used for adjusting the phase so that the phase of the wave after one round trip matches that of the previous round trip to ensure that the wave constructively adds up after each round trip and the amplitude builds up.

Figure 14.53 shows how the lasing wavelength shifts by manipulating the phase control currents. The horizontal axis is the wavelength and the vertical axis is the light output with representative combinations of control currents. The wavelength of the output light shifts over 50 nm by various choices of front, rear, and phase tuning currents.
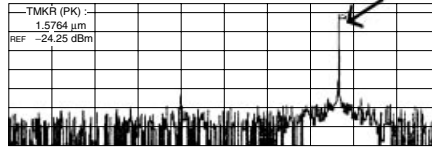
14.11   LASER DIODE ARRAY

Laser diode arrays are employed in situations where a multiplicity of independent sources are required, such as in driving a multifiber cable. In this case, the laser diodes
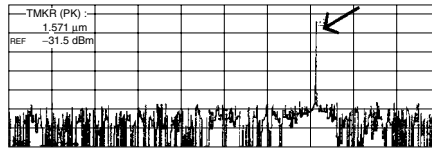
Region 1
1.581 μm, I_{th} = 5 mA
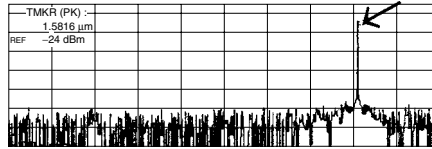
Region 2
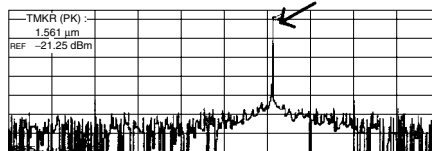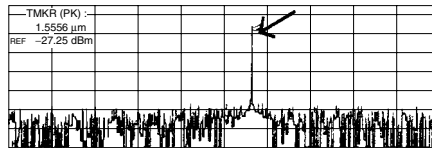1.576 μm, I_{th} = 5 mA

Region 3
1.570 μm, I_{th} = 7 mA

Region 4
1.560 μm, I_{th} = 5 mA

Region 5
1.555 μm, I_{th} = 7.5 mA

Region 6
1.541 μm, I_{th} = 7.5 mA
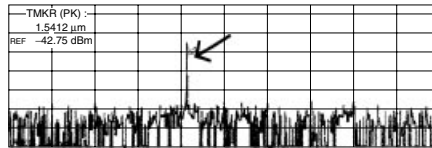
Region 7
1.531 μm, I_{th} = 9.5 mA
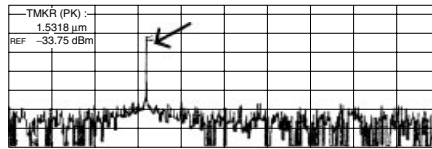
10 dB/div

Figure 14.53 Lasing spectra of seven wavelength regions in a 50-nm tuning range. (After Y. Tohmori et al. [30].)

are connected in one-to-one correspondence, that is, one light source to one optical fiber in the cable. The surface-emitting laser diode array belongs to this category. The individual lasers are optically isolated.

Figure 14.54 shows a vertical cavity surface-emitting laser (VCSEL) array [32] used for a free-space optical interconnection. The array not only connects optical channels at an ultrafast switching speed but also overcomes the intrinsic limits of physical wiring [33]. Figure 14.54a is a schematic of a basic VCSEL array. Figure 14.54b
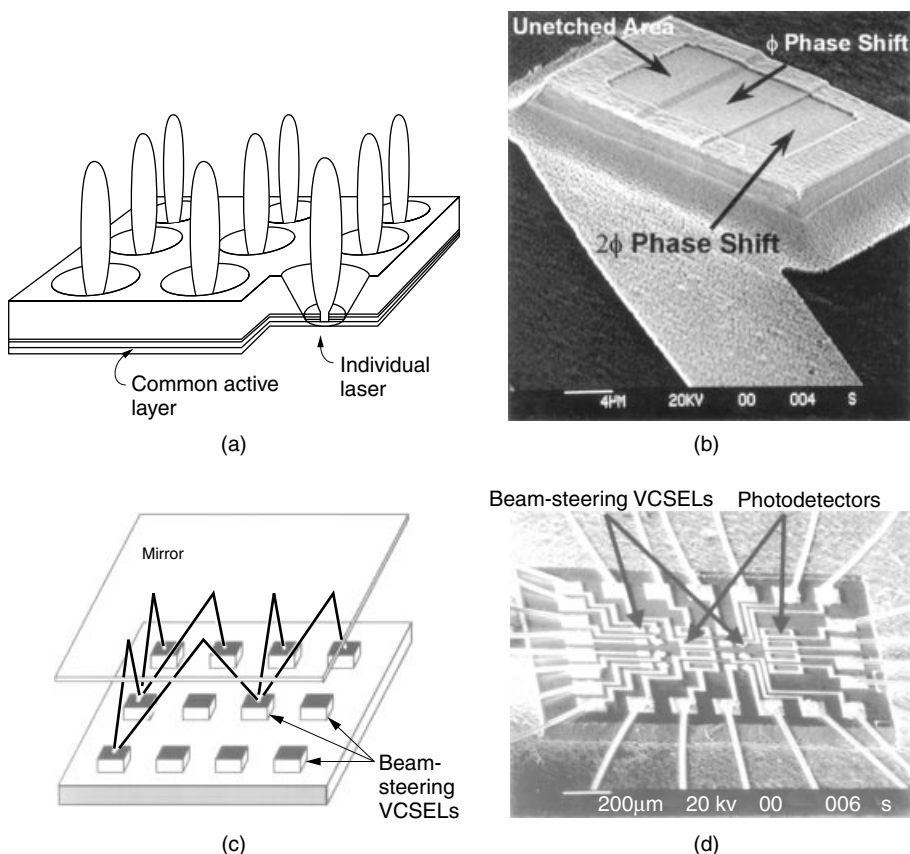
Figure 14.54 Vertical cavity surface-emitting laser (VCSEL) diode array. (a) VCSEL array. (b) SEM photograph of VCSEL array with beam-steering router. (c) Schematic diagram of the VCSEL array optical interconnect. (d) SEM photograph of a packaged 4 × 4 photonic network. (After L. Fan et al. [32].)

shows a beam-steering VCSEL. A three-element phase shifter film is deposited on the outer surface of the VCSEL and the direction of the light beam is electronically steered. (The principle is explained in Fig. 14.24.) Such beam-steering VCSELs are used for implementing multistage space division switching networks, as illustrated in Fig. 14.54c. Figure 14.54d is a scanning electron microscope photograph of a packaged 4 × 4 optical interconnect.

An alternate use of laser diode arrays is in a many-to-one correspondence, whereby many laser diode sources are fed into a single fiber or single optical component. This arrangement is used to increase the light power into the optical component. In order to effectively increase the total output from the array, the element lasers have to be excited coherently with each other. The rest of this section will be devoted to this category of coherent laser diode arrays.

Normally, the elements of the coherent laser array are put close together. If all array elements have the same amplitude and phase and are closely spaced, the outputs of the array elements approximate the distribution shown in Fig. 14.24b, and a narrow symmetric, high intensity beam can be obtained. It is important that all the array

elements have the same phase. If for instance, the left half of the array elements are in opposite phase to the right half of the elements, they form an antisymmetric distribution, and a null appears in the middle of the radiation pattern as shown in Fig. 14.24d. The outputs of the array elements should discretely approximate either the pattern in Fig. 14.24b or c.

Figure 14.55 shows a Y-branch laser diode array [34] that forces the output from each array element to be identical with the adjacent elements. The geometry of the Y-branch laser array is shown in Fig. 14.55a. For the purpose of illustrating the principle of operation of the array, only one period of the array is shown separately in Fig. 14.55b. Let us assume first that the amplitude E_1 of the bottom left arm is different from E_3 of the bottom right arm. Amplitudes are arbitrary, but phases are assumed either in phase or 180° out of phase. The general case is left for Problem 14.4. E_1 and E_3 can be decomposed into a symmetric (in-phase) component E_s, and an antisymmetric (180° out-of-phase) component E_a, as shown in Fig. 14.55b. The E_s components in both arms of the same amplitude oscillate in phase, whereas the E_a components in both arms of the same amplitude oscillate 180° out of phase. Using the law of superposition, E_1 and E_3 are expressed in terms of symmetric and antisymmetric components as

$$E_1 = E_s + E_a$$
$$E_2 = E_s - E_a$$

(14.180)

Then, E_s and E_a are

$$E_s = \frac{E_1 + E_2}{2}$$
$$E_a = \frac{E_1 - E_2}{2}$$

(14.181)

Now consider the inputs into the upper arms. The E_s components add constructively and the input to the upper arms is $2E_s$ whereas the E_a components add destructively and the input to the upper arm is zero, as indicated in Fig. 14.55b. Picture Fig. 14.55b with laser cavity mirrors located at the top of branch E_2 and at the very bottom of branches E_1 and E_3. The input into the upper arm is amplified and then reflected downward into the lower arms, and, depending on the reflectivity of the mirrors, this up-and-down pattern may be repeated several times before the light radiates out from either the top
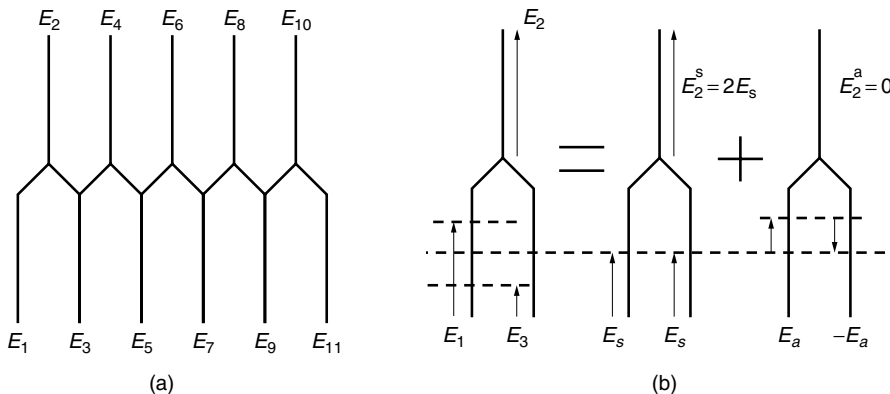

Figure 14.55 Y-branch laser array. (a) Branch laser array. (b) Explanation of the operation.

or bottom apertures. The symmetric components $2E_s$ are much more amplified than the antisymmetric components whose input to the upper arm is null. This is true with all neighboring arms in the Y-branch array shown in Fig. 14.55a. Thus, $E_2, E_4, \ldots, E_{2n}$ are excited in phase, and so are $E_1, E_3, E_5, \ldots, E_{2n-1}$. The aperture pattern of the array discretely resembles that in Fig. 14.24b if the spacing between the elements is small. Such a laser array emits a narrow high-intensity beam.

14.12   MULTI-QUANTUM-WELL LASERS

By alternately stacking thin layers of wider and narrower bandgaps as shown in Fig. 14.56a, a series of potential wells such as shown in Fig. 14.56b is formed that is called a *multi-quantum well* (MQW) [35]. As the dimensions of the potential wells are reduced to the order of 10 nm, the movement of the electrons is restricted inside the potential well, and quantum effects become prominent.

The laser gain curves made up of Eqs. (14.2), (14.5), and (14.19) are strongly governed by the shapes of the density of the states $g_c(E_2)$ and $g_v(E_1)$. The quantum well effect makes it possible to tailor the shapes of the functions of $g_c(E_2)$ and $g_v(E_1)$
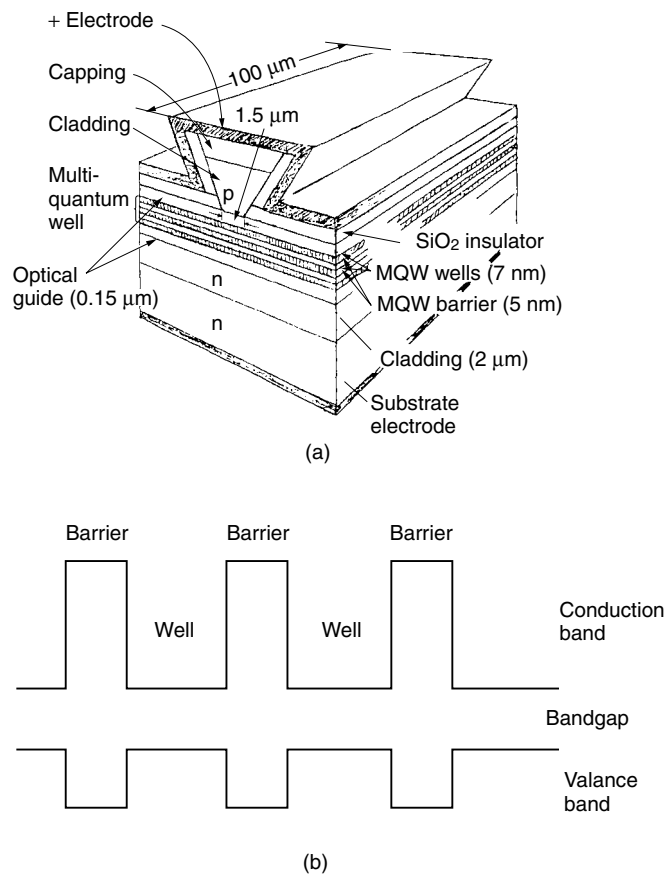

Figure 14.56 Multi-quantum well. (a) Structure of multi-quantum-well laser ($\lambda = 0.835\ \mu m$). (b) Potential well of MQW.

so that the gain of the laser is peaked at a specified frequency. A semiconductor laser using the quantum well effect has such good features as:

- Narrow frequency band gain curve
- Lower threshold current
- Less temperature dependence
- Frequency of emission that can be designed by the dimension of the wells

Let's start with an analysis of the energy states in a bulk semiconductor before going into the quantum well laser.

14.12.1 Energy States in a Bulk Semiconductor

The kinetic energy of an electron with total energy E and potential energy V is

$$\tfrac{1}{2}m_e^* v^2 = E - V \tag{14.182}$$

where v is the velocity of the particle and m_e^* is the effective mass of an electron inside the semiconductor crystal. The momentum p of such a particle is

$$p = m_e^* v \tag{14.183}$$

Combining Eqs. (14.182) and (14.183),

$$p = \sqrt{2m_e^*(E - V)} \tag{14.184}$$

It was de Broglie who postulated that any particle of matter that has momentum should also possess a wave nature, called a *matter wave*. The wavelength λ of the matter wave is given by

$$p = \frac{h}{\lambda} \tag{14.185}$$

From Eqs. (14.184) and (14.185), the wavelength is expressed as

$$\lambda = \frac{h}{\sqrt{2m_e^*(E - V)}} \tag{14.186}$$

If Eq. (14.186) is inserted into the wave equation,

$$\nabla^2 \psi + \left(\frac{2\pi}{\lambda}\right)^2 \psi = 0 \tag{14.187}$$

then the wave equation for the matter wave is obtained as

$$\nabla^2 \psi + \frac{2m_e^*(E - V)}{\hbar^2} \psi = 0 \tag{14.188}$$

where

$$\hbar = \frac{h}{2\pi} \tag{14.189}$$

Equation (14.188) is called *Schrödinger's equation*.

The wavefunction that satisfies Schrödinger's equation will be found [6]. In the bulk case, the analysis is made for the potential well constant throughout the well as shown
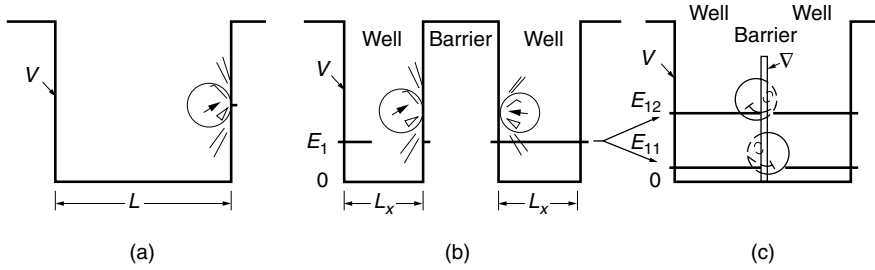
Figure 14.57 Comparison of the quantum-well structure among (a) bulk well, (b) weakly coupled double quantum well, and (c) strongly coupled double quantum well.

in Fig. 14.57a. V being constant, Eq. (14.188) becomes a linear, homogeneous, second order, partial differential equation and its general solution is

$$\psi = A \sin(k_x x + \phi_x) \sin(k_y y + \phi_y) \sin(k_z z + \phi_z) \tag{14.190}$$

Inserting Eq. (14.190) into (14.188), the values of k_x, k_y, and k_z are found as

$$\frac{2m_e^* E}{\hbar^2} = k_x^2 + k_y^2 + k_z^2 \tag{14.191}$$

where

$$V = 0 \tag{14.192}$$

is assumed inside the well.

For simplicity, let us say the electron is confined inside cubic potential walls with size L^3 as shown in Fig. 14.58. It is further assumed that the potential walls are so high that $\psi = 0$ on and outside the walls. First, the boundary condition in only the x direction is considered. In order that $\psi = 0$ at both $x = 0$ and $x = L$,

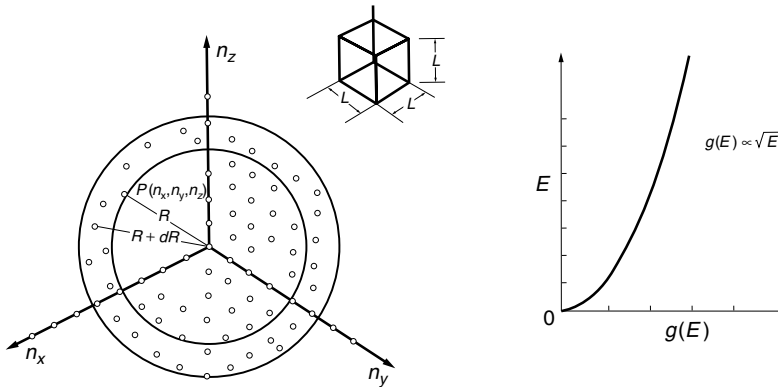$$\phi_x = 0$$
$$k_x L = n_x \pi \tag{14.193}$$

Figure 14.58 Modes in a bulk semiconductor.

where n_x is a positive integer called the mode number. Only positive integers are used for designating the mode number. Similarly,

$$k_x = \frac{\pi}{L} n_x$$

$$k_y = \frac{\pi}{L} n_y \tag{14.194}$$

$$k_z = \frac{\pi}{L} n_z$$

Thus, the solution ψ of Schrödinger's equation is

$$\psi = \sin k_x x \cdot \sin k_y y \cdot \sin k_z z \tag{14.195}$$

Let us consider (n_x, n_y, n_z) coordinates such as shown in Fig. 14.58, where n_x, n_y, n_z are positive integer points. Any one dot that is made up of a combination of n_x, n_y, n_z represents a mode of the electron motion inside the cubic potential well.

Inserting Eq. (14.194) into (14.191) gives

$$\frac{2m_e^* E}{\hbar^2} \left(\frac{L}{\pi} \right)^2 = n_x^2 + n_y^2 + n_z^2 \tag{14.196}$$

The energy level E that belongs to each mode can be calculated from Eq. (14.196).

The right hand side of Eq. (14.196) is the square of the distance R to the origin. The states having energy E lie on the sphere with radius R such that

$$R = \frac{\sqrt{2m_e^* E}}{\hbar} \frac{L}{\pi} \tag{14.197}$$

or

$$E = \frac{\hbar^2}{2m_e^*} \left(\frac{\pi}{L} \right)^2 R^2 \tag{14.198}$$

Because n_x, n_y, n_z are restricted to be integers, the associated energy levels E are also discrete, but the spacing between the adjacent energy levels is very minute (compared to the 0.8 eV energy bandgap of a $\lambda = 1.55$ μm semiconductor laser.) because when $L = 1$ mm is inserted into Eq. (14.196)

$$E = 9.2 \times 10^{-12} (n_x^2 + n_y^2 + n_z^2) \text{ eV} \tag{14.199}$$

This is the reason why the energy levels in a bulk semiconductor are practically continuous.

We are finally ready to calculate the density of states $g(E)$ of an electron in a unit volume of the bulk semiconductor. The density of states is defined such that the number of states between E and $E + dE$ is represented by $g(E) dE$. $g(E) dE$ will be found by calculating the difference between the total number of states whose associated energy is smaller than E and the total number with energy smaller than $E + dE$. Referring to Fig. 14.58, n_x, n_y, n_z are all positive integers and only the lattice points in one-eighth

of the sphere are counted. Including the orientation of the spin of the electron, the total number M of states whose associated energy is smaller than E is

$$M = 2 \left(\frac{1}{8}\right) \left(\frac{4}{3}\right) \pi R^3 \tag{14.200}$$

The number of states between E and $E + dE$ is

$$g(E)\, dE = \frac{1}{L^3} \frac{dM}{dE} dE \tag{14.201}$$

L^{-3} was included to define the quantity per unit volume. Using Eq. (14.198) in (14.200) and inserting into Eq. (14.201) finally gives

$$g(E) = \frac{\sqrt{2} m_e^{*3/2}}{\hbar^3 \pi^2} \sqrt{E} \tag{14.202}$$

Equation (14.202) is plotted as a function of E in Fig. 14.58. The function $g(E)$ is smoothly increasing starting with $E = 0$. There are no special peaks as are found with the quantum well effect, as will be shown next.

The result can easily be extended to the proof of Eq. (14.3). If an electron inside the semiconductor has an effective mass and total energy E_2, and the potential energy is taken as $V = E_c$, then instead of Eq. (14.192), the density $g_c(E_2)$ of the states per unit volume in the conduction band is

$$g_c(E_2) = \frac{\sqrt{2} m_e^{*3/2}}{\hbar^3 \pi^2} \sqrt{E_2 - E_c} \tag{14.203}$$

which is Eq. (14.3).

14.12.2   Energy States in a Quantum Well

Figures 14.57b and 14.57c show the MQW of the simplest kind. Two wells are partitioned by a potential barrier. When the potential barrier is set too high and wide, as shown in Fig. 14.57b, an electron in one well cannot tunnel across the potential barrier to the adjacent well, and the electron remains in the same well. The motion of such an electron can be treated as if the electron is inside a single well. If there are N wells, the problem can be treated as if there are N separate wells. This case is classified as the weakly coupled case. In the weakly coupled case, the analysis for the single electron in one potential well applies to every well and the analysis is simple.

However, when the barrier becomes thin and narrow, as in Fig. 14.57c, the tunneling effect becomes significant and the electrons begin to sneak into each other's wells. This is similar to what happens to photons in an optical directional coupler, where photons in one of the optical guides sneak into the other guide by means of the evanescent wave if the spacing is narrow. This case is classified as the strongly coupled case. The analysis of strong coupling is much more complicated than that of weak coupling, and for this reason only the weakly coupled case will be presented here.

The case when an electron is confined in one of the two potential wells shown in Fig. 14.57b will be treated. The barrier wall is assumed to be so high and thick that the electron inside the well cannot penetrate into the wall and the wavefunction is zero on and inside the potential barrier. The width L_x of the well in the x direction

is significantly narrower than the other two dimensions, which are assumed L. The boundary conditions in Eq. (14.194) have to be modified. The wavefunction in the x direction is

$$X(x) = A \sin(k_x x + \phi_x) \qquad (14.204)$$

In the quantum well, $X(x)$ has to vanish at both walls at $x = 0$ and $x = L_x$. This means that $X(0) = 0$, $\phi_x = 0$, and

$$X(x) = A \sin k_x x \qquad (14.205)$$

Equation (14.205) has to satisfy yet another boundary condition:

$$X(L_x) = 0 \qquad (14.206)$$

hence,

$$k_x L_x = n_x \pi \qquad (14.207)$$

where n_x is a positive integer

$$n_x = 1, 2, 3, 4, \ldots \qquad (14.208)$$

Thus, Eqs. (14.194) and (14.196) have to be modified as

$$k_x = \frac{\pi}{L_x} n_x$$
$$k_y = \frac{\pi}{L} n_y \qquad (14.209)$$
$$k_z = \frac{\pi}{L} n_z$$

$$\frac{2m_e^* E}{\hbar^2} \left(\frac{L}{\pi}\right)^2 = n_x'^2 + n_y^2 + n_z^2 \qquad (14.210)$$

with

$$n_x' = \frac{L}{L_x} n_x \qquad (14.211)$$

Figure 14.59 represents the lattice points in n_x', n_y, n_z coordinates. From Eq. (14.211), as n_x changes with unit increment, n_x' changes with a large increment because L/L_x is a large number like 10^5. As a result, the lattice points look more like sheets. There are no lattice points in the region

$$0 < n_x' = \frac{L}{L_x} \qquad (14.212)$$

and the first sheet appears in the plane of

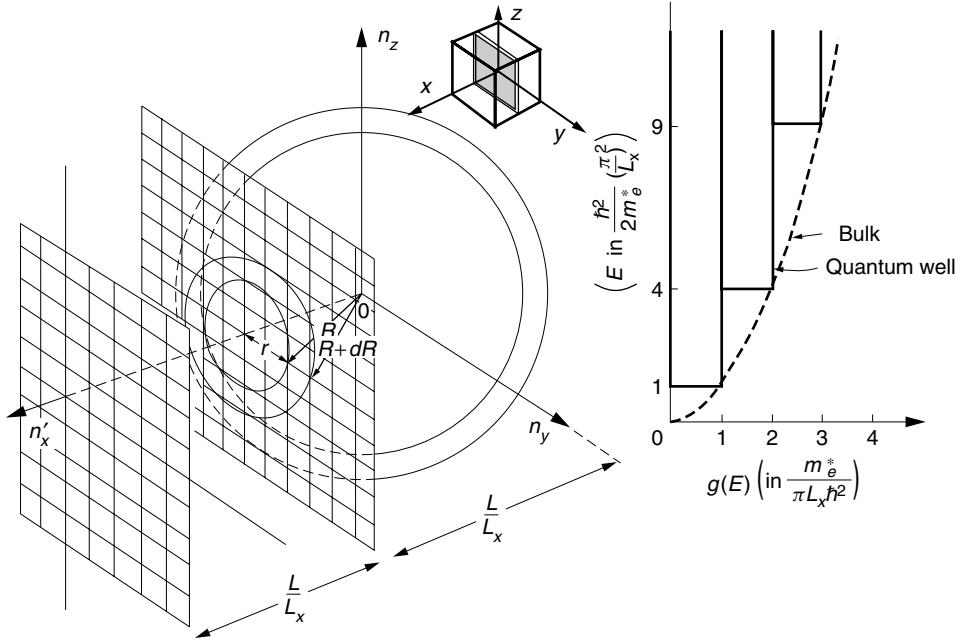$$n_x' = \frac{L}{L_x} \qquad (14.213)$$

Figure 14.59   Modes in a quantum well.

The associated energy level of the mode where the sphere is tangent to the sheet is obtained from Eq. (14.210) with Eq. (14.213) and $n_y = n_z = 0$ as

$$E_1 = \frac{\hbar^2}{2m_e^*} \left(\frac{\pi}{L_x} \right)^2 \tag{14.214}$$

which is indeed the first quantized energy level of the electron in the potential well. The next sheet appears at twice the distance, and the subsequent n_xth sheet appears at

$$n_x' = \frac{L}{L_x} n_x \tag{14.215}$$

The points for a given energy E are located on the surface of the sphere with radius R given by Eq. (14.198). With the configuration shown in Fig. 14.59, first consider the case when the sphere is cut by only one sheet and R is larger than L/L_x but smaller than $2L/L_x$, or from Eq. (14.198),

$$\frac{\hbar^2}{2m_e^*} \left(\frac{\pi}{L_x} \right)^2 < E < \frac{\hbar^2}{2m_e^*} \left(2\frac{\pi}{L_x} \right)^2 \tag{14.216}$$

The energy represented by the points in the first sheet with $n_x = 1$ is

$$E = \frac{\hbar^2}{2m_e^*} \left(\frac{\pi}{L} \right)^2 \left[\left(\frac{L}{L_x} \right)^2 + r^2 \right] \tag{14.217}$$

where

$$r^2 = n_y^2 + n_z^2$$

In order to find the density of states, the number of modes M with energy less than E has to be found. Recall that n_x and n_y are positive integers and only the lattice points in one-quarter of the circle are counted, and there are two spin states for each point.

$$M = \left(\frac{1}{4}\right)(2)\pi r^2 \tag{14.218}$$

The rate of increase in M with respect to r is

$$\frac{dM}{dr} = \pi r \tag{14.219}$$

On the other hand, the rate of increase in E with respect to r is

$$\frac{dE}{dr} = \frac{\hbar^2}{m_e^*}\left(\frac{\pi}{L}\right)^2 r \tag{14.220}$$

Thus, the rate of increase in M with respect to E is

$$\frac{dM}{dE} = \frac{dM}{dr}\frac{dr}{dE} = \frac{m_e^* L^2}{\pi\hbar^2} \tag{14.221}$$

Equation (14.221) has to be divided by the volume $L_x L^2$ of the potential well in order to obtain the density of states per unit volume

$$g_1(E) = \frac{m_e^*}{\pi L_x \hbar^2} \tag{14.222}$$

Note that $g_1(E)$ is independent of r, R, and E.

Next, the case when the sphere intercepts two sheets is considered. The rate of increase in M in the second sheet is obtained with $n_x = 2$. Only the first term in Eq. (14.210) has the factor n_x, but this n_x soon disappears when dM/dr and dE/dr are calculated. The density of states for $n_x = 2$ is the same as before, and is Eq. (14.222), but now the sphere is cut by two sheets, and the rate of increase in the number of states for each sheet is independent of R. The total increase in states is simply the addition of the two contributions, and

$$g_2(E) = 2\frac{m_e^*}{\pi L_x \hbar^2} \tag{14.223}$$

Finally, the density of states at an arbitrary energy level is considered. Every time a new sheet is cut by the sphere, the density of the states increases by $m_e^*/\pi L_x \hbar^2$. The density of states per unit volume inside the potential well is therefore

$$g(E) = \frac{m_e^*}{\pi L_x \hbar^2}\sum_{n=1}^{N} H(E - E_{x_n}) \tag{14.224}$$

where

$$E_{x_n} = \frac{\hbar^2}{2m_e^*}\left(n_{x_n}\frac{\pi}{L_x}\right)^2 \tag{14.225}$$

and $H(x)$ is *Heavyside's step function*, defined as

$$H(x) = \begin{cases} 0 & x < 0 \\ \frac{1}{2} & x = 0 \\ 1 & x > 0 \end{cases} \tag{14.226}$$

The curve of $g(E_x)$ looks like a staircase function. As compared to the smooth curve of the bulk semiconductor laser, it steps up by $m_e^*/\pi L_x \hbar^2$ every time E_x exceeds E_{n_x}, as shown in Fig. 14.59.

Next, the influence of this staircase like function on the gain curve is explained.

14.12.3 Gain Curves of the MQW Laser

The gain curve has already been calculated for a bulk p-n junction laser as described in Section 14.2.1. A similar approach will be used to calculate the gain curve of the active layer of the MQW laser. Using the Fermi–Dirac distribution function, the number of states that are occupied in the energy levels between E_2 and $E_2 + dE_2$ in the conduction band is given by

$$N = \int g_c(E_2) f_c(E_2) \, dE_2 \tag{14.227}$$

and that of holes in the valence band is

$$P = \int g_v(E_1)[1 - f_v(E_1)] \, dE_1 \tag{14.228}$$

Figures 14.60a–c show the operation $g_c(E_2)f_c(E_2)$ and $g_v(E_1)[1 - f_v(E_1)]$. The width of $g_c(E_2)f_c(E_2)$ for a MQW laser is narrower in the E axis dimension than that shown by the dashed line of a bulk laser. This is the very reason why the MQW laser has a more pointed and higher peak gain in a narrower frequency band than a bulk laser does.

A narrower curve means more efficient use of the injection current and hence the reduction of N_α. The reduction of N_α leads to a variety of advantages such as a higher gain in Eq. (14.26), a lower J_{th} in Eq. (14.49), a larger power in Eq. (14.58), a shorter turn-on time in Eq. (14.61), and a higher modulation frequency ω_r in Eq. (14.89).

In the following, an outline for calculating the gain will be presented. The gain curve of the MQW laser will be obtained by calculating the quasi-Fermi level for a given carrier density. Then the calculated quasi-Fermi levels are used to calculate the gain in Eq. (14.25). The carrier densities need to be calculated first before calculating the Fermi level. From Eq. (14.2), the number N of electrons in the entire conduction band is

$$N = \int g_c(E_2) f_c(E_2) \, dE_2$$

$$= \frac{m_e^*}{\pi L_x \hbar^2} \sum_{n=1}^{\infty} n \int_{E_{x_n}}^{E_{x(n+1)}} \frac{dE_2}{e^{(E_2 - F_c)/kT} + 1} \tag{14.229}$$
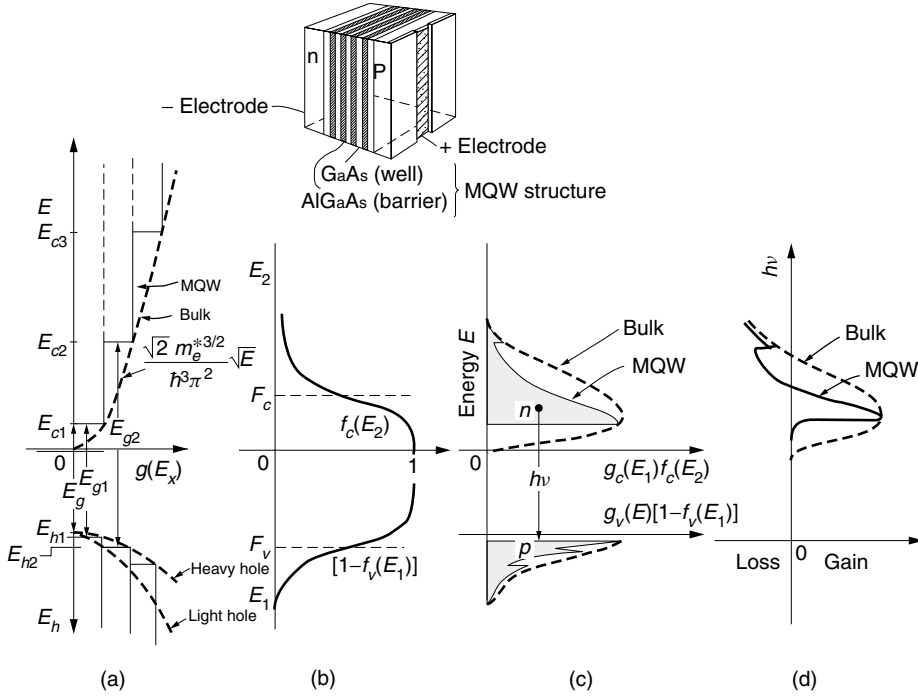
Figure 14.60 Composite diagram to explain the operation of a MQW laser. (a) Density $g(E)$ of energy states. (b) Fermi levels $f(E_2)$ and $[1 - f_v(E_1)]$. (c) Population density $g_c(E_2)f_c(E_2)$ and $g_v(E_1)[1 - f_v(E_1)]$. (d) Gain of the MQW laser.

Using the relationship

$$\int \frac{dx}{e^x + 1} = -\ln(e^{-x} + 1) \tag{14.230}$$

the integral of Eq. (14.229) is calculated as

$$
\begin{aligned}
N = \frac{m_e^* kT}{\pi L_x \hbar^2} \Big\{ &1 \left[\ln \left(e^{-(E_{c1} - F_c)/kT} + 1 \right) - \ln \left(e^{-(E_{c2} - F_c)/kT} + 1 \right) \right] \\
&+ 2 \left[\ln \left(e^{-(E_{c2} - F_c)/kT} + 1 \right) - \ln \left(e^{-(E_{c3} - F_c)/kT} + 1 \right) \right] \\
&+ 3 \left[\ln \left(e^{-(E_{c3} - F_c)/kT} + 1 \right) - \ln \left(e^{-(E_{c4} - F_c)/kT} + 1 \right) \right] \\
&+ \cdots \Big\}
\end{aligned}
\tag{14.231}
$$

Aside from the very first square bracket in Eq. (14.231), the first terms in all the subsequent square brackets are reduced by an amount that corresponds to the second term in the previous square brackets, and Eq. (14.231) becomes

$$N = \frac{m_e^*}{\pi L_x \hbar^2} kT \sum_{n=1}^{\infty} \ln \left(1 + e^{(F_c - E_{cn})/kT} \right) \tag{14.232}$$

Similarly, the density of holes in the valence band is

$$P = \frac{m_h^*}{\pi L_x \, \hbar^2} kT \sum_{n=1}^{\infty} \ln \left(1 + e^{(E_{hn} - F_v)/kT} \right) \tag{14.233}$$

If the assumption is made that only the $n = 1$ level is filled with carriers, the quasi-Fermi levels of the MQW as a function of the carrier concentration are

$$F_c = E_{c1} + kT \ln \left(e^{N/N_c^Q} - 1 \right) \tag{14.234}$$

$$F_v = E_{h1} - kT \ln \left(e^{P/N_v^Q} - 1 \right) \tag{14.235}$$

where

$$N_c^Q = \frac{m_e^* kT}{\pi L_x \, \hbar^2}$$

$$N_v^Q = \frac{m_h^* kT}{\pi L_x \, \hbar^2} \tag{14.236}$$

The quasi-Fermi levels together with Eqs. (14.2)–(14.4) and (14.5)–(14.7) are inserted into Eq. (14.19) to calculate the gain curve. The calculated gain curves for a $Ga_{0.47}$ $In_{0.53}As$/InP MQW laser are shown in Fig. 14.61 [36].

General observations concerning the calculated results show that, compared to the bulk p-n junction laser of Fig. 14.5 represented by the dashed line in Fig. 14.61, the MQW laser has the following characteristics:

- A narrower, more pointed gain curve
- A higher peak gain
- A shift of the center toward higher frequency from that of the bulk

The narrower pointed curve contributes to the stability of the oscillation. As mentioned earlier, the higher peak gain means a lowering of the MQW laser threshold current. The dependence of the shift of the center frequency on L_x means that the frequency of the MQW laser can be designed by adjusting L_x, as shown in Example 14.7.

14.12.4 Structure and Characteristics of a MQW Laser

The structure and characteristics of the MQW laser will be explained by taking a specific example of a MQW laser of the ridge type shown in Fig. 14.56a. There are three quantum wells 7-nm thick with 5-nm barriers. The quantum wells are sandwiched by 0.15-μm-thick optical guides made of $Al_{0.28}Ga_{0.72}As$ whose refractive index is $n = 3.50$. The optical guide/quantum wells/optical guide structure is further sandwiched by 2-μm-thick cladding layers of $Al_{0.8}Ga_{0.2}As$ whose refractive index is $n = 3.27$, which is lower than that of the guiding layer. The light is confined in the optical guide centered by the multi-quantum wells.

The quantum wells being thin, the confinement factor Γ (see Section 13.7) is 3.5%. Let n_w denote the number of quantum wells. If n_w is increased in order to improve the overall confinement factor, the injection carrier density $N = \tau J / 2etn_w$ decreases with an increase in the total thickness tn_w, where t is the thickness of the potential well and J is limited by the heat dissipation. There is an optimum number of quantum wells.
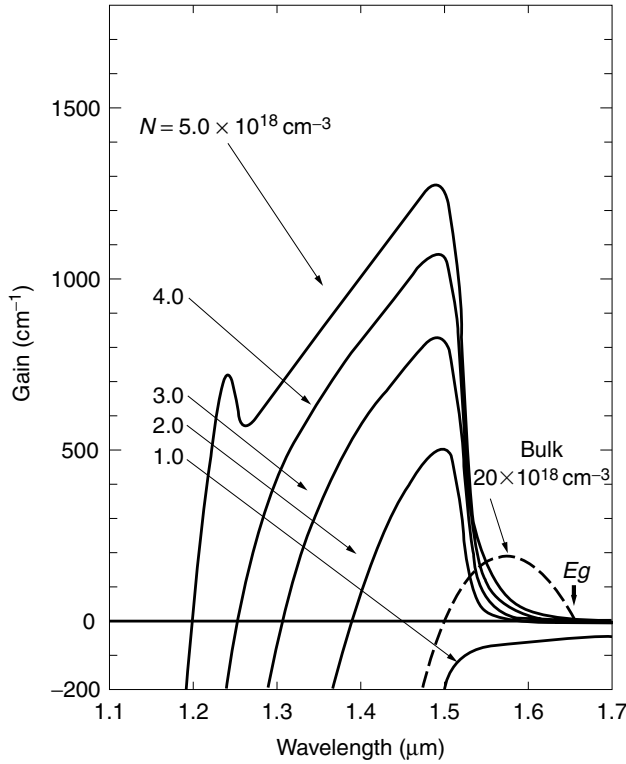
Figure 14.61   Gain spectrum of a $Ga_{0.47}In_{0.53}As/InP$ MQW laser with $L_x = 100$ Å. (After M. Asada, A. Kameyama, and Y. Suematsu [36].)

A capping layer that adheres to both metal and semiconductor materials is deposited on top of the upper cladding layer. These two layers are then etched to form a mesa structure (steep hill structure). A SiO_2 insulating layer is deposited except in the region of the capping layer. Then the positive electrode is deposited. The injection current is constricted in the narrow neck region at the bottom of the ridge.

Finally, both front and rear facets of the laser are coated with high reflection coatings with $R_f = 70\%$ and $R_r = 86\%$, respectively. The total length of the laser cavity is 100 μm.

The operational characteristics of this specific MQW laser are summarized as follows. The threshold current is 3.98 mA and is less than one-tenth the threshold current of a bulk double heterojunction laser. As mentioned earlier, this low threshold current means:

1. Biasing is practically unnecessary.
2. The relaxation oscillation decays fast and a high bit rate is possible.
3. The turn-on delay time is short.
4. The temperature dependence is less.

Expanding on the last point, the characteristic temperatures are large for this MQW laser ($T_0 = 154$ K and $T'_0 = 352$ K). The output power change is ± 0.5 dB for the temperature range $25 \pm 25\,°C$.

Example 14.7 $Ga_{0.47}In_{0.53}$ As grown on an InP substrate was used as a material in the potential well of a MQW laser. The energy gap of the semiconductor is $E_g = 0.75$ eV. The potential barrier was made thick enough to assume the weakly coupled case. The width of the well is $L_x = 10$ nm.

The effective masses of $Ga_xIn_{1-x}As_yP_{1-y}$ grown on an InP substrate ($y = 2.2x$) are given by

$$m_e^* = (0.080 - 0.039y)m_0$$
$$m_h^* = (0.4 + 0.05y)m_0 \qquad (14.237)$$
$$m_0 = \text{electron mass} = 0.9109 \times 10^{-30} \text{ kg}$$

(a) Calculate the values and fill in the blanks in the graph in Fig. 14.62.
(b) Design the well width L_x of the MQW laser of the same material so that the wavelength of the emitted light becomes 1.55 μm.

Solution
(a) The mole fractions of the given semiconductor are
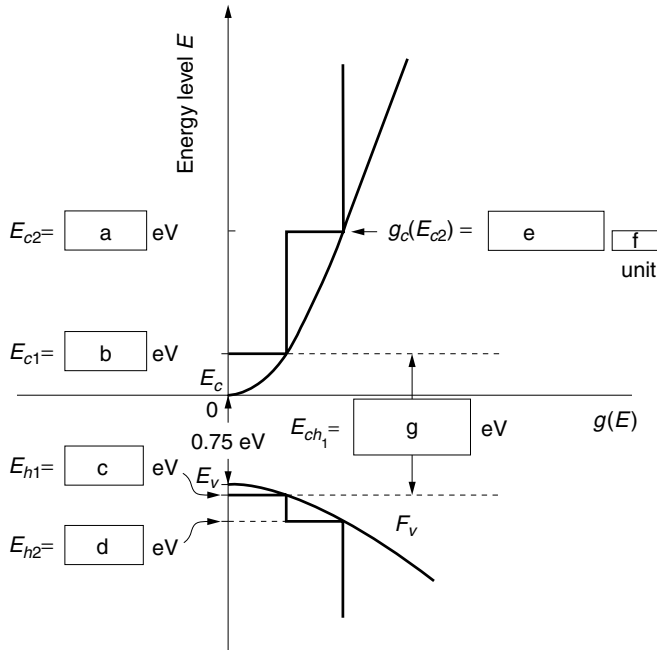
$$x = 0.47 \quad \text{and} \quad y = 1.0$$

Figure 14.62 Density $g(E)$ of states versus energy level for a $Ga_{0.47}In_{0.53}As$ MQW laser. The quantities (a)–(g) are to be calculated.

Thus, the effective masses are

$$m_e^* = 0.041 m_0$$

$$m_h^* = 0.45 m_0$$

The lowest quantized energy state in the conduction band E_{c1} is obtained using Eq. (14.214):

$$E_{c1} = \frac{\hbar^2}{2m_e^*} \left(\frac{\pi}{L_x}\right)^2 \tag{14.238}$$

$$E_{c1} = \frac{(1.055 \times 10^{-34})^2}{2(0.041)(0.9109 \times 10^{-30})} \left(\frac{\pi}{10^{-8}}\right)^2 \frac{1}{1.6 \times 10^{-19}}$$

The last factor is to convert joules into electron volts:

$$E_{c1} = 0.0919 \text{ eV}$$

The second lowest quantized energy state is, from Eq. (14.225),

$$E_{c2} = 4E_{c1} = 4(0.0919) = 0.368 \text{ eV}$$

The quantized energy states E_{h1} in the valence band can be found from the ratio of the effective masses of m_h^* and m_e^*

$$E_{h1} = 0.0919 \frac{0.041}{0.45} = 0.00837 \text{ eV}$$

$$E_{h2} = 0.368 \frac{0.041}{0.45} = 0.0335 \text{ eV}$$

Note that E_{h1} and E_{h2} are measured downward from the band edge of the valence band.

Next, the density of states $g_1(E)$ of the electrons per unit energy per unit volume is, from Eq. (14.222),

$$g_c(E_{c2}) = 2g_1(E) = \frac{2m_e^*}{\pi L_x \hbar^2}$$

$$= \frac{(2)(0.041)(0.9109 \times 10^{-30})}{\pi(10^{-8})(1.055 \times 10^{-34})^2}$$

$$= 2.14 \times 10^{44} (\text{J} \cdot \text{m}^3)^{-1}$$

This value is converted into the unit of $(\text{eV} \cdot \text{cm}^3)^{-1}$

$$[2.14 \times 10^{44} (\text{J} \cdot \text{m}^3)^{-1}](1.6 \times 10^{-19})(10^{-6}) = 3.42 \times 10^{19} (\text{eV} \cdot \text{cm}^3)^{-1} \tag{14.239}$$

The units of $g_c(E_{c2})$ are per unit energy per unit volume, which is verified by

$$\frac{m_e^*}{\pi L_x \hbar^2} = \frac{\text{kg}}{\text{m}(\text{J} \cdot \text{s})^2} = \frac{1}{\text{J} \cdot \text{m}^3} \tag{14.240}$$

where use was made of

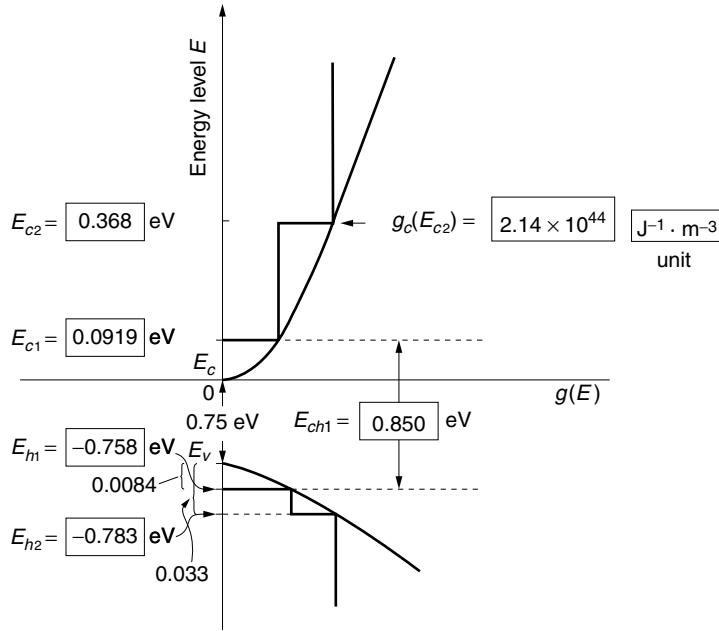$$\text{J} = \text{force} \times \text{distance} = \text{kg}\frac{\text{m}}{\text{s}^2} \cdot \text{m}$$

Figure 14.63 The density $g(E)$ of states versus energy level for a $Ga_{0.47}In_{0.53}As$ MQW laser. The results of the calculations in Fig. 14.62 are given.

Thus, $\int g(E_c)\,dE_c$ represents the number of states per unit volume. The results are shown in Fig. 14.63.

The energy bandgap between the bottom of the quantized level in the conduction band and top of the quantized level in the valence band is

$$E_{c1} + E_{h1} + 0.75 = 0.850 \text{ eV}$$

(b) The quantum of the $\lambda = 1.55$ μm photon is

$$h\nu = (4.14 \times 10^{-15}) \left(\frac{3 \times 10^8}{1.55 \times 10^{-6}} \right)$$

$$= 0.801 \text{ eV}$$

Alternatively, this result could have been obtained directly from the formula

$$\lambda = \frac{1.24}{E \text{ (eV)}} \mu m \tag{14.241}$$

From the energy diagram, we have

$$E_{c1} + E_{h1} + E_g = h\nu \tag{14.242}$$

$$\left[\frac{\hbar^2}{2m_e^*} \left(\frac{\pi}{L_x} \right)^2 + \frac{\hbar^2}{2m_h^*} \left(\frac{\pi}{L_x} \right)^2 \right] \frac{1}{1.6 \times 10^{-19}} + 0.75 = 0.801$$

Solving for L_x gives

$$L_x = 14 \text{ nm} \qquad \qquad \Box$$

By expanding the quantum size effect to two dimensions, and then to all three dimensions, a quantum wire structure and a quantum dot (box) structure can be formed, respectively. Lasers using the quantum effect in more than one dimension further accentuate the merits of the MQW lasers [37,38]. In the next section, the density of states for the quantum wire and quantum dot will be obtained for comparison with the quantum well.

14.12.5 Density of States of a Quantum Wire and Quantum Dot

Such a potential well as shown in Fig. 14.64 confined in both x and y directions is called a quantum wire. With the quantum wire, Eq. (14.196) is modified as

$$\frac{2m_e^* E}{\hbar^2} \left(\frac{L}{\pi} \right)^2 = n_x'^2 + n_y'^2 + n_z^2 \qquad (14.243)$$

with

$$n_x' = \frac{L}{L_x} n_x \qquad (14.244)$$

$$n_y' = \frac{L}{L_y} n_y \qquad (14.245)$$

Let us assume

$$L_x = L_y = L_d \qquad (14.246)$$

L_x and L_y are significantly narrower than L and the lattice spacings are now wide in both x and y directions and narrow only in the z direction. The lattice points corresponding to the lowest energy look like a post located at $n_x' = n_y' = L/L_d$, as shown in Fig. 14.64a. Since neither n_x' nor n_y' is allowed to be negative, posts exist only in the first quadrant of the $n_x' - n_y'$ plane. The radius R_1 of the sphere that just touches the post nearest the origin is $\sqrt{2}L/L_d$ and its associated energy E_1 is, from Eq. (14.198),

$$E_1 = \frac{\hbar^2}{m_e^*} \left(\frac{\pi}{L_d} \right)^2 \qquad (14.247)$$

Toward the objective of finding the density of states, the number of modes M with energy smaller than E will be calculated by counting the lattice points that are enclosed by the sphere. From Figs. 14.64b and 14.64c, the number of modes M is equal to r and

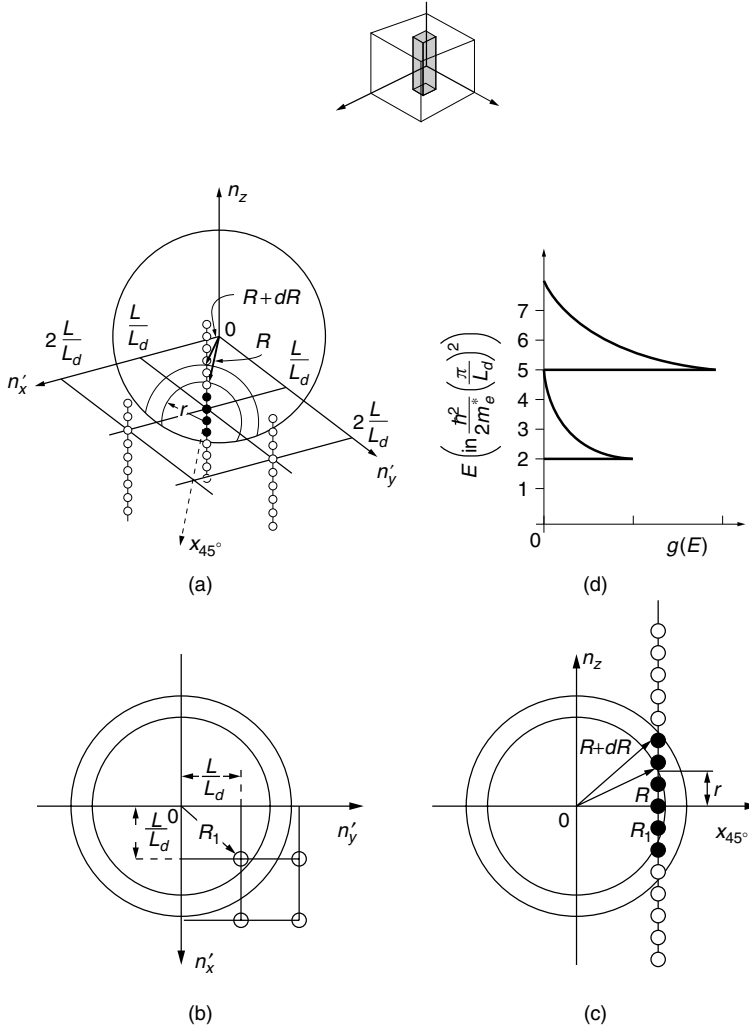$$M = \sqrt{R^2 - R_1^2} \qquad (14.248)$$

Figure 14.64 Calculation of the density of states of a quantum wire. (a) Lattice points. (b) Plan view. (c) Side view. (d) Density of states.

and

$$\frac{dM}{dR} = \frac{R}{\sqrt{R^2 - R_1^2}} \tag{14.249}$$

From Eq. (14.198), the derivative of E with respect to R is

$$\frac{dE}{dR} = \frac{\hbar^2}{2m_e^*} \left(\frac{\pi}{L}\right)^2 \cdot 2R \tag{14.250}$$

The number of modes dM between E and $E + dE$ is

$$dM = \frac{dM}{dR} \frac{dR}{dE} \, dE \tag{14.251}$$

Multiplying by 2 for spin states and dividing by LL_d^2 for the number per unit volume, the number of states $g_1(E)\,dE$ between E and $E + dE$ becomes

$$g_1(E)\,dE = \frac{2}{LL_d^2} \frac{dM}{dR} \frac{dR}{dE} \, dE \tag{14.252}$$

Inserting Eqs. (14.249) and (14.250) into Eq. (14.252) and summarizing the results gives

$$g_1(E) = \begin{cases} 0 & E < E_1 \\ \dfrac{\sqrt{2m_e^*}}{\hbar} \dfrac{1}{\pi L_d^2} \dfrac{1}{\sqrt{E - E_1}} & E > E_1 \end{cases} \tag{14.253}$$

with

$$E_1 = 2\frac{\hbar^2}{2m_e^*}\left(\frac{\pi}{L_d}\right)^2 \tag{14.254}$$

$g_1(E)$ is zero until the sphere reaches the first post and then becomes $g_1(E)$ after the sphere encloses the first post. $g_1(E)$ decreases with $\sqrt{E - E_1}$.

With a further increase in the radius of the sphere, the sphere simultaneously reaches the next two posts located at $n_x' = L/L_d$, $n_y' = 2L/L_d$ and at $n_x' = 2L/L_d$, $n_y' = L/L_d$.

Both posts are located at a distance $\sqrt{5}L/L_d$ from the origin. The energy associated with the radius is, from Eq. (14.198),

$$E_2 = 5\frac{\hbar^2}{2m_e^*}\left(\frac{\pi}{L_d}\right)^2 \tag{14.255}$$

The density of states $g_2(E)$ associated with these two posts is obtained in a similar manner as Eq. (14.253) and

$$g_2(E) = \begin{cases} 0 & E < E_2 \\ \dfrac{\sqrt{2m_e^*}}{\hbar} \dfrac{2}{\pi L_d^2} \dfrac{1}{\sqrt{E - E_2}} & E > E_2 \end{cases} \tag{14.256}$$

with

$$E_2 = 5\frac{\hbar^2}{2m_e^*}\left(\frac{\pi}{L_d}\right)^2 \tag{14.257}$$

With the sphere totally enclosing the first three posts, the density of states becomes

$$g(E) = \begin{cases} 0 & E < E_1 \\ g_1(E) & E_1 < E < E_2 \\ g_1(E) + g_2(E) & E_2 < E < E_3 \end{cases} \tag{14.258}$$

where

$$E_3 = 9\frac{\hbar^2}{2m_e^*}\left(\frac{\pi}{L_d}\right)^2 \tag{14.259}$$

For the region $E > E_3$ the density of states can be obtained in a similar manner.

The overall density of states of the quantum wire is plotted in Fig. 14.64d. The regions of high density of states are more concentrated than those of the quantum well.

Next, the density of states of the quantum dot will be calculated. The quantum dot has walls in all three dimensions, as shown in the inset of Fig. 14.65. Equation (14.196) has to be modified as

$$\frac{2m_e^* E}{\hbar^2} \left(\frac{L}{2\pi} \right)^2 = n_x'^2 + n_y'^2 + n_z'^2 \tag{14.260}$$

Let us assume that

$$L_x = L_y = L_z = L_d \tag{14.261}$$

The lattice points are dispersed in the (n_x', n_y', n_z') space. The density of states is zero until the sphere reaches the lattice point nearest the origin, which is located at

$$(n_x', n_y', n_z') = \frac{L}{L_d}(1, 1, 1) \tag{14.262}$$

The radius of the sphere that reaches the nearest lattice point is

$$R = \sqrt{3} \left(\frac{L}{L_d} \right) \tag{14.263}$$
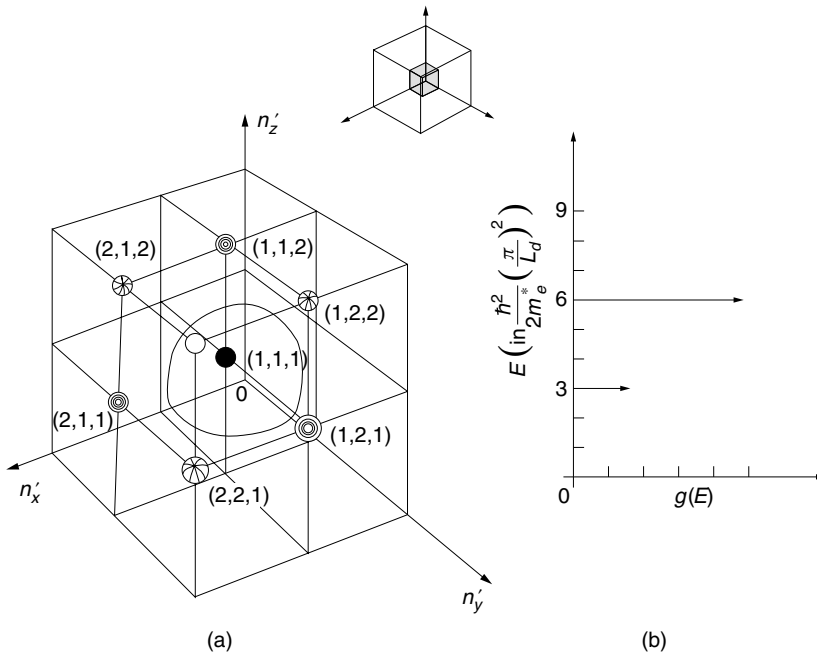

(a)   (b)

Figure 14.65   Calculation of the density of states of a quantum dot. (a) Lattice points. (b) Density of states.

The energy E associated with this sphere is, from Eq. (14.198),

$$E_1 = 3\frac{\hbar^2}{2m_e^*}\left(\frac{\pi}{L_d}\right)^2 \qquad (14.264)$$

Thus, after multiplying by 2 for spin states, the density of states $g_1(E)$ before reaching the second nearest lattice points is

$$g_1(E) = 2\delta(E - E_1) \quad \text{for } E < E_1 \qquad (14.265)$$

The next lattice points are located at

$$(n_x', n_y', n_z') = \begin{cases} \dfrac{L}{L_d}(2, 1, 1) \\[2mm] \dfrac{L}{L_d}(1, 2, 1) \\[2mm] \dfrac{L}{L_d}(1, 1, 2) \end{cases} \qquad (14.266)$$

These are all in the radius

$$R = \sqrt{6}\left(\frac{L}{L_d}\right) \qquad (14.267)$$

The energy E associated with the sphere is, from Eq. (14.198),

$$E_2 = 6\frac{\hbar^2}{2m_e^*}\left(\frac{\pi}{L_d}\right)^2 \qquad (14.268)$$

Thus, the density of states $g_2(E)$ before reaching E_3 is

$$g_2(E) = 6\delta(E - E_2) \quad \text{for } E < E_2 \qquad (14.269)$$

The next lattice points are located at

$$(n_x', n_y', n_z') = \begin{cases} \dfrac{L}{L_d}(2, 2, 1) \\[2mm] \dfrac{L}{L_d}(2, 1, 2) \\[2mm] \dfrac{L}{L_d}(1, 2, 2) \end{cases} \qquad (14.270)$$

These are all at the radius
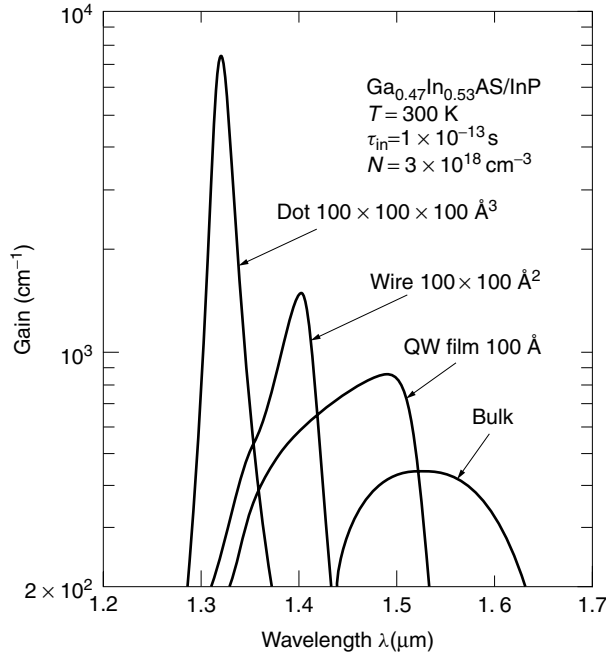
$$R = \sqrt{9}\left(\frac{L}{L_d}\right) \qquad (14.271)$$

Figure 14.66 Gain spectra calculated for $Ga_{0.47}In_{0.53}As/InP$: $100 \times 100 \times 100$ Å^3 cubic quantum dot, 100×100 Å^2 quantum wire, 100 Å quantum film, and bulk crystal at $T = 300$ K. (After M. Asada, Y. Miyamoto, and Y. Suematsu [37].)

The energy E associated with the sphere is, from Eq. (14.198),

$$E_3 = 9 \frac{\hbar^2}{2m_e^*} \left(\frac{\pi}{L_d} \right)^2 \tag{14.272}$$

The results are plotted in Fig. 14.65b. They consist of a series of delta functions and the curve of the density of states of the quantum dot is the sharpest of all three kinds of quantum effects. Also, by repeating the same procedure as demonstrated in Fig. 14.4, the order of the gain curves from sharpest to least sharp is as follows: quantum dot, quantum wire, quantum well, and then bulk. Calculated results are shown in Fig. 14.66.

14.13 ERBIUM-DOPED FIBER LASER

An erbium-doped fiber amplifier can immediately be converted into a fiber laser if its output light is fed back to the input port. The feedback is achieved either by connecting the input port to the output port, forming a ring-type fiber laser, or by installing reflectors at the input and output ports, thereby creating a Fabry–Pérot-type fiber laser. The hybrid of the above two types is known as a *sigma laser*.
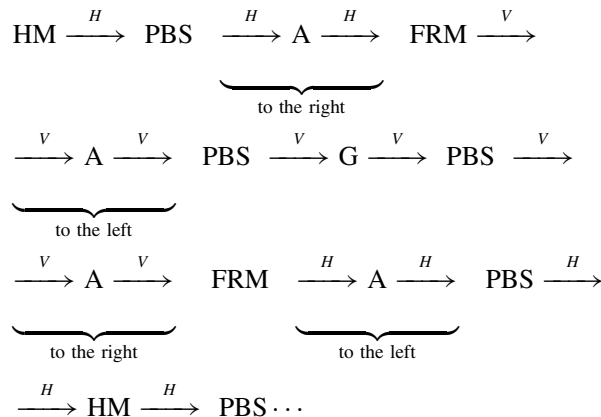
Figure 14.67a shows a schematic of the ring-type fiber laser. The traveling-wave [39] operation eliminates the problem of spatial hole burning (see Section 14.4.3.3). To

ensure the traveling-wave excitation, an optical isolator is installed. The optical isolator allows propagation in only one direction, as indicated by the arrow in Fig. 14.67a.

Since the length of the fiber ring is long, the frequency spacing between the longitudinal modes is close. For instance, from Eq. (14.36), $\Delta\nu$ is of the order of 10 MHz for a ring length of 10 meters. Tight control of the fiber length is important in order for the ring laser to be free from mode instabilities due to either temperature or vibration. A device for stretching the fiber is installed to fine tune the length of the fiber ring. The fiber is stretched by means of a piezoelectric ceramic cylinder onto which the fiber is wound. The diameter of the cylinder is controlled by the servolooped applied electric field [40] to stabilize the wavelength of oscillation.

Figure 14.67b is a schematic of the Fabry–Pérot-type fiber laser [41]. Referring to the diagram, the components and their symbols are explained as follows. An erbium-doped fiber amplifier A serves as the active medium. The reflector HM on the left is a half-mirror, and the reflector FRM on the right is a combination of Faraday rotator and mirror. The direction of polarization of the wave reflected from the FRM is rotated by 90°, which means that horizontally polarized light after reflection is converted into a vertically polarized wave, or vice versa. The polarizing beamsplitter (PBS) reflects the vertically polarized wave and transmits the horizontally polarized wave (see Section 6.5.2). The external grating G controls the wavelength of oscillation.

The path of light through the Fabry–Pérot fiber laser will now be traced. The directions of polarization are indicated by H and V for horizontal and vertical polarization, respectively. The starting point is taken as the light just reflected from mirror HM.

$$\text{HM} \xrightarrow{H} \text{PBS} \xrightarrow{H} \text{A} \xrightarrow{H} \text{FRM} \xrightarrow{V}$$

$$\underbrace{\qquad\qquad\qquad}_{\text{to the right}}$$

$$\xrightarrow{V} \text{A} \xrightarrow{V} \text{PBS} \xrightarrow{V} \text{G} \xrightarrow{V} \text{PBS} \xrightarrow{V}$$

$$\underbrace{\qquad\qquad}_{\text{to the left}}$$

$$\xrightarrow{V} \text{A} \xrightarrow{V} \text{FRM} \xrightarrow{H} \text{A} \xrightarrow{H} \text{PBS} \xrightarrow{H}$$

$$\underbrace{\qquad\qquad}_{\text{to the right}} \qquad \underbrace{\qquad\qquad}_{\text{to the left}}$$

$$\xrightarrow{H} \text{HM} \xrightarrow{H} \text{PBS} \cdots$$

As seen above, the directions of polarization of the two counterpropagating waves in A are always perpendicular to each other so that no standing wave is formed and the problem of spatial hole burning is eliminated.

Figure 14.67c is a hybrid of the above two systems and is called a sigma laser [41]. Instead of being reflected back by a mirror at the left end, the light beam makes a U-turn. The U-turn contains a kind of optical isolator that is accompanied by a rotation of the direction of polarization by 90° (the optical isolator can be replaced by a polarization-maintaining fiber twisted by 90°).

Let us say a horizontally polarized beam is incident onto the PBS from A. The beam will pass straight through the PBS and reach the optical isolator. The output from the
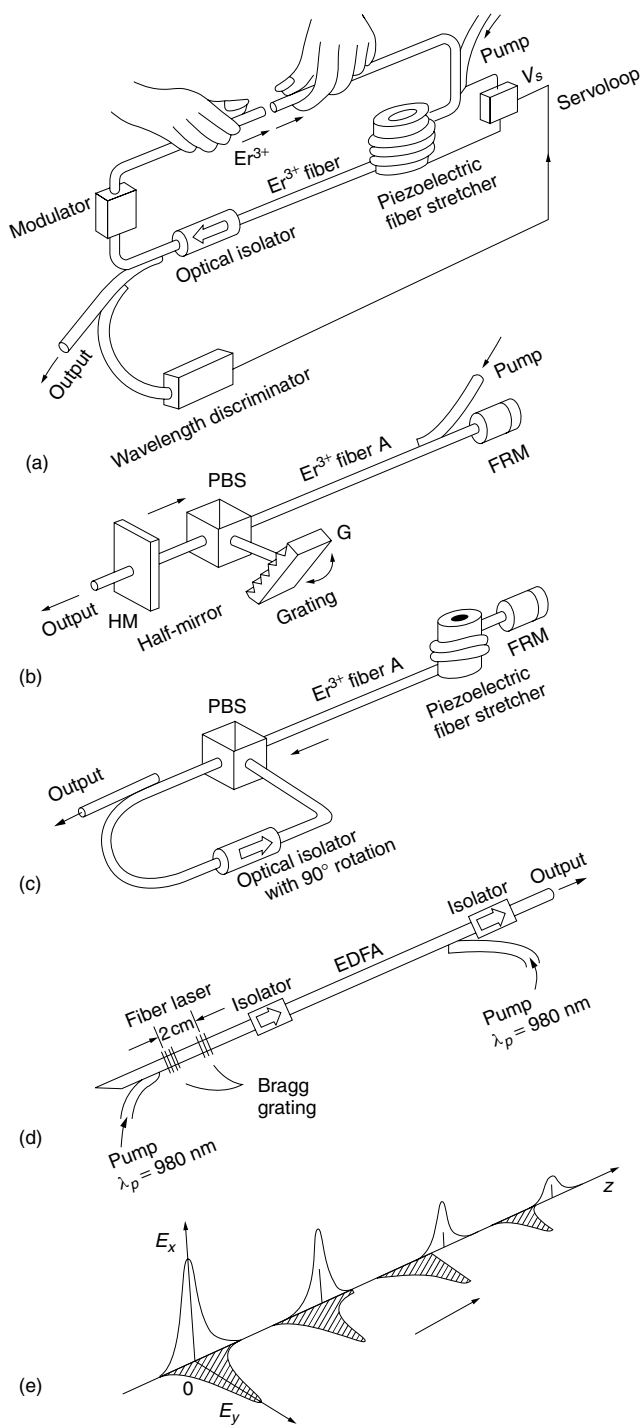
Figure 14.67 Erbium-doped fiber laser. (a) Ring type. (b) Fabry–Pérot type. (c) Sigma type. (d) Erbium-doped fiber grating laser (EDFGL). (e) Pulse spread due to the birefringence of the Er^{3+}-doped fiber.

optical isolator is vertically polarized. The vertically polarized wave is deflected by the PBS toward A. Upon reflection from the FRM, the vertically polarized wave changes back to horizontal polarization. The horizontally polarized wave is incident onto the PBS, and we are back to our starting point. The wave traveling to the right in A is always vertically polarized, and the wave traveling to the left is always horizontally polarized. This eliminates the problem of spatial hole burning.

Figure 14.67d is another type of fiber laser [42]. Bragg reflectors that have been written by photobleaching the glass are used at both ends of the fiber laser. The structure is quite similar to the solid-state DBR laser shown in Fig. 14.30. This is a fiber version of it. In the laser itself, the fiber length is only a few centimeters long, and since gain is proportional to length, a short length means less output power. The lack of output power is supplemented by an EDFA, which accompanies the laser. One advantage of a short laser section is the minimization of the output power fluctuation due to the relaxation oscillation. Another advantage is the assurance of single longitudinal mode oscillation by making the separation of the adjacent longitudinal modes given by Eq. (14.34) wider. Another advantage of this system is that the same pump power can be used for both the laser and the accompanying EDFA. The pumping efficiency is not decreased despite the short laser section because the residually transmitted pump power is used in the EDFA.

The configuration of alternating vertical and horizontal polarizations is not only useful for getting rid of spatial hole burning, but also for preventing pulsewidth spread during pulse mode operation. As indicated in Fig. 14.67e, the pulse is decomposed into horizontal and vertical components. If the two components have different group velocities due to birefringence in the fiber, the pulsewidth spreads as it propagates in the fiber [43]. This can be prevented by alternating the directions of polarization in such a way as mentioned above.

The fiber laser can function in either continuous wave operation or pulse mode operation. Pulse modulation is achieved by either installing an amplitude modulator [42] in the erbium-doped fiber or pumping with pulsed light.

The state of polarization of the output can be made linearly polarized if polarization-maintaining erbium doped fiber [44] is used.

Subpicosecond pulses can be generated if the fiber laser is combined with a nonlinear amplifying loop, which generates an optical soliton wave (see Section 15.6) [45].

14.14   LIGHT-EMITTING DIODE (LED)

Recall that there are two mechanisms of emission of photons from the p-n junction due to the recombination of the electrons with holes. One is stimulated emission, which is the basic mechanism of the already mentioned semiconductor laser diode. The other is spontaneous emission, which is the basic mechanism of the light-emitting diode (LED). The light-emitting diode is the topic of this section.

14.14.1   LED Characteristics

The LED has quite a similar structure to a laser diode except that the LED does not have the laser cavity that is necessary to enhance the stimulated emission. The LED

is structurally much simpler than the laser diode, so that compared to the laser diode, the LED has advantages such as:

- The fabrication cost is lower.
- The LED can operate at higher temperatures, while its operation is less influenced by temperature variations.
- The drive current is moderately low, and the drive circuit is simple.
- The output light power is moderately linear with respect to the drive current.
- Its lifetime is extremely long, of the order of 10^8 hours.

The disadvantages of the LED are:

- The LED has a broader wavelength spectrum (10–50 nm).
- The cutoff frequency for modulation is normally less than 100 MHz.
- The radiation beam is spatially wider ($30° \times 120°$) and harder to couple into an optical fiber.

LEDs with emission in the visible wavelength range are widely used as status indicators in electronic instruments and display panels, mainly because of their long life, low consumption of electric power, and low cost.

14.14.2 LED Structure

There are two LED types: one is the surface-emitting LED and the other is the edge-emitting LED.

The surface-emitting LED is sometimes called the Burrus-type LED. The structure is shown in Fig. 14.68. The structure is quite similar to the surface-emitting laser diode, except for the absence of the cavity reflectors. The advantage of the surface-emitting structure as shown in Fig. 14.68 is that the light generated in the active layer has only to traverse the 1-μm thickness of the active layer in order to exit via the 3-μm-thick cladding layer; the light does not have to travel the entire 20–30 μm length of the active region. Light whose quantum $h\nu$ is larger than the bandgap of the transmission medium is subjected to absorption. The amount of absorption increases with $h\nu$. Since the LED has such a wide spectrum, the longer the light stays in the active region, the more severely absorbed the higher frequency components become.

The refractive index of the GaAs material is large ($n = 3.5$), and the critical angle is small, so that only the light inside a cone with an apex angle of $\pm 16.6°$ can exit the LED from the active layer. The surface-emitting structure also creates a difficulty in coupling the light to an optical fiber. Moreover, the dimension of the emitting area is large, and a short focal length lens is needed to project the image of the active area onto the end of the core of the optical fiber. A good short-focal-length lens is hard to fabricate.

Figure 14.69 shows the structure of the edge-emitting LED. It is quite similar to the electrode stripe laser except that the active layer is not excited along the entire length. For better external efficiency (input electric power to output light power), only the portion of the active region that is near the exit is excited. This structure also reduces the cavity resonance effect and heat sink problems. The cavity resonance effect in the
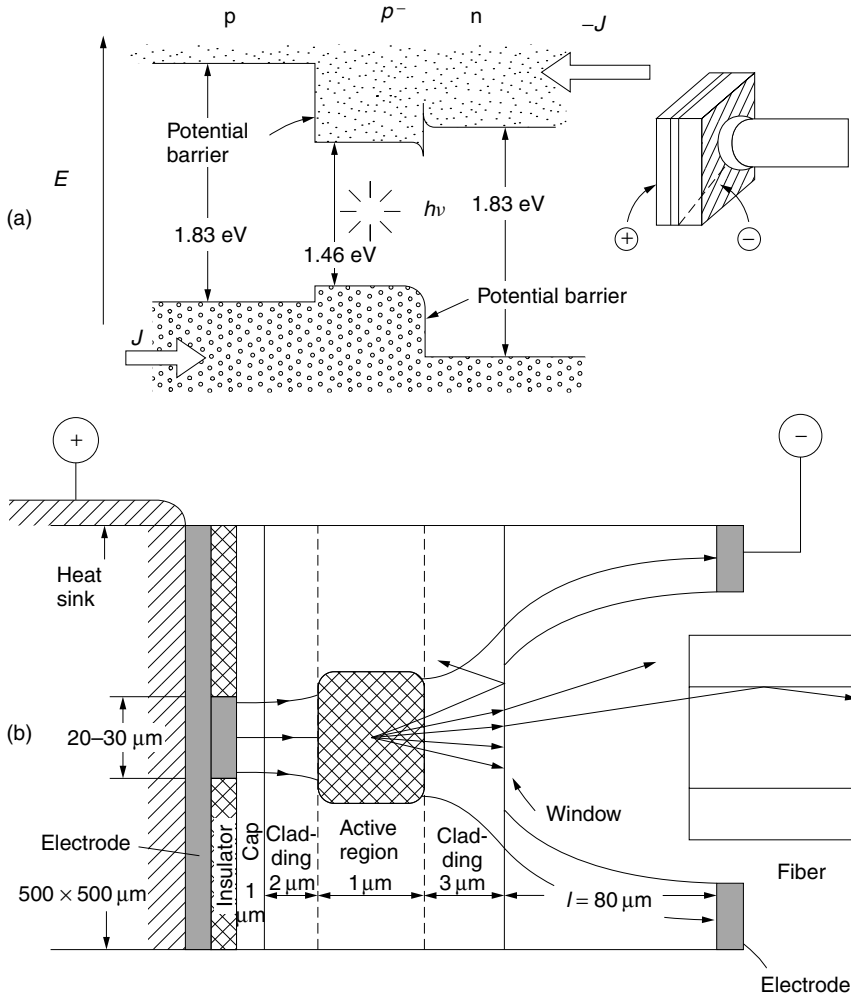
Figure 14.68   Structure of surface-emitting LED. (a) Energy bandgap. (b) Structure: cladding layer, $Al_{0.3}Ga_{0.7}As$; active layer, $Al_{0.03}Ga_{0.97}As$.

surface-emitting LED arises from the cladding interfaces that act as low-reflectivity reflectors. While the "edge" of the edge-emitting LED does act as a reflective boundary, the reflected light is likely to be absorbed before reaching the other end, and a resonant cavity is not established.

14.15   FIBER RAMAN LASERS

A method of amplifying the light by means of the enhancement of the Stokes radiation has already been described in Section 12.8.1. Fiber Raman lasers [46–48] are a natural extension of this technique. When the pump light with frequency ω_L is injected into the Raman fiber, the light acquires an increase in amplitude as well as a shift in frequency to $\omega_L - \omega_R$, where ω_R is the Raman shift frequency.
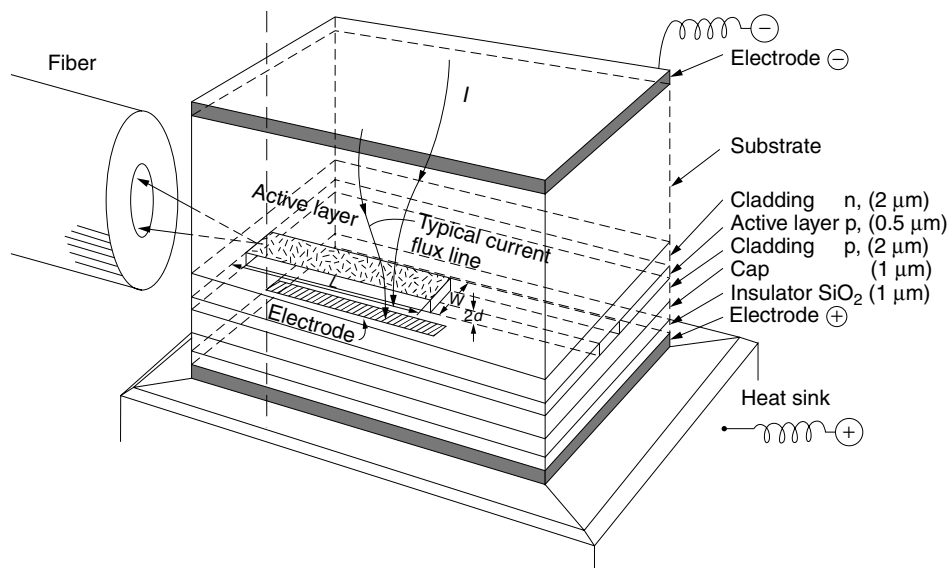
Figure 14.69 Structure of an edge-emitting LED. Cladding layers, $Al_{0.3}Ga_{0.7}As$, $E_g = 1.83$ eV. Active layer, $Al_{0.03}Ga_{0.97}As$, $E_g = 1.46$ eV.

Figure 14.70a shows a diagram of sets of fiber Bragg gratings (fiber Bragg gratings are described in Section 11.5). The center frequencies match the Raman shifted frequencies. Gratings $B_0, B_1, B_2, \ldots, B_n$ are placed on the right side of the GeO_2 fiber and $B'_1, B'_2, B'_3, \ldots, B'_n$ on the left side, in order to form a GeO_2 fiber cascaded Raman laser resonator. All of the gratings are highly reflective at their respective frequencies except the outermost grating B_n which is only partially reflective. For better input coupling, grating B'_0 is absent.

Pump light at ω_L is incident to the resonator. Due to the Raman effect, a portion of the incident light shifts its frequency to $\omega_L - \omega_R$. A portion of the $\omega_L - \omega_R$ component shifts further to $\omega_L - 2\omega_R$, which in turn shifts to $\omega_L - 3\omega_R$, and so forth. All of the components except the ω_L component pass through B_0. The $\omega_L - \omega_R$ component is reflected back and forth inside the cavity by B_1 and B'_1, which are highly reflective at $\omega_L - \omega_R$ but pass other frequencies. Similarly, the $\omega_L - 2\omega_R$ component is reflected back and forth by B_2 and B'_2, which are highly reflective at $\omega_L - 2\omega_R$ but pass other frequencies. Thus, lower order frequency components go back and forth inside the cavity until their frequency is shifted to the next higher order. This process repeats until the light reaches the outermost cavity gratings. At the outermost grating B_n which is partially reflective, a portion of the $\omega_L - n\omega_R$ component escapes. The escaped light is the laser output.

Figure 14.70b shows a schematic of the Raman fiber laser [46]. It is made of germanosilicate fiber (GeO_2-doped fiber) about 1 km long. The fiber Bragg gratings' center frequencies match the Raman-shifted frequencies up to the fifth order. The frequency of the pump light is ω_L and that of the output is $\omega_L - 5\omega_R$. The Raman shift frequency ω_R is 13.2 THz (450 cm^{-1}) in each order. If the pump frequency is set so that the output wavelength is $\lambda = 1.48$ μm, then the laser can be used as a pump light to an erbium-doped fiber amplifier.
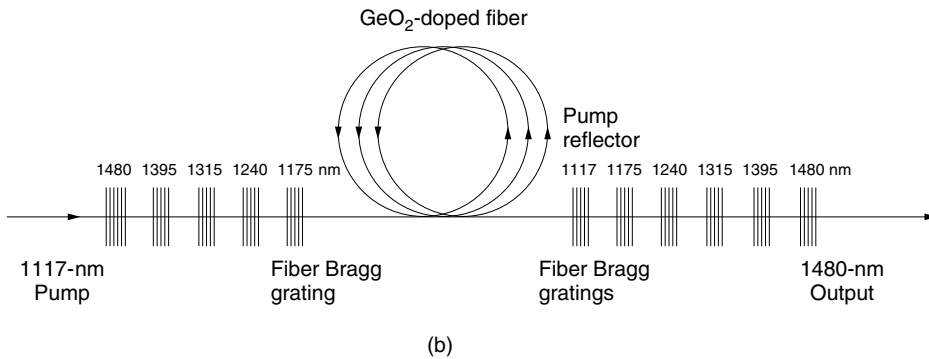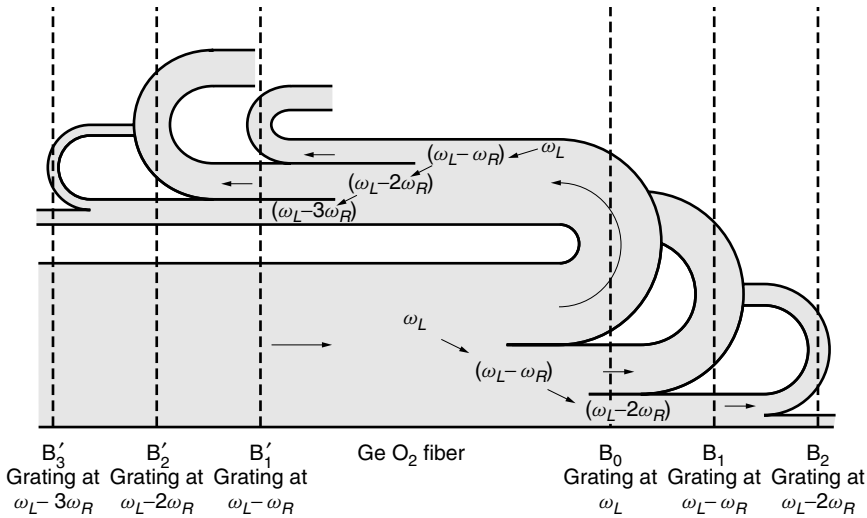
(a)

(b)

Figure 14.70 Fifth order 1480 nm cascaded Raman fiber laser. (a) Principle of operation. (b) Schematics. (After J. L. Archambault and S. G. Grubb [46].)

The main feature of the fiber Raman laser is simplicity with elegance. The conversion efficiency, which is the ratio of pump power to output power, is as high as 46%. The saturation power is high (0.4 W = 26 dBm). The biggest advantage of all is that even though the amount of frequency shift is set by the material of the fiber, there is no restriction on the pump wavelength. The frequency of the pump can be set according to the desired frequency of the output light.

14.16   SELECTION OF LIGHT SOURCES

The four major types of light sources that are most often used for fiber-optic communication systems have been presented. They are the semiconductor laser diode (LD), the solid-state laser, fiber lasers, and the light-emitting diode (LED). Although all four light sources possess such advantages as being rugged, compact, reliable, long-lived, and low electric consumption, there are some differences in

the characteristics, and proper selection of the source is important. The spectra are compared in Fig. 14.71.

The laser diode is the most widely used because of its high light power output, the reasonable purity of its spectrum, and the ease of direct modulation. The laser diode can be modulated up to tens of gigahertz. The disadvantages are turn-on delay time, temperature-induced instability, and sensitivity to the reflected light from the load. The lifetime of the laser diode, however, is not as long as that of a light-emitting diode.

The Nd:YAG solid-state laser of the MISER configuration (see Section 14.9.4) has the special feature of an extremely narrow spectral width of 10^{-7} nm (or 10–100 kHz) and is suitable for the main and local oscillator lasers of an optical heterodyne system. The output power is more or less the same as the laser diode. The Nd:YAG solid-state laser is optically pumped by an array of the semiconductor laser diodes and is structurally the most complicated. The disadvantages are the difficulty of high-speed direct modulation and the higher cost.

Fiber lasers are relatively simple structurally and compact. They can easily be connected to optical fiber systems. They are useful not only for fiber-optic communication systems but also for other applications as well, such as sources for fiber-optic gyros.
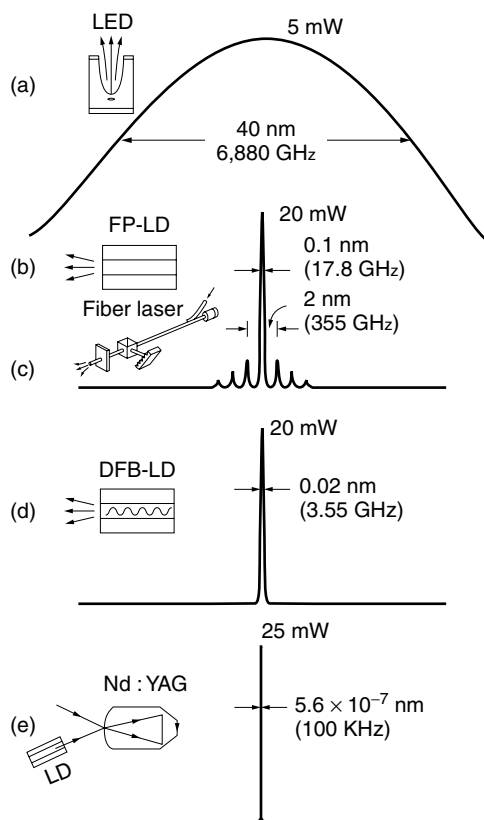

Figure 14.71 Comparison of the spectra of sources. (a) Light-emitting diode (LED). (b) Fabry–perot laser diode (FP-LD). (c) Erbium-doped fiber laser. (d) Distributed feedback laser diode (DFB-LD). (e) Laser diode driven Nd:YAG solid-state laser.

The LED emits radiation in a broad spectrum of light as compared to laser sources. Because of this broadness of the spectrum, the chromatic dispersion in the glass fiber is large and the distance of transmission is much more limited than that of the system with a laser diode. Another shortcoming of the LED is the limit on the modulation frequency, which is limited to less than a few hundred megahertz. The limitation on the modulation frequency is inherent. The cutoff modulation frequency of the LED is $f_c = 1/2\pi\tau_n$, whereas that of the LD is $f_c \propto 1/2\pi\sqrt{\tau_n\tau_s}$, where τ_n is the lifetime of the injected electrons and τ_s is the lifetime of the photons before leaving the laser cavity (see Section 14.3). τ_n is of the order of nanoseconds, while τ_s is of the order of picoseconds. τ_n can be reduced by increasing the doping at the cost of the output light power. Further drawbacks of the LED are the difficulty of coupling the output light into a fiber, because of the spread of the radiation pattern of the LED, and the smaller output light power.

The LED, however, is structurally simple and rugged and has the longest lifetime of 10^8 hours (an estimated one hundred centuries!). It is also less temperature dependent and has simpler drive circuits than a laser diode.

PROBLEMS

14.1 An $Al_xGa_{1-x}As$ laser diode is operated at $J = 1.7J_{th}$. Find the relaxation time $1/\gamma$ of the relaxation oscillation and the upper limit of the modulation frequency f_r. The physical parameters are as follows:

Index of refraction	$n = 3.5$
Length of the cavity	$L = 2 \times 10^{-2}$ cm
Power attenuation constant	$\alpha = 25$ cm^{-1}

Cleaved surfaces were used as cavity end mirrors. The lifetime of the spontaneous emission measured by the turn-on delay time was $\tau_n = 2 \times 10^{-9}$ s.

14.2 Find an expression for the decay constant γ of the relaxation oscillation that corresponds to Eq. (14.81) without the assumption that $N_{th} >> N_\alpha$.

14.3 Find the following quantities for a $Ga_{0.47}In_{0.53}As$ semiconductor laser with the dimensions and physical constants given in Fig. P14.3.
   (a) The turn-on-delay time at $J/J_{th} = 1.2$.
   (b) The length of the laser cavity.
   (c) The threshold electron density (use Fig. 14.6).
   (d) The threshold current.
   (e) The relationship between the light output power and the injection current.

14.4 In connection with Fig. 14.55b, decompose the two complex fields $\tilde{E}_1 = E_1 e^{j\phi_1}$ and $\tilde{E}_3 = E_3 e^{j\phi_3}$, into symmetric $\tilde{E}_s$ and antisymmetric $\tilde{E}_a$ components using a phasor diagram. The tilde symbol represents a phasor vector on the complex plane, and not a spatial vector.

14.5 Determine the values of I_{th0}, η_{th0}, T_0, and T_0' from Fig. 14.26.
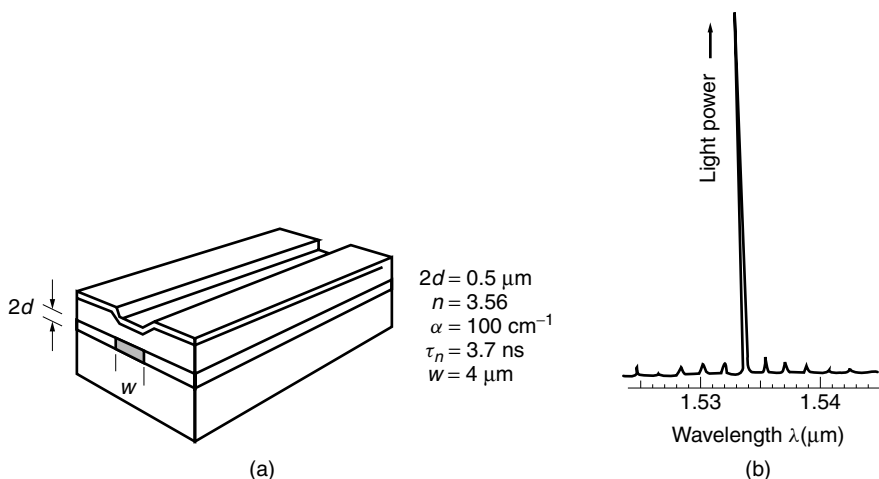
Figure P14.3   Semiconductor laser. (a) Dimensions. (b) Power spectrum.

14.6   The gain of a semiconductor laser diode for the case of $T = 0$ was graphically obtained in Fig. 14.4. The Fermi distribution function used in Fig. 14.4 was a curve with an abrupt ramp. Try the same, but this time, with a Fermi distribution function with a linear ramp representing the case of $T \neq 0$ so as to compare spectral distributions of $g(h\nu)$ for the case of $T \neq 0$ with that for the case of $T = 0$.

REFERENCES

1. A. E. Siegman, *Lasers*, University Science Books, Mill Valley, CA, 1986.

2. T. F. Carruthers and I. N. Duling III, "10 GHz, single-polarization, actively modelocked picosecond erbium-fiber laser," *Optical Fiber Communication Conference Record*, TuB6, San Jose, CA, Feb. 1996.

3. R. A. Chodzko, J. M. Bernard, and H. Mirels, "Coherent combination of multiline lasers," *Proc. SPIE* **1224**, 239–253 (1990).

4. G. P. Agrawal (ed.), *Semiconductor Lasers—Past, Present and Future*, American Institute of Physics, Woodbury, NY, 1995.

5. B. Sapoval and C. Hermann, *Physics of Semiconductors*, Springer-Verlag, Berlin, 1995.

6. C. Kittel, *Introduction to Solid State Physics*, 7th ed., Wiley, New York, 1996.

7. M. Asada and Y. Suematsu, "Density-matrix theory of semiconductor lasers with relaxation broadening model-gain and gain-suppression in semiconductor lasers," *IEEE J. Quantum Electron.* **QE21**(5), 434–442 (1985).

8. H. Yonezu, *Elements of Fiber Optical Communication Systems Emitter and Detectors*, 6th ed., Kogakutosho, Tokyo, 2000.

9. R. Tucker, C. Lin, and C. A. Burrus, "High-frequency small-signal modulation characteristics of short-cavity InGaAsP lasers," *Electron. Lett.* **20**(10), 393–394 (1984).

10. H. C. Casey, Jr. and M. B. Panish, *Heterostructure Lasers*, Vols. I and II, Academic Press, New York, 1978.

11. D. Botez, "Laser diodes are power-packed," *IEEE Spectrum*, 43–53 (June 1985).

12. T. K. Woodward, B. Tell, W. H. Knox, and J. B. Stark, "Suppressed photocurrent multiple-quantum-well optical modulator by proton implantation," *Appl. Phys. Lett.* **60**(6), 742–744 (1992).

13. E. Oomura, H. Higuchi, Y. Sakakibara, R. Hirano, H. Namizaki, W. Susaki, K. Ikeda, and K. Fujikawa, "InGaAsP/InP buried crescent laser diode emitting at 1.3 μm wavelength," *IEEE J. Quantum Electron.* **QE20**(8), 866–874 (1984).

14. H. Kawanishi, T. Morimoto, M. Yamaguchi, S. Kaneiwa, N. Miyauchi, T. Yoshida, H. Hayashi, S. Yano, and T. Hijikata, "High-power CW operation in V-channeled substrate inner-stripe lasers with "Torch"-shaped waveguide," *Jpn. J. Appl. Phys. 2 Lett.* **27**(7), L1310–L1312 (1988).

15. Y. Suematsu, *Semiconductor Laser and Optic ICs* (in Japanese), Ohm-Sha, Tokyo, 1984.

16. N. Chinone, T. Kuroda, T. Ohtoshi, T. Takahashi, and T. Kajimura, "Mode-hopping noise in index-guided semiconductor lasers, and its reduction by saturable absorbers," *IEEE J. Quantum Electron.* **QE21**(8), 1264–1270 (1985).

17. P. W. Smith, Y. Silberberg, and D. A. B. Miller, "Mode locking of semiconductor diode lasers using saturable excitonic nonlinearities," *J. Opt. Soc. Am. B.* **2**(7), 1228–1236 (1985).

18. M. Kitamura, M. Yamaguchi, S. Murata, I. Mito, and K. Kobayashi, "High-performance single-longitudinal-mode operation of InGaAsP/InP DFB-DC-PBH LDs," *J. Lightwave Technol.*, **2**(4), 363–369 (1984).

19. Y. Huang, H. Yamada, T. Okuda, T. Torikai, and T. Uji, "External optical feedback resistant characteristics in partially-corrugated waveguide laser diodes," *Optical Fiber Communication Conference Record*, TuH1, San Jose, CA, Feb. 1996.

20. T. Hamano, K. Iga, and T. Baba, "Spontaneous emission behavior and its injection level dependence in three-dimensional microcavity surface emitting lasers," *Electronics and Communications in Japan* (Translation into English by Scripta Technica), Part 2, Vol. 79, pp. 46–54, Wiley, New York, 1996.

21. R. T. Chen, L. Lin, C. Choi, Y. J. Liu, B. Bihari, L. Wu, S. Tang, R. Wickman, B. Picor, M. K. Hibbs-Brenner, J. Bristow, and Y. S. Liu, "Fully embedded board-level guided-wave optoelectronic interconnects," *Proc. IEEE* **88**(6), 780–793 (2000).

22. T. Kjellberg, S. Nilsson, T. Klinga, B. Broberg, and R. Schatz, "Investigation on the spectral characteristics of DFB lasers with different grating configurations made by electron-beam lithography," *J. Lightwave Technol.* **11**(9), 1405–1415 (1993).

23. H. Kogelnik and C. V. Shank, "Coupled-wave theory of distributed feedback lasers," *J. Appl. Phys.* **43**(5), 2327–2335 (1972).

24. M. Yamaguchi, T. Numai, Y. Koizumi, I. Mito, and K. Kobayashi, "Stable single-longitudinal-mode operation in λ/4 shifted DFB-DC-PBH laser diodes," *Optical Fiber Communication Conference Record*, TUC4, Reno, NV, Jan. 1987.

25. K. Kobayashi and I. Mito, "Progress in narrow-linewidth tunable laser sources," *Optical Fiber Communication Conference Record*, WC-1, Reno, NV, Jan. 1987.

26. T. J. Kane and R. L. Byer, "Monolithic, unidirectional single-mode Nd:YAG ring laser," *Opt. Lett.* **10**, 65–67 (1985).

27. K. Kobayashi and I. Mito, "Single frequency and tunable laser diodes," *J. Lightwave Technol.* **6**(11), 1623–1633 (1988).

28. K. Kobayashi, "Semiconductor lasers for optical fiber networks," *Conference on Lasers and Electrooptics (CLEO)*, Baltimore, pp. 10–11, May 1995.

29. A. Yariv and P. Yeh, *Optical Waves in Crystals: Propagation and Control of Laser Radiation*, Wiley, New York, 1984.

30. Y. Tohmori, Y. Yoshikuni, H. Ishii, F. Kano, T. Tamamura, Y. Kondo, and M. Yamamoto, "Broad-range wavelength-tunable superstructure grating (SSG) DBR lasers," *IEEE J. Quantum Electron.* **29**(6), 1817–1823 (1993).

31. G. Sarlet, G. Morthier, and R. Baets, "Control of widely tunable SSG-DBR lasers for dense wavelength division multiplexing," *J. Lightwave Tech.* **18**(8), 1128–1138 (2000).

32. L. Fan, M. C. Wu, H. C. Lee, and P. Grodzinski, "4 × 4 reconfigurable optical interconnection network using beam-steering vertical cavity surface emitting lasers," *Optical Fiber Communication Conference Record*, TuC2, San Jose, CA, Feb. 1996.

33. A. Husain and J. N. Lee (Eds.), "Special Issue on Interconnections for information Processing," *J. Lightwave Technol.* **13**(6), 985–1183 (1995).

34. D. Botez and D. R. Scifres (Eds.), *Diode Laser Arrays*, Cambridge University Press, Cambridge, 1995.

35. P. S. Zory Jr. (Ed.), *Quantum Well Lasers*, Academic Press, New York, 1993.

36. M. Asada, A. Kameyama, and Y. Suematsu, "Gain and intervalence band absorption in quantum-well lasers," *IEEE J. Quantum Electron.* **QE20**(7), 745–753 (1984).

37. M. Asada, Y. Miyamoto, and Y. Suematsu, "Gain and the threshold of three dimensional quantum-box lasers," *IEEE J. Quantum Electron.* **QE-22**(9), 1915–1921 (1986).

38. H. Hirayama, J. Yoshida, Y. Miyake, and M. Asada, "Carrier capture time and its effect on the efficiency of quantum-well lasers," *IEEE J. Quantum Electron*. **30**(1), 54–62 (1994).

39. E. Yoshida, Y. Kimura, and M. Nakazawa, "20 GHz, 1.8 ps pulse generation from a regeneratively modelocked erbium-doped fibre laser and its femtosecond pulse compression," *Electron. Lett.* **31**(5), 376–378 (1995).

40. T. F. Carruthers and I. N. Duling III, "10 GHz single-polarization, actively mode-locked picosecond erbium-fiber laser," *Optical Fiber Communication Conference Record*, TuB6, San Jose, CA, Feb. 1996.

41. I. N. Duling III and R. D. Esman, "Single-polarization fiber amplifier," *Electron. Lett.* **28**(12), 1126–1128 (1992).

42. G. A. Ball and W. H. Glenn, "Design of a single-mode linear cavity erbium fiber laser utilizing Bragg reflectors," *J. Lightwave Technol.* **10**(10), 1338–1343 (1992).

43. T. Morioka, H. Takara, K. Mori, and M. Saruwatari, "Ultrafast reflective optical Kerr demultiplexer using polarizatioin rotation mirror," *Electron. Lett.* **28**(6), 521–522 (1992).

44. K. Tajima, "$Er^{3\pm}$ doped single-polarization optical fibers," *Electron. Lett.* **26**(18), 1498–1499 (1990).

45. I. N. Duling III, "Subpicosecond all-fiber erbium laser," *Electron. Lett.* **27**(6), 544–545 (1991).

46. J.-L. Archambault and S. G. Grubb, "Fiber gratings in lasers and amplifiers," *J. Lightwave Technol.* **15**(8), 1378–1390 (1997).

47. E. M. Dianov, M. V. Grekov, I. A. Bufetov, S. A. Vasiliev, O. I. Medvedkov, V. G. Plotnichenko, V. V. Koltashev, A. V. Belov, M. M. Bubnov, S. L. Semjonov, and A. M. Prokhorov, "CW high power 1.24 μm and 1.48 μm Raman lasers based on low loss phosphosilicate fiber," *Electron. Lett.* **33**(18), 1542–1544 (1997).

48. M. Prabhu, N. S. Kim, and K. Ueda, "Simultaneous double-color continuous wave Raman fiber laser at 1239 nm and 1484 nm using phosphosilicate fiber," *Optical Review* **7**(4) 277–280 (2000).